UCLouvain

epl

École polytechnique de Louvain

Fabrication and electrical transport properties of twisted bilayer graphene devices

Author: **Alexis Warnier**
Supervisor: **Benoît Hackens**
Readers: **Jean-Christophe Charlier, Jean-Pierre Raskin**
Academic year 2018–2019
Master [120] in Physical Engineering

Abstract

Twisted bilayer graphene devices have been in the spotlight since 2018 and the discovery of superconducting states at the magic angle. It is probably the simplest member of the broader family of 2D Van der Waals heterostructures. The many degrees of freedom in these structures, ranging from the chemical nature of the layers to the relative orientations of their crystalline lattices, yield the access to a wide variety of properties, many of which are yet to be discovered. In twisted bilayer graphene, it is the ability to continuously tune the band structure and especially the band velocity that has sparked the interest of researchers. In particular, at the so-called magic angle, the band velocity of twisted bilayer graphene almost vanishes giving rise to strongly correlated electronic systems, home to many exotic properties, such as the superconducting state.

In this master thesis, a fabrication process for the creation of twisted bilayer graphene devices is developed and presented. Twisted bilayer graphene encapsulated in hexagonal boron nitride samples were created from scratch and characterized optically and with Raman spectroscopy. The process is based on dry transfer of exfoliated graphene and h-BN flakes. The presented method is especially easy and efficient for the creation of a wide variety of Van der Waals heterostructures. The characterization of the samples indicated that the method was successful at stacking the different layers in the desired configurations. For example, the Raman signatures of the twist angle between the graphene layers has been observed. However, this works also presents some minor issues that still need to be addressed before the process can serve for the creation of usable samples.

Keywords: twisted bilayer graphene, h-BN, superconductivity, fabrication process, Van der Waals heterostructures, 2D crystals, Raman

List of Symbols

Abbreviations

2DEG	Two-dimensional electron gas
2D	Two-dimensional
3D	Three-dimensional
AFM	Atomic force microscopy
Ar	Argon
Au	Gold
BLG	Bilayer graphene
CHF_3	Trifluoromethane (fluoroform)
Cr	Chromium
DOS	Density of states
F.S.	Fermi surface
FWHM	Full width at half maximum
h-BN	Hexagonal boron nitride
HOPG	Highly oriented pyrolytic graphite
HSQ	Hydrogen silsesquioxane
ICP	Inductively coupled plasma
LDOS	Local density of states
MIBK	Methyl isobutyl ketone
O_2	Oxygen gas
PC	Polycarbonate
PDMS	Polydimethylsiloxane
PID	Proportional–integral–derivative
PMMA	Poly(methyl methacrylate)
PPC	Polypropylene carbonate
QHE	Quantum Hall effect
RF	Radio frequency
RIE	Reactive ion etching
RPM	Revolutions per minute
SEM	Scanning electron microscopy
SF_6	Sulfur hexafluoride

SiO_2	Silicon dioxide
Si	Silicon
SLG	Single layer graphene
tBLG	Twisted bilayer graphene
VHS	Van Hove singularity

Physical quantities

α	Fine structure constant
β	Angle
ϵ	Effective dielectric constant
ϵ_0	Vacuum permittivity
$\hbar$	Reduced Plank Constant
κ	Dimensionless parameter
λ	Wavelength
λ_1	Scattered wavelength
λ_2	Incoming wavelength
$\mathbf{a_1^{(1)}}$	First unit vector of the bottom graphene layer in tBLG
$\mathbf{a_1^{(2)}}$	First unit vector of the top graphene layer in tBLG
$\mathbf{a_2^{(1)}}$	Second unit vector of the bottom graphene layer in tBLG
$\mathbf{a_2^{(2)}}$	Second unit vector of the top graphene layer in tBLG
$\mathbf{L_1}$	First unit vector of the Moiré pattern in tBLG
$\mathbf{L_2}$	Second unit vector of the Moiré pattern in tBLG
∇	Gradient
ν	Filling factor
ϕ	Magnetic flux
ϕ_0	Magnetic flux quantum ($h/(2e)$)
π	Mathematical constant (3.14...)
ρ_{xx}	Longitudinal resistivity
σ	Electrical conductivity
σ_{xy}	Transverse conductivity
θ	Twist angle
$\theta_{Magic}^{(n)}$	nth magic angle of tBLG
A	Moiré supercell area
a	Lattice parameter of single layer graphene
B	Magnetic field
c	Speed of light
D	Largest dimension
d	Carbon-carbon distance in graphene
E	Energy
e	Elementary charge unit

G_0	Quantum unit of conductance ($= 2e^2/h$)
G_K	Separation between the K and Γ in reciprocal space
h	Plank Constant
k	Wave vector
k_θ	Separation of the Dirac cones in reciprocal space
k_x	x-component of the wave vector
k_y	y-component of the wave vector
L	Commensurate supercell lattice parameter
l_B	Magnetic characteristic length
L_M	Moiré lattice parameter
m^*	Effective mass
m_c	Cyclotron mass
n	Charge carrier density
$n_{s,2D}$	Superconductive charge carrier density
p	Pressure
R_{xx}	Longitudinal resistance
S	Commensurate supercell area
T	Absolute temperature
T_c	Superconductive critical temperature
T_F	Fermi temperature
$t_\perp$	Up (down) shift of the Dirac cones in AA stacked bilayer graphene
U	Coulomb potential energy
u^-	Displacement vector
V_0	Reference potential
v_0	Fermi velocity near the K an K' points in single layer graphene
v_F	Fermi velocity
V_g	Gate voltage
W	Bandwidth
w	Half of the band gap created for interacting Dirac cones
x, y and z	Real space Cartesian coordinates

Units

% vol.	Volume fraction (unit of concentration)
$^\circ$	Degree (unit of angle)
$^\circ$C	Degree Celsius (unit of temperature)
µC	Microcoulomb (10^{-6} C)
µm	Micrometre (10^{-6} m)
cm^{-1}	Number of charge carriers per cm (charge carrier density)
cm^{-1}	Number of wavelengths per cm (spectroscopic unit of energy)
cm	Centimetre (10^{-2} m)

C	Coulomb (unit of electric charge)
eV	Electronvolt (unit of energy)
GPa	Gigapascal (10^9 Pa)
h	Hour (unit of time)
kΩ	Kiloohm (10^3 Ω)
kV	Kilovolt (10^3 V)
K	Kelvin (unit of temperature)
mbar	Millibar (10^2 Pa)
meV	Millielectronvolt (10^{-3} eV)
min	Minute (unit of time)
mm	Millimetre (10^{-3} m)
mTorr	Millitorr ($1.33 \cdot 10^2$ Pa)
m	Metre (unit of length)
nm	Nanometre (10^{-9} m)
Pa	Pascal (unit of pressure)
pm	Picometre (10^{-12} m)
sccm	Standard cubic centimetre per minute
s	Second (unit of time)
TPa	Terapascal (10^{12} Pa)
T	Tesla (unit of magnetic field intensity)
V	Volt (unit of electric potential)
Wb	Weber (unit of magnetic flux)
W	Watt (unit of power)

Contents

1 Introduction **7**

2 State of the art **8**
2.1 Graphene 8
2.1.1 Description 8
2.1.2 Properties 10
2.2 Hexagonal boron nitride 12
2.3 Twisted Bilayer graphene 12
2.3.1 Physical structure of tBLG 12
2.3.2 Electronic structure of tBLG 14
2.3.3 Reported and expected phenomena 20

3 Fabrication process **25**
3.1 Desired sample 25
3.2 Mechanical exfoliation 26
3.2.1 Graphene 28
3.2.2 h-BN 31
3.3 Raman spectroscopy 32
3.3.1 Working principle 32
3.3.2 Graphene 34
3.3.3 h-BN 38
3.4 Thermal annealing 38
3.5 Dry transfer 39
3.5.1 Tools 40
3.5.2 Transfer 43
3.5.3 Twist angle 47
3.5.4 Stack flips 49
3.6 Lithography 50
3.6.1 Working principle 50
3.6.2 Preparation 51
3.6.3 Exposure and development 52

3.6.4 Etching . . . 52
3.7 Contacting . . . 56

4 Fabrication results **57**
4.1 Graphene flakes . . . 57
4.2 h-BN flakes . . . 59
4.3 Transfer . . . 60
4.4 Lithography and etching . . . 62
4.5 Characterization . . . 64
4.6 Stack flips . . . 66

5 Conclusion and perspectives **67**

6 Acknowledgements **69**

A Commensuration condition **79**

B Process sheet **81**

C Supplementary illustrations **84**

Chapter 1

Introduction

Since graphene was first isolated by Novoselov et al. in 2004 [1] it has surged to become one of the most studied material in experimental physics. Soon, researchers realized that one of the most common defects in few-layer graphene was orientational disorder between the different layers. At first, little attention was given to this type of structure. Only a few theoretical papers predicted the emergence of interesting electronic structures in small angle twisted bilayer graphene [2].
Techniques evolved and the ability to experimentally control the twist angle between different graphene layers sparked interest for these structures. In 2017, the study of electronic properties in twisted structures of 2D materials was given the name of "twistronics" by Carr et al. [3]. From there, things accelerated and, in March 2018, Cao et al. [4, 5] announced the discovery of both an insulating and superconducting state in so-called magic angle twisted bilayer graphene. The transition between the insulating and superconducting state is possible simply by changing the gate voltage of the device. This major discovery was named "breakthrough of the year 2018" by the magazine Physics World. It made people dream of the possibility to make 100% carbon based superconducting transistors. A major improvement in an environmentally fragile world, with an ever-increasing importance of electronics.

For now, this remains a dream and only progress in this domain will tell if it can ever be realized. The purpose of this master thesis is to dive into this new field of research. This is done with both a theoretical understanding of these exotic phenomena and the development of fabrication techniques, eventually making them experimentally accessible. This work is composed of a large state of the art section, providing an overview and understanding of the (recent) developments in this promising field of twistronics. It is followed by a precise description and justification of the fabrication techniques used. Eventually, an analysis of the results obtained is presented, emphasizing the strengths and weaknesses of all the techniques developed.

Chapter 2

State of the art

2.1 Graphene

2.1.1 Description

In order to fully understand the behavior of twisted bilayer graphene, it is important first to understand its building block: graphene. Graphene is a two dimensional, honeycomb-like, crystal of carbon atoms. It is essentially a single-layer thick graphite. It was first (intentionally) isolated and characterized by Novoselov et al. in 2004 [1], earning them the Nobel prize. Figure 2.1 shows the physical structure of graphene.

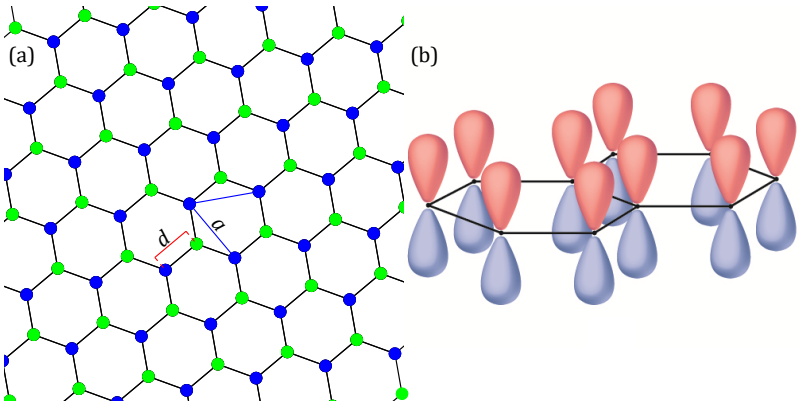


Figure 2.1: (a) Physical structure of graphene. The blue and green dots represent the carbon atoms of the two Bravais triangular sublattices. The blue lines represent the unit vectors, of length $a = 246$ pm, of the blue lattice. $d = 142$ pm is the inter-atomic distance. (b) Representation of the perpendicular p-orbitals[1].

[1]Image (b) from wikimedia: CNX_Chem_18_04_unhyporbC.png

The honeycomb structure can be represented by a combination of two Bravais triangular lattices, represented on the figure by the green and blue dots. The lattice parameter of these sublattices is $a = 246$ pm, whereas the inter-atomic distance is $d = 142$ pm. Chemically, each carbon atom is bonded to three neighbouring carbon atoms and hence presents a sp^2 hybridization. This leaves one p-orbital, containing one electron, perpendicular to the plane for each atom. These electrons form, through chemical resonance, a 2-dimensional delocalized electron gas (2DEG) that is key to most of graphene's peculiar properties.

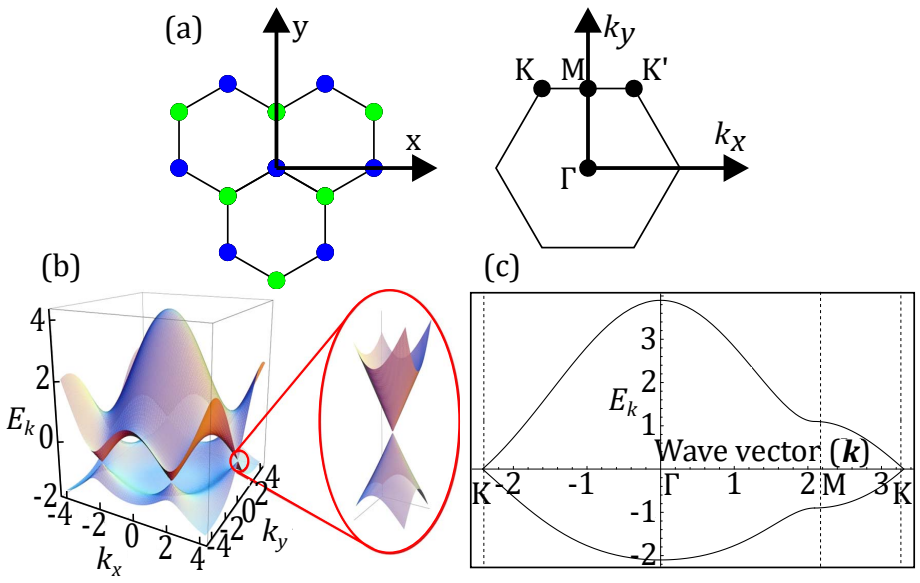


Figure 2.2: Band structure of single layer graphene. (a) Left: Physical structure of single layer graphene. Right: first Brillouin zone of single layer graphene. (b) Band structure of graphene with a zoom on the structure around a K-point, showing the Dirac cone [6]. (c) Band structure along the given path [7]. The energy is expressed in units of the tight-binding parameter $t \approx 2.7$ eV. This parameter is called the nearest neighbour hopping energy. The wave-vector is in units of $1/d$, $d = 0.142$ nm being the carbon-carbon distance of graphene.

Figure 2.2.a shows the geometry of the first Brillouin zone of graphene. Figure 2.2.b and 2.2.c show the very peculiar band structure of graphene. At the K and K' points, the band structure shows a linear dispersion instead of a usual parabolic dispersion. This linear dispersion relationship leads to the formation of a cone shaped band, called the Dirac cone. The tips of the cones coincide with the Fermi level. This leads to the peculiar situation of graphene having zero density of states at the Fermi level and non-zero right below or above. For this reason, graphene is considered as a zero band gap semiconductor or a semimetal with zero overlap

between conduction and valence band.

2.1.2 Properties

Graphene has kept surprising scientists with its unique properties of all kinds, from mechanical to electrical. Here is a short overview of these properties.

Mechanical properties

To begin with, graphene is one of the stiffest materials known. Its in-plane Young's modulus has been measured at 1 TPa [8]. Comparatively, steel has a Young's modulus around 200 GPa. Graphene also has the peculiar property of having a negative thermal expansion coefficient, i.e. it shrinks when heated up [9].

Optical properties

Optically, graphene is also an extremely interesting material. It is a relatively transparent conductor, a relatively unique feature. However, this is what could be expected from an atomically thin film. In fact, graphene has a high optical absorbance (almost 2.3%) for a single atom layer. What is even more remarkable is that this absorbance is frequency independent over a large part of the spectrum and only given by universal constants as the expression $\pi\alpha$ [10][2].

Heat transport properties

Next to one of the highest Young's moduli known, Graphene also possesses one of the highest in-plane thermal conductivity coefficients ever observed. Experimental values yielded thermal conductivity coefficients between 2000 and 3000 W m^{-1} K^{-1} [11] at room temperature. Comparatively, copper only displays a thermal conductivity coefficient of $\sim$ 380 W m^{-1} K^{-1}. This high thermal conductivity coefficient in graphene is beneficial for potential electronic applications [12].

Electronic properties

Graphene's electronic band structure has already been discussed in figure 2.2. The peculiar shape of the Dirac cone can be experimentally observed through electrical conductivity measurements as a function of gate voltage as shown in figure 2.3. A positive (negative) gate voltage shifts the Fermi level up (down), filling the conduction (valence) band with electrons (holes). This is commonly known as n-doping (p-doping) through electric field and allows for a continuous tuning of

[2] α is the fine-structure constant and given by $\alpha = \frac{e^2}{4\pi\epsilon_0\hbar c} \approx \frac{1}{137}$

the doping level. Compared with chemical doping in conventional semiconductors, which requires one sample per doping level, this is a major advantage of graphene.

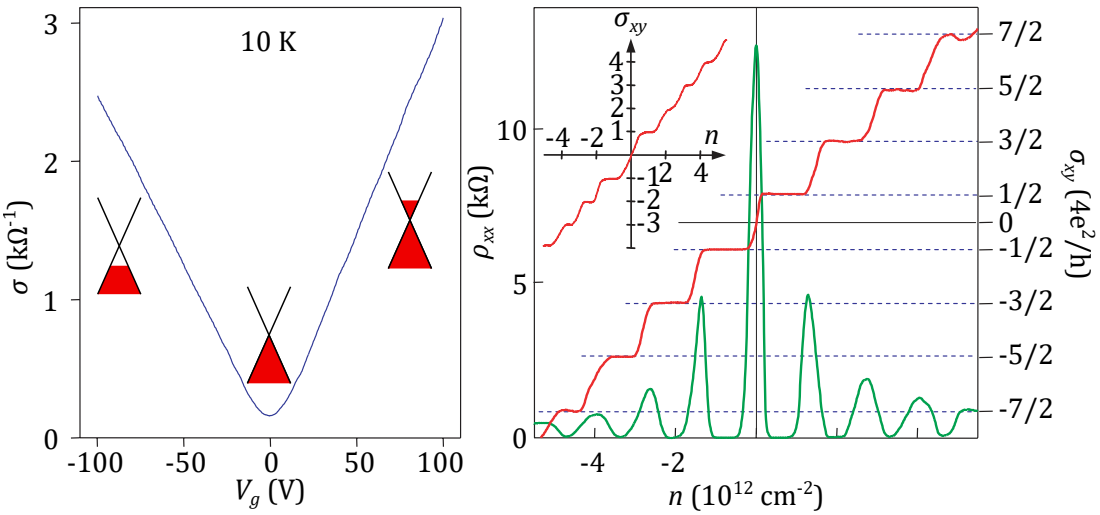


Figure 2.3: Left: Conductivity as a function of gate voltage. Right: Quantum Hall effect in graphene. Red is the Hall conductivity, green is the longitudinal resistivity. The inset shows the QHE in Bernal stacked bilayer graphene. The axis units are the same for the larger plot as for the inset. Adapted from [13].

The linear dispersion relationship gives a constant band velocity, regardless of the energy of:

$$v_F = \frac{1}{\hbar}|\nabla_{\mathbf{k}} E_{\mathbf{k}}| = v_0 \approx 10^6 \text{ m} \cdot \text{s}^{-1} \tag{2.1}$$

This means that the energy is independent of the velocity of an electron. A naive explanation could be an infinite effective mass, which is also coherent with the traditional definition of effective mass ($(m^*)^{-1} \propto \partial^2 E/\partial k^2$). However, this wouldn't fit with high observed electron mobility in graphene (up to ~ 180000 and $> 10^6$ cm^2 V^{-1} s^{-1} respectively at room and low temperature [14]). Instead, eq. 2.1 can be interpreted as the equation of massless relativistic electrons, similar to photons, with a special "speed of light" v_0. These electrons can be described by the Dirac equation and are hence called Dirac fermions. This interpretation has several consequences that can be confirmed experimentally. First, the fact that graphene's conductivity never falls below one quantum unit of conductance[3]. Second, the quantum Hall effect (QHE) [15] shows conductivity plateaus at half integer filling factors instead of integer ones with non-relativistic electrons. Third, the cyclotron

[3]Quantum unit of conductance $= G_0 = 2e^2/h$ with e the elementary charge unit and h Planck constant

mass is expressed as $m_c = E/v_0^2$ [13]. Figure 2.3 shows the mentioned half-integer QHE, each conductance plateau is located at half-integer multiples of $4e^2/h$. As a comparison, the inset shows the QHE of Bernal stacked bilayer graphene[4], where all plateaus are located at integer multiples of $4e^2/h$. The fact that the conductance exhibits steps of $2 \times G_0$ is because of the presence of two Dirac cones (at the K and K' points) in the first Brillouin zone. This degeneracy due to the presence of two Dirac cones is called valley degeneracy.

2.2 Hexagonal boron nitride

Hexagonal boron nitride (h-BN) is a polymorph of boron nitride, where the boron and nitrogen atoms are disposed in a honeycomb structure, just like graphene. The boron and nitrogen atoms each occupy the position of one of the triangular Bravais sub-lattices (cfr. the blue and green positions in figure 2.1). The lattice parameter of h-BN is $a \approx 250$ pm [16], 1.7% more than graphene's 246 pm. Its similar structure with graphene resulted in its nickname: "white graphene". In opposition to graphene, h-BN is an insulator, with a wide band gap of ~ 5.2 to 5.5 eV depending on the thickness of the film [17]. This, as well as its graphene-like structure, make it an ideal substrate for graphene-based devices.

2.3 Twisted Bilayer graphene

2.3.1 Physical structure of tBLG

tBLG is made of two graphene layers with a twist angle between their crystalline orientation. Figure 2.4 shows a schematic view of those two layers (red and green). Because of the twist angle, the bilayer no longer has the same periodicity as the original crystals. In fact, two things can happen, either the structure has no periodicity at all, either the periodicity is recreated at a larger scale (e.g in figure 2.4). The angles for which the periodicity reappears are called "commensurate" angles (see appendix A for the commensuration condition). In that case, all atoms from one layer have rational coordinates in the basis of the unit vectors of the other layer (if translations of the layers are neglected[5]). For commensurate angles, a new, larger unit cell (black in the figure) emerges and creates what is called a superlattice. This new and larger lattice will be key to all the exotic properties observed in tBLG. Mathematically, if the unit vectors of the two original crystals

[4]Bernal stacked bilayer graphene consists of two graphene sheets, with zero twist angle between them and in AB stacking configuration (cfr. fig 2.5.d)

[5]Even with a translation, the structure can still be considered commensurate, but atoms might have irrational coordinates

are given by the vectors $\mathbf{a_1^{(1)}}$, $\mathbf{a_2^{(1)}}$, $\mathbf{a_1^{(2)}}$ and $\mathbf{a_2^{(2)}}$, the new, supercell unit vectors may be represented as linear combinations of these, with integer coefficients if the angles is commensurate. These new unit vectors are called $\mathbf{L_1}$ and $\mathbf{L_2}$ and can be expressed as $\mathbf{L_1} = m\mathbf{a_1^{(1)}} + n\mathbf{a_2^{(1)}} = m'\mathbf{a_1^{(2)}} + n'\mathbf{a_2^{(2)}}$, with $\mathbf{L_2}$ being a 60° rotation of $\mathbf{L_1}$. With an appropriate choice of the unit vectors, the pair (m', n') may be set equal to (n, m). This pair relates to the twist angle according to the following relation [18]:

$$\cos\theta = \frac{1}{2}\frac{m^2 + n^2 + 4mn}{m^2 + n^2 + mn} \tag{2.2}$$

The length and surface area of the new unit vectors and unit cell are given by:

$$L = |\mathbf{L_1}| = |\mathbf{L_2}| = a\sqrt{m^2 + n^2 + mn} = \frac{|m - n|}{2\sin\theta/2}a \tag{2.3}$$

$$S = |\mathbf{L_1} \times \mathbf{L_2}| = \frac{\sqrt{3}}{2}L^2 \tag{2.4}$$

a being the lattice parameter of single layer graphene (SLG). As expressed in equation 2.3, the smaller the angle, the larger the superlattice unit cell. This feature will be of high importance for example in the presence of a magnetic field as a larger unit cell will capture a larger magnetic flux.

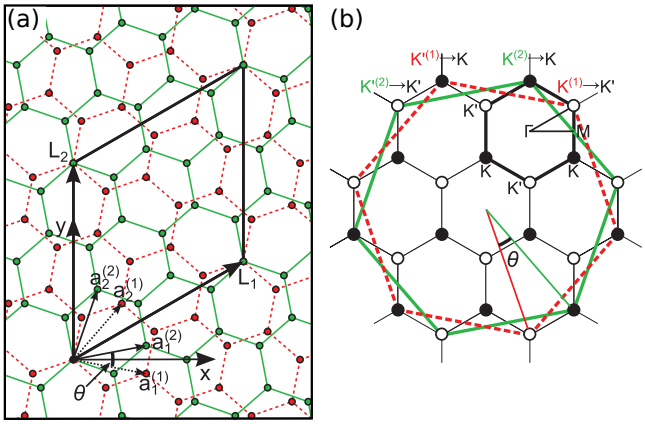


Figure 2.4: (a) Description of the new superlattice (black) for two layers twisted by an angle θ. The lattices of the two layers are represented in red (dashed) and green (solid), the angle here is commensurate. (b) Representation of the new Brillouin zone for the same angle, with the same colors as (a). Figure from [18].

This model, however, is not as complete as one could get as it does not take into account the cases of non-commensurate twist angles (e.g. 30°). In fact, the physics is continuous and so there is a need for a more general way of characterizing

such a structure. It turns out that exact periodicity of the atoms in the lattice is not the key to the electronic properties of such systems, which instead is to be found in a larger scale triangular periodicity called a Moiré pattern (see figure 2.5). The length of the Moiré unit vector, in opposition with the commensurate angle approach, evolves continuously. It is given by [19]:

$$L_M = \frac{a}{2\sin\theta/2} \tag{2.5}$$

The periodicity of the Moiré unit cell and the commensurate unit cell only coincide when $|m - n| = 1$. The Moiré pattern is illustrated in figure 2.5.

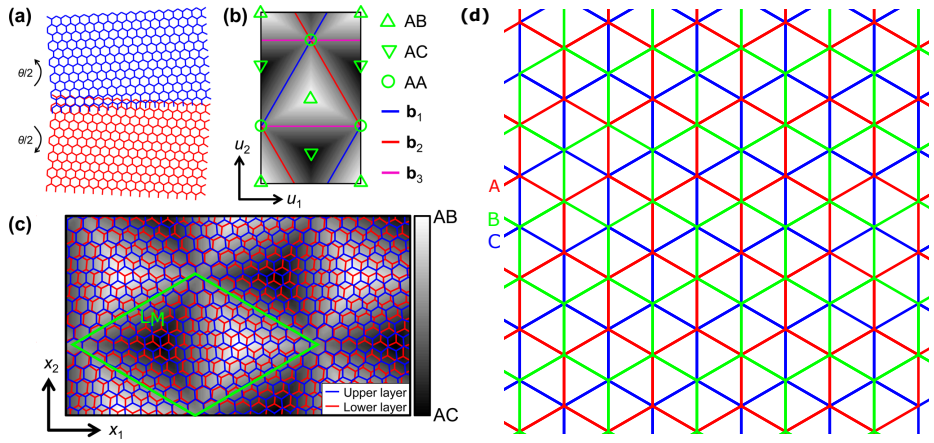


Figure 2.5: Moiré pattern with the specific alignment of the layers. (a) Illustration of the twist angle. (b) Moiré pattern mapped. (c) Layer lattices superposed on the Moiré pattern. The green diamond is the Moiré superlattice. (d) Possible relative alignments of the layers. (a,b,c) from [20].

In addition a translation could be added, but according to [18] the effect of such an action would be negligible and will thus not be considered.
As shown in figure 2.4, the physical unit cell getting bigger leads to a shrinking of the Brillouin zone by the same factor. This strongly limits the number of wave vectors accessible and will be part of the explanation for some observed phenomena.

2.3.2 Electronic structure of tBLG

tBLG's peculiar electronic properties arise from the peculiar shape of its band structure. As can be seen from figure 2.6, the width (in energy) of the lowest energy conduction band and highest energy valence band decrease with decreasing twist angles. This width decrease is faster than the simple scaling factor due to

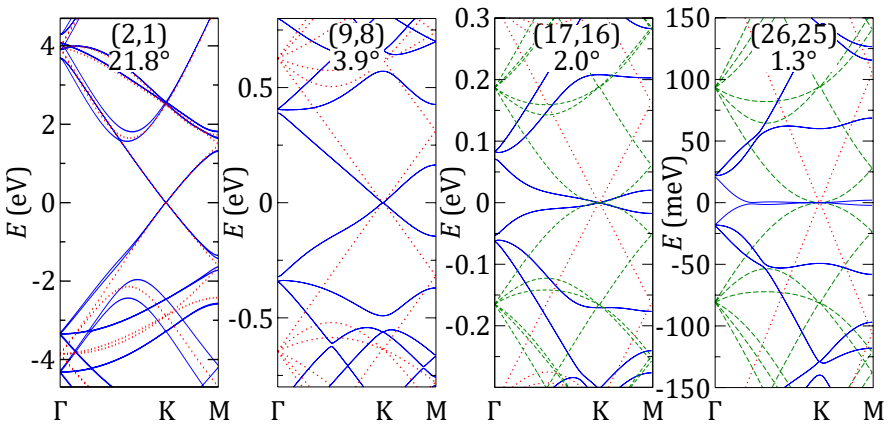


Figure 2.6: Band structure of tBLG at different twist angles. The integer pairs are the commensuration indices (m,n) discussed before. The blue lines are the calculated band structures. The red and green dotted lines show the band structures of SLG and Bernal stacked BLG respectively. Adapted from [21].

the reduction in size of the first Brillouin zone. In fact, these bands theoretically reach zero width at some precise angles called "magic angles". The first magic angle is $\sim 1.1°$, while the second is $\sim 0.5°$. An intuitive explanation for this phenomenon will be given later. The reader might have noticed that only specific angles were simulated, commensurate angles with commensuration indices (m, n) with $|m - n| = 1$. As mentioned in the previous section, these are the only indices for which the commensurate unit cell matches the Moiré unit cell. In fact however, the physics of these systems is continuous and the important unit cell is the Moiré unit cell. Only these commensurate angles are studied for practical reasons as they allow the system to be simulated with exact periodicity conditions. These systems are a real challenge to study using simulation tools given that a unit cell of tBLG with a twist angle below 1° contains more than 15000 atoms [21]. This is the reason why tight binding method are usually chosen instead of ab initio methods. Continuous models need to make strong hypotheses and try to fit with the discrete, commensurate simulations [22].
These flat bands have several important consequences. The first consequence is that, because of the flattening of the bands, the Fermi velocity (given by eq. 2.1) decreases by a few orders of magnitude near the magic angles. Another major consequence of these flat bands is to be found in the vicinity of another point of the Brillouin zone: the M point. At small angles, the interactions between states in the overlapping Dirac cones open a gap at the saddle point (M point) of the superlattice band structure (fig 2.7.a) [23, 24]. This newly formed gap, causes a flattening of the bands at the M point, which in turn shows up as a spike in the

density of states (DOS), called the Van Hove singularity (VHS) (fig 2.7.b). With decreasing angle and emergence of the flat bands, the VHS energy moves closer to the Dirac energy[6]. At $\sim 2°$ the VHS on both sides of the Dirac energy merge in one sharp peak (fig 2.7.c and 2.7.d). The low Fermi velocity also ensures a strong localization of these states. It turns out that the high DOS observed from the VHS is not uniform and is strongly localized in the AA stacked regions of the Moiré pattern [25] (fig 2.7.e).

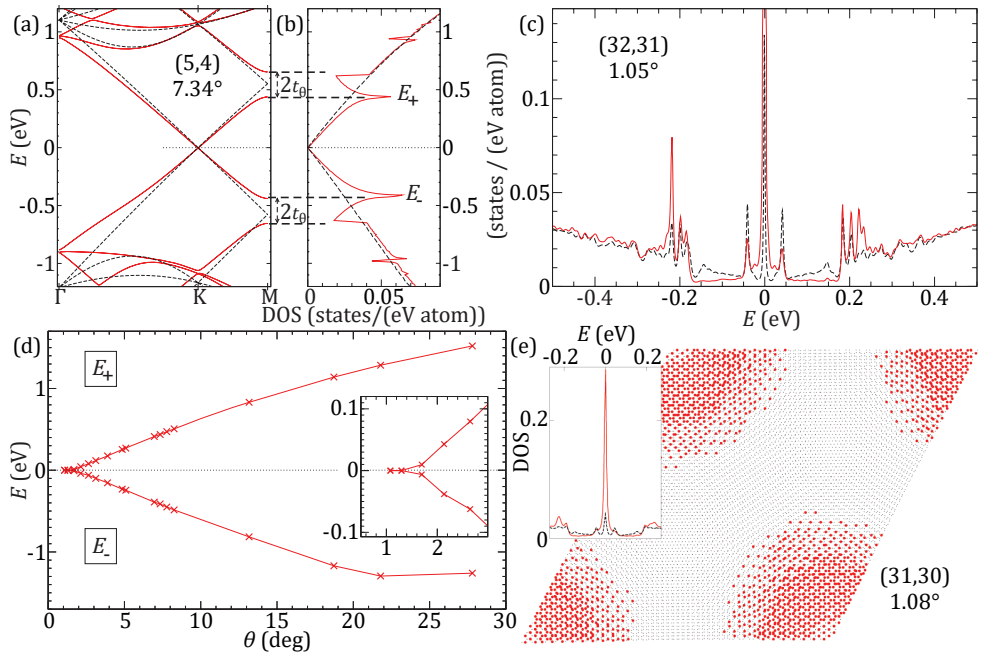


Figure 2.7: Evolution of the VHS in tBLG. (a) Band structure of tBLG with a twist angle of 7.34° with the emergence of a gap at the M point. The dashed line is the band structure of SLG. (b) DOS associated to the band structures in (a), the two peaks of the VHS are labeled E_+ and E_-. (c) DOS of a tBLG with twist angle 1.05°, the VHS on both sides have merged. (d) Energy of the VHS as a function of twist angle. (e) Localization of the states, the red dots are atoms on which 80% of the states are localized. The inset shows: red solid line: LDOS at the center of the AA region. Black dashed line: total DOS. (a-d) adapted from [24], (e) adapted from [25].

The reason these flat bands are responsible for such exotic effects is because small bandwidths correspond to low Fermi velocities and low kinetic energy. In that case the interaction potential between electrons becomes stronger and eventually

[6]The Dirac energy is the energy of the tip of the Dirac cone, the Fermi energy at charge neutrality

even dominant. This yields to strong correlation effects such as unconventional superconductivity, etc. (see later). Figure 2.8 shows the evolution, with the twist angle, of the bandwidth and of the Coulomb interaction energy from localized electronic states. Assuming localized electronic states in the AA stacked regions, the Coulomb potential energy could be expressed as [4]:

$$U = \frac{e^2}{4\pi\epsilon d} \tag{2.6}$$

with ϵ the effective dielectric constant, including screening and d the effective distance of interaction. d is not clearly defined, but, as localized states in AA regions are assumed, is of the order of magnitude of the Moiré lattice parameter. Hence, the product ϵd can be expressed as $\epsilon_0 \kappa L_M(\theta)$ with κ a dimensionless parameter close to unity. In the small angle approximation and using the expression of $L_M(\theta)$ (eq. 2.5), the potential interaction can hence be rewritten as:

$$U = \frac{e^2\theta}{4\pi\epsilon_0\kappa a} \tag{2.7}$$

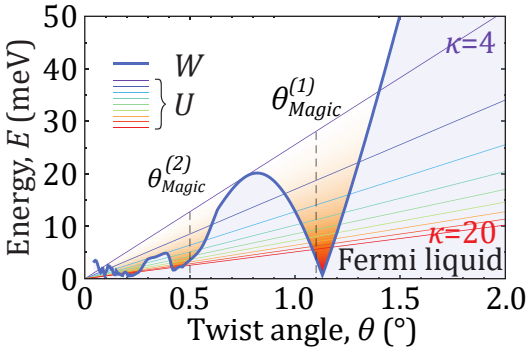


Figure 2.8: Bandwidth (W) and Coulomb potential from localized states (U) as a function of the twist angle for several values of κ. Figure from [4].

It is clear from fig 2.8 that, only near magic angle configurations, the Coulomb interaction potential energy may dominate over kinetic energy and strong correlation effect become visible.

As explained, the bandwidth theoretically reaches 0 at the magic angles, yielding completely localized electronic states. In practice however, this never happens because of lattice relaxation [26]. Because the stacking energy is higher for AA stacking than for AB stacking, the AA regions will tend to relax closer to AB and BA configurations. This creates large areas of AB and BA regions in a triangular

lattice, with small pockets of AA regions in between (fig 2.9.a and 2.9.b). This strain has the effect of significantly increasing the Fermi velocity, strongly suppressed before relaxation. Furthermore, the magic angle in relaxed lattices is slightly shifted compared to non relaxed (fig 2.9.d). Another effect of this relaxation is the opening of a band gap of several meV at the Γ point (fig 2.9.c).

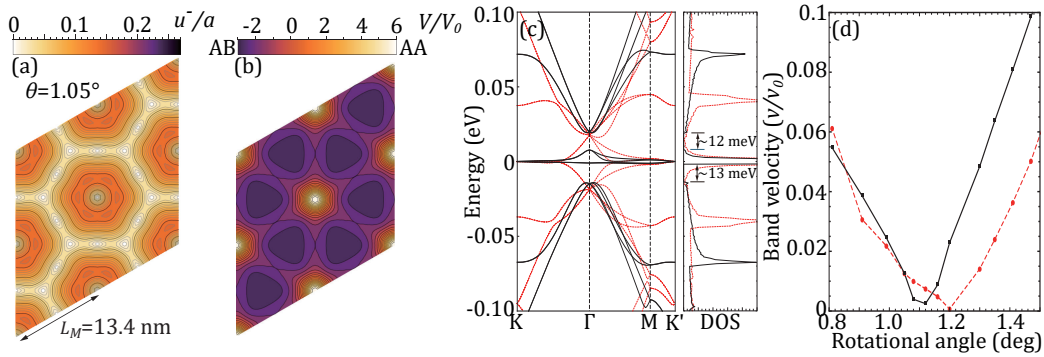


Figure 2.9: Effects of lattice relaxation. (a) Strain induced by the relaxation. u^- is the displacement vector. (b) Stacking potential. V_0 is the maximum "interchain energy" of the model used in the reference, essentially $6V_0$ is the stacking energy of AA and $-3V_0$ of AB stacked BLG. (c) Relaxed vs non relaxed lattice band structure (black and red, respectively). The newly created band gap is clearly visible in the DOS. (d) Fermi velocity in relaxed (black) vs non relaxed (red) lattices. Adapted from [26].

A last interesting feature about the magic angle is that is varies with pressure, due to compression. In the absence of any pressure, the first magic angle is situated at 1.1°, but at higher pressures, it increases, e.g. at 9.2 GPa (10% compression) the first magic angle becomes $\sim 2.0°$ [27].

Intuitive understanding of the flat bands

Cao et al. (2018) [4] propose an intuitive explanation, illustrated in figure 2.10 for the emergence of flat bands. As mentioned in the previous section, increasing the size of the Moiré superlattice would decrease the size of the first Brillouin zone. This would bring the two new Dirac points closer and closer together until the Dirac cones merge (fig 2.10.a and 2.10.b). Before completely merging, the Dirac cones interact and form hybridized bands, creating a band gap of $2w$ (fig 2.10.c). This is also the gap responsible for the VHS. It is also assumed that the gap remains constant with decreasing twist angle. This is a reasonable assumption given the linear evolution of the position of the VHS, seen in figure 2.7.d. Furthermore,

the spacing between both Dirac cones in the reciprocal space is labeled k_θ. With decreasing angle and increasing Moiré supercell, k_θ decreases. The Fermi velocity is deduced from the dispersion relationship with following expression:

$$v_F = \frac{1}{\hbar}|\nabla_{\mathbf{k}} E_{\mathbf{k}}|_{\mathbf{k}=K,K'} \tag{2.8}$$

In single layer graphene, this Fermi velocity is labeled v_0 and is roughly equal to 10^{-6} m/s. Using this, we can calculate the difference in energy between the charge neutrality point and the fictional point of intersection between the two Dirac cones. This difference is given by $\hbar v_0 k_\theta/2$ (fig 2.10.b), assuming that the Dirac cones are perfect cones with perfectly linear dispersion. From these conclusions, it makes sense intuitively that when this energy difference approaches the gap w between the two hybridized bands, the lowest conduction band and highest valence band have "no choice" but to be flattened out (fig 2.10.d). Finally, for small angles, the spacing between the Dirac cones can be approximated by $k_\theta \approx G_K\theta$, with $G_K = 4\pi/(3a)$ being the difference in wave vectors between the Γ and K points in single layer graphene. With all of this, the magic angle can be estimated by:

$$\theta_{Magic} \approx 2w/(\hbar v_0 G_K) \tag{2.9}$$

Using $w = 110$ meV, based on the electronic structure of Bernal stacked BLG [28], a surprisingly accurate magic angle of 1.12° is calculated. Mathematical derivations yield a first magic angle given by $\sqrt{3}w/(\hbar v_0 G_K)$ [4].

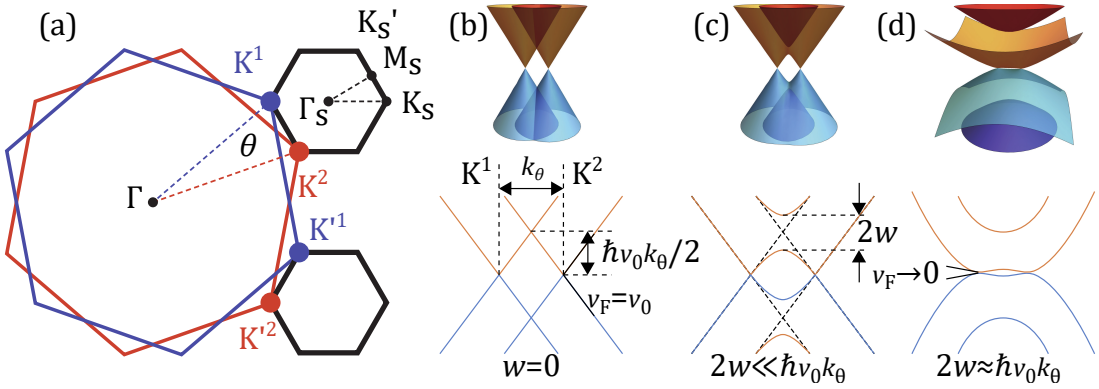


Figure 2.10: Intuitive understanding of the formation of the flat bands. (a) First Brillouin zone of the tBLG (black) from the first Brillouin zones of the two graphene layers (red and blue). (b) Overlap of non interacting Dirac cones. (c) Interaction and merging of two Dirac cones. (d) Band structure close to the magic angle. Figure adapted from [4].

This explanation works for the first magic angle, but doesn't explain the others. Intuitive explanation for the other magic angles can be found with another approach

[22]. This has to do with the observation that, at the magic angle, there is a strong localization of the electrons in the AA stacked regions. The band structure of AA stacked bilayer graphene at the K point can be seen as two Dirac cones, one shifted up and one shifted down by a quantity $\pm t_\perp$ (fig 2.11.a). Therefore, the wave vector of electrons at the Fermi surface ($E = 0$) is given by $k = t_\perp/(\hbar v_0)$.

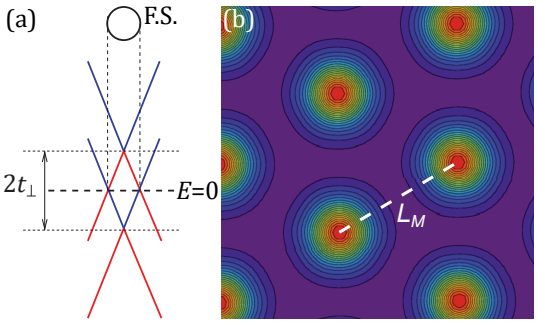


Figure 2.11: (a) Band structure of AA stacked BLG. (b) Moiré pattern, the red discs are the AA regions. Adapted from [22].

Strong localization in the AA regions can be expected periodically when:

$$k \cdot L_M \approx 2\pi n \tag{2.10}$$

With n an integer. Furthermore, for small angles, $L_M \approx a/\theta$. This yields a rough approximation for the magic angles:

$$\theta^{(n)}_{Magic} \approx \frac{1}{2\pi}\frac{t_\perp}{\hbar v_0}\frac{a}{n} \approx 1.08^\circ \frac{1}{n} \tag{2.11}$$

With $t_\perp \approx 0.3$ eV experimentally measured. This indeed yields a sequence of magic angles, with the first two being close to reported values of 1.1° and 0.5°.

2.3.3 Reported and expected phenomena

Twisted bilayer graphene is home to a great number of exotic properties, most of which arise from the dominant effect of electron electron correlations. This section highlights some of the properties observed. Other interesting properties include strange metal behavior [29], the emergence of ferromagnetism [30] or the creation of helical edge states [31].

Superconductivity and Mott-like insulating state

In 2018, Cao et al. [4, 5] first observed two closely related, yet opposite phenomena in magic angle tBLG: Mott-like insulating and superconducting states. This major

discovery was named "breakthrough of the year 2018" by the magazine Physics World. The phenomenon has since then been confirmed by several other groups [32, 33, 34]. The exact mechanism behind these phenomena (especially the superconductive state) is not yet clearly understood because of the challenge posed to model such systems. The Mott-like insulating states are observed at integer filling factors, while the superconducting states appear in between the integer filling factors. The filling factor is a measure of electronic doping of the crystal and it is measured as the number of extra electrons per unit cell. In the case of (first) magic angle tBLG the Moiré unit cell has an area of $A = \sin(60°)L_M^2 \approx 142$ nm^2, hence a filling factor of $\nu = 1$ corresponds to an electronic density of $n = 1/A \approx 0.70 \cdot 10^{-12}$ cm^{-2}. Because of the spin and valley degeneracy, complete filling of the conduction band corresponds to a filling factor of $\nu = 4$. Figure 2.12 shows the electrical resistance behavior of tBLG as a function of temperature and doping. Superconducting and Mott-like insulating states have been observed at twist angles close to the magic angle, down to 0.93° [33] and up to 1.27° under pressure [32].

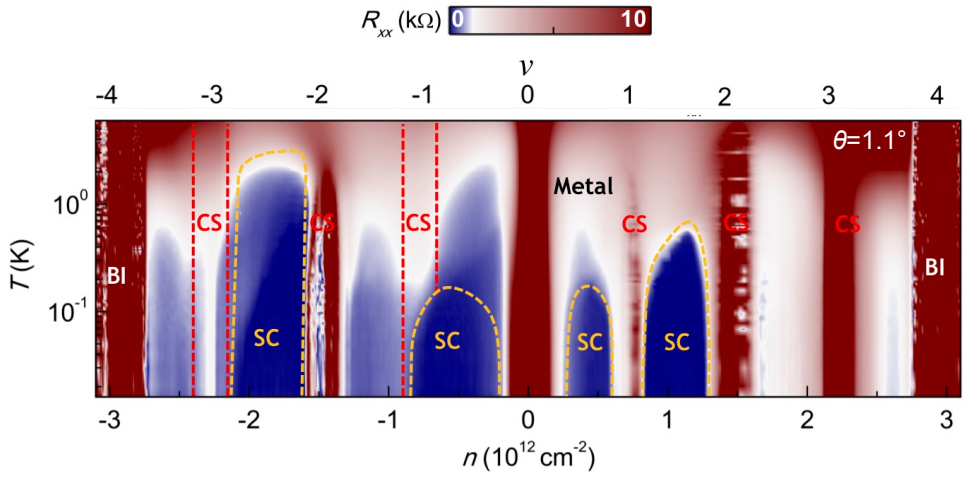


Figure 2.12: Resistance as a function of doping level and temperature for a 1.1° angle tBLG. Different states are labeled: band insulator (BI), insulating state at full filling of the bands; correlated states (CS), Mott-like insulating state at integer filling factors; superconducting state (SC); Metallic state (Metal). Figure from [34].

Mott insulator are special insulating states observed in conductors at half-filling of their conduction bands. In conventional band theory, a half filled conduction band is supposed to lead to a metallic behavior. In the case of Mott insulators, the electron-electron interactions split the conduction band in two sub-bands separated by a band gap. In tBLG, this is likely due to charge localization in the AA regions at the magic angle. In fact, Mott-like insulating states appear at every integer filling factor, not only at half filling. Similar mechanisms might still be

at stakes at these filling factors, with a (partial) lifting of the spin and valley degeneracy [32]. The insulating behavior in tBLG is called "Mott-like" because the behavior is similar to Mott insulators, but there is still debate over the real origin of these features [35]. Similar insulating states have also been observed at filling factors of $\nu = \pm 5$, corresponding to quarter filling of a higher energy band [33].

The main feature of the map presented in figure 2.12 is of course the superconductivity. The critical temperature (T_c) of these superconductors has been measured as high as 3 K [32, 34]. This critical temperature might seem low, but it is actually very high compared to the Fermi temperature of tBLG. The effective Fermi temperature for 2D materials is proportional to $T_F \propto n_{s,2D}/m^*$ [36] ($n_{s,2D}$ is superconducting charge carrier density and m^* is the effective mass of the electrons). The ratio T_c/T_F is a measure of the coupling strength of the electron pairs in a superconductor. The superconducting states in tBLG occur near half integer filling factors and because of the large unit cell, these correspond to low charge carrier densities. This means a $n_{s,2D}$ and hence T_F orders of magnitude smaller compared to other superconductors. Therefore tBLG has one of the T_c/T_F among the highest found in all superconductors [5].
The strong coupling between the electrons and the presence of a Mott-like state are features also found in cuprates. This lead Cao et al. to classify the observed superconductivity as "unconventional"[7] and speculate that it originated from strong electron correlations instead of weak electron-phonon interactions. This hypothesis has since then been questioned by several groups [38, 39, 40] claiming the origin might be phonon driven after all. This topic is, at the moment of writing this thesis, subject to an intense theoretical debate.

[7]Unconventional superconductivity refers to superconductivity phenomena where the Cooper pairs are not bound together through phonon-exchange, but through other mechanisms [37]

Hofstadter's Butterfly in the quantum Hall effect

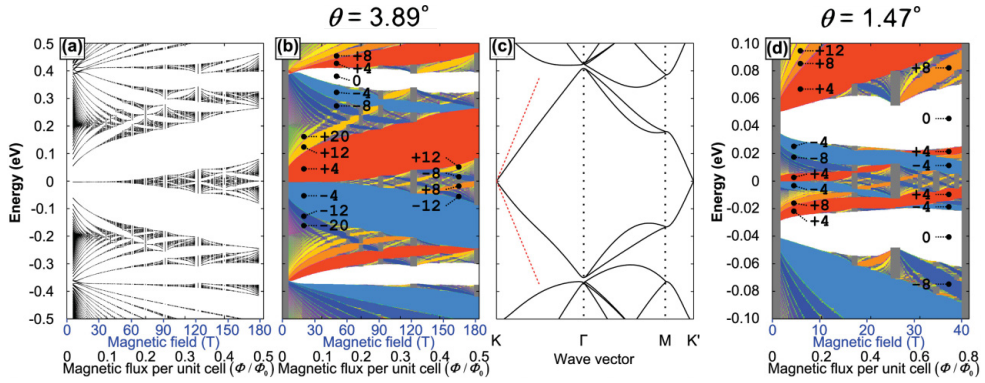


Figure 2.13: Hofstadter's butterfly structure in the QHE. (a) Landau levels as a function of magnetic field. (b) Same structure as (a) with the associated quantum Hall conductance. (c) Band structure of the tBLG. (a,b,c) are calculated for a twist angle of 3.89°. (d) Idem as (b), except for a 1.47° twist angle. The Hall conductance is expressed in units of $-e^2/h$. Figure from [18].

It has been predicted that 2D electronic systems under the influence of a periodic potential and perpendicular magnetic field are very sensitive to the ratio "magnetic flux per unit cell"/"magnetic flux quantum"[8] [41]. In those systems a fractal structure of the Landau levels is expected and takes the form of a mathematical structure called Hofstadter's butterfly (fig 2.13.b). This fractal structure would be visible in the Hall conductance measurements. For atomic size unit cells, this would require magnetic fields about 1000× stronger than what is technically feasible [42]. The idea then quickly arises to try to observe this phenomenon using tBLG superlattices, as increasing the unit cell size would drastically reduce the required magnetic fields. Figure 2.13 shows the expected phenomenon.
The fractal structure can be observed for magnetic fields whose characteristic length scale ($l_B = \sqrt{\hbar/(eB)}$) is smaller than the size of the unit cell (L_M). Then, the uncertainty on the momentum of an electron ($2\pi/l_B$) would be greater than the first Brillouin zone. This means for magnetic fields (in tesla) greater than $\sim 3.3 \times \theta$ with θ in degrees [18]. In order for this to be experimentally accessible, twist angles close to $\sim 1°$ are required. These being angles close to the magic angle, it explains why the "wings" of the butterfly are squeezed. In fact, there are two types of contribution to this structure: the electron-like Landau levels, close to the K and K' points, and the hole-like Landau levels, close to the Γ point. The electron-like Landau levels contribute to the sequence of Hall conductivity increasing by steps of

[8] Magnetic flux quantum $= \phi_0 = h/(2e) \approx 2.1 \cdot 10^{-15}$ Wb

8 ($-e^2/h$) because of the spin, valley and layer degeneracy. The hole-like Landau levels contribute to the sequence with steps of -4 ($-e^2/h$) because there is only one Γ point and so no valley degeneracy. In the flat bands, the bands are getting squeezed faster around the K and K' points than around the Γ point. This is the reason for a faster flattening of electron-like Landau levels compared to the hole-like Landau levels.

Quasi-crystal

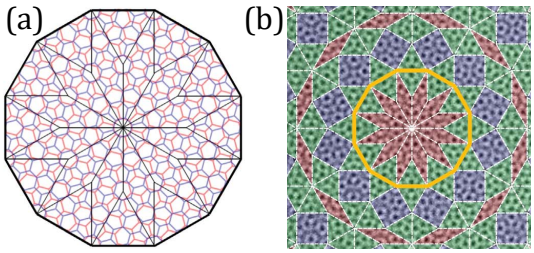


Figure 2.14: Structure of 30° tBLG. (a) Close view of the alignment of the lattices. (b) Large scale view of the created patterns. Figure from [43].

Not all the peculiar properties of tBLG occur at small twist angles. At a twist angle of exactly 30° a 12-fold rotational symmetric quasi-crystal is created. A quasi-crystal is an ordered, but non periodic structure (see figure 2.14). The non periodicity is easily checked by seeing that 30° doesn't respect the commensuration condition (cfr. Appendix A) and at such large angles, no Moiré pattern can be drawn. These structures have been studied with other materials (e.g. Copper covered by CO [44]), but all of which hosting non relativistic electrons. Graphene based quasi-crystals allow for a material study of quasi-crystals with relativistic electrons and could challenge current our theoretical understanding of matter, such as exhibiting properties related to 4 dimensional QHE [45]. Interestingly, 30° tBLG shows different electronic properties than tBLG with a commensurate twist angle close to 30° [43]. Another interesting phenomenon observed with these graphene quasi-crystal is superlubricity, meaning the absence of (or very small) frictional force between the layers [46].

Chapter 3

Fabrication process

This chapter presents a detailed overview of all steps in the fabrication process of twisted bilayer graphene. Appendix B provides a process sheet summarizing most of the content of this chapter.

3.1 Desired sample

In the case of this work, the desired sample is a magic angle tBLG. The magic angle is chosen as twist angle for electronic reasons, but the fabrication process is identical regardless of the angle. This tBLG sample would be encapsulated between two h-BN flakes in order to improve electron mobility and hence the quality of future measurements. The electronic properties of a sample may indeed be heavily influenced by the substrate carrying it. For a whole bunch of reasons, its structural resemblance with graphene to begin with, h-BN turns out to be close to the ideal substrate for graphene based devices. The top h-BN flake also plays an important role useful for two reasons. The first one is practical, as it will help with the fabrication of the tBLG device. The second reason is to protect the stack from lithography resists and air, having undesired effects on the properties of the device [47, 48]. Graphene devices encapsulated in h-BN exhibit the highest charge carrier mobilities achieved in the literature [49].
In fact, h-BN substrates may, in some situations, have a negative impact on the electronic properties of graphene. This happens when the misalignment between the h-BN and graphene lattice is of less than 1° [50]. However, if the relative orientation between them is considered random, the chances of this to occur are negligible (1/30 given the rotational symmetry).

In order to perform all kinds of electronic measurements, the sample is shaped into a Hall bar. This allows for the possibility to place up to six contacts to

the samples. Six contacts are useful as typical electronic measurements require four or five contacts (two for the current and two or three for the longitudinal and potentially Hall voltage) and there is always a possibility of a failed contact, hence having back up contacts is necessary. Figure 3.1 shows a scheme of the desired sample. The dimensions of the samples depend on the size of the flakes. On the one hand, the Hall bar must fit into the area of twisted bilayer graphene of the sample, accounting for the possibility of a slight misalignment during the lithography process. On the other hand, the larger the Hall bar, the easier it becomes to place the contacts and the less significant boundary effects become. Typical dimensions of the twisted bilayer graphene range from 6 µm × 4 µm to 20 µm × 10 µm. This means Hall bar geometries ranging from 5 µm × 3 µm to 15 µm × 7 µm.

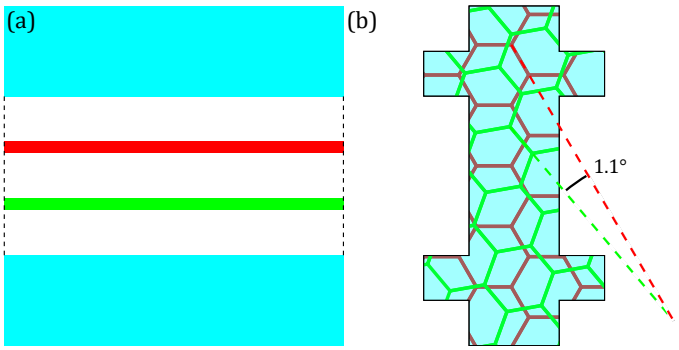


Figure 3.1: Scheme of the desired sample. (a) Drawing of the different layers present in the sample. The blue layers stand for h-BN, the red and green layers for graphene. (b) Top view of an ideal sample, shaped as a Hall bar. The twist angle is exaggerated for graphical purposes.

3.2 Mechanical exfoliation

There are several ways to get graphene flakes, all with different advantages. Here is a short overview of the most popular techniques with their advantages [51, 52, 53]:

- **Liquid phase and thermal exfoliation:** Graphene is isolated from graphite using a solvent whose surface tension favors exfoliation of graphene. Ultrasonic mixing allows for individual graphene sheets to be detached and suspended in the solvent. These are then extracted, usually using centrifugation. Variants exist, e.g. using graphite oxide instead. The main advantages are the ease with which film size can be scaled up and the fact that it is a rapid process. Its main drawback is the poor charge carrier mobility in the obtained graphene.

- **Chemical vapour deposition (CVD):** A hydrocarbon molecule (called precursor) such as methane is heated to about 1000°C in a furnace containing a metallic substrate (typically copper). The molecules decompose at such temperatures and the carbon atoms cluster to form large domains of graphene. This method is rapidly improving and could soon be key for industrial applications. Its main advantages is the reasonably high quality (second best method after mechanical exfoliation) and the size (up to 1 cm) of the flakes. The main drawback is that transfer from the metal is needed and can be problematic.

- **Synthesis on SiC:** A silicon carbide wafer is heated to more than 1000°C, hence sublimating the Si atoms. The carbon atoms are left behind and create a graphitized surface. The advantages here are the fact that the graphene doesn't need to be transferred anymore (SiC can be used as a wafer) and the high evenness between different films. Its main drawback is the energetic cost of the method (very high temperatures).

- **Mechanical exfoliation:** The description for this method is in the next section. Mechanical exfoliation doesn't require any special equipment and the method is easy to reproduce. Furthermore, this method provides the flakes with the highest charge carrier mobility of all methods. The main drawbacks of the method are the unpredictability of the size of the produced flakes and its labor intensive aspect.

For the study of electronic properties of a material, the electronic mobility needs to be as high as possible among the available methods. For this reason, in the case of this thesis, mechanical exfoliation seems to be the ideal way to produce graphene flakes. Figure 3.2 emphasizes the qualitative superiority of mechanically exfoliated flakes. Furthermore, mechanical exfoliation doesn't require any expensive equipment and is thus always available. However, progress in CVD methods could also allow for the use of CVD graphene in the future. Indeed, high mobilities have been observed in CVD samples up to 350000 $cm^2\ V^{-1}\ s^{-1}$ at 1.6 K [54]. The larger size of CVD produced flakes would make them much easier to manipulate.

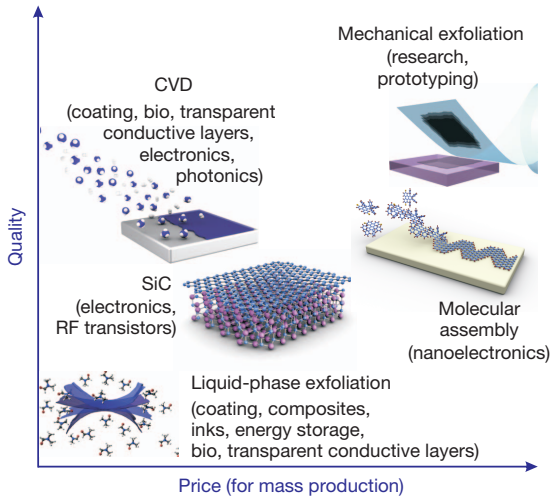


Figure 3.2: Map of the several production methods for graphene flakes. Figure from [51].

3.2.1 Graphene

Figure 3.3 shows a schematic drawing of the procedure of graphene exfoliation. The idea is to tear apart atomic layers in graphite until only one remains. The layers involved need to be of the highest quality in order to obtain high quality graphene as an end product. For this reason, extremely pure natural graphite is used as starting material. An alternative is highly oriented pyrolytic graphite (HOPG), with even higher crystalline perfection. This being a rather random process, many flakes need to be made in the hope that some of them will only be one layer thick and large enough for further use. The procedure is the following:

- A thin line of graphite grains are laid down on some tape (ideally Scotch Magic Tape). One end of the tape is stuck on the table while the other remains free (fig 3.3.a).
- The free end of the tape is folded back onto the other end, hence encapsulating the graphite line between the two sticky sides (fig 3.3.b). Good adhesion is ensured by pressing on the tape around the graphite line (not on it in order not to break the flakes) (fig 3.3.c).
- The free end is then quickly separated from the other end, tearing the graphite grains apart. Two lines of graphite (one on each side of the tape) are now visible.

- This procedure is repeated a few times, each time shifting the lines of graphite w.r.t. each other. This creates a larger area filled with bits of the original graphite flakes (fig 3.3.d).

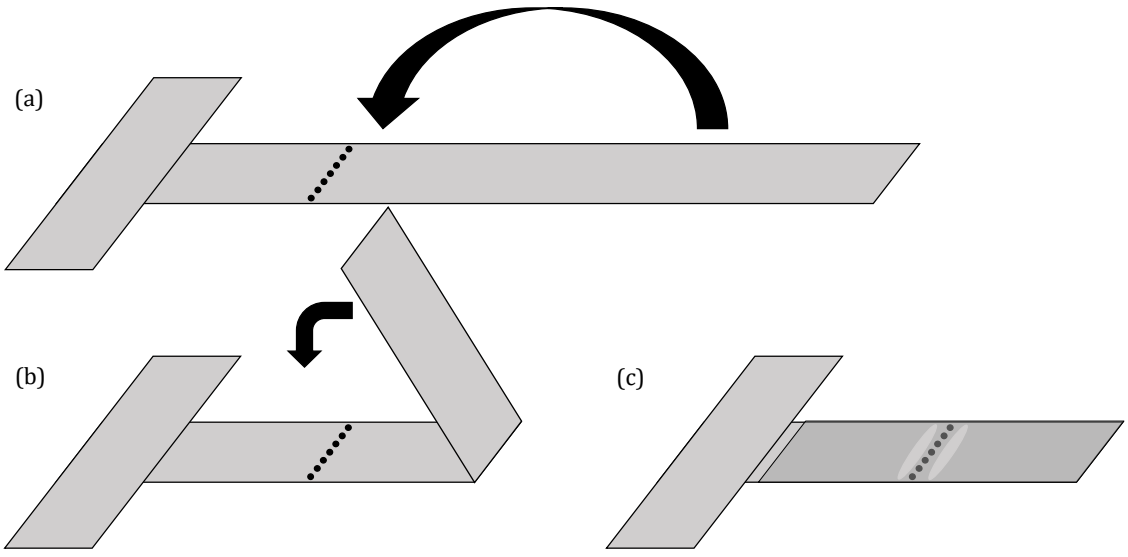
- A few, roughly 1 cm $\times$ 1 cm Si/SiO_2 wafers are first cleaned with acetone in an ultrasonic cleaning machine for $\sim$ 3 min, then rinsed with isopropanol and dried with nitrogen. Afterwards, they are cleaned in O_2 plasma at 40 W for 60 s. The purpose of this entire cleaning step is to remove all possible dirt to increase the adherence between graphene and SiO_2. The O_2 plasma removes all ambient adsorbates from the substrate [55].

- After cleaning, they are laid with the SiO_2-side on the tape (fig 3.3.e). The tape is then detached from the table, cut and put on glass slides with the sticky side (and thus the Si/SiO_2 wafers) up.

- The slides are put on a heating plate for several minutes at 90°C (fig 3.3.f). The purpose of this step is to maximize the uniform contact area between the flakes and the substrate [55].

- Once hot, the tape is pressed against the wafers, again by pushing next to the wafer and not on it to preserve the flakes. After that, it is peeled off the wafers, leaving some flakes on the SiO_2 part of the wafer.

- The highest quality flakes are identified and referenced with optical microscopy. The best flakes are the largest contiguous flakes, isolated from any other thicker flake that might make it harder to pick up the graphene.



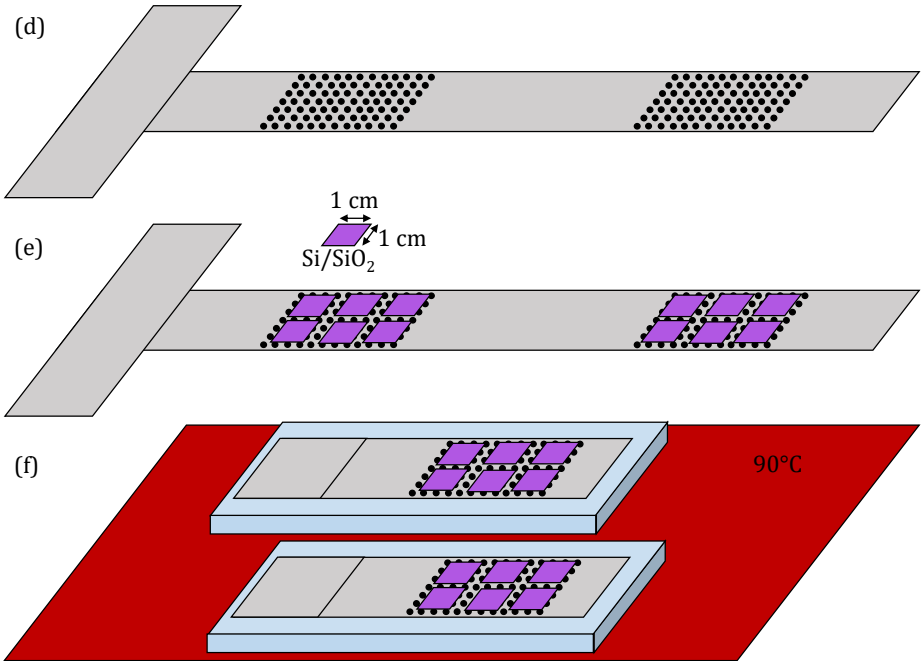


Figure 3.3: Scheme of the exfoliation procedure.

The color of the flakes under optical microscopy is determined by their thickness. Indeed, graphene's optical absorption of $\pi\alpha \approx 2.3\%$ is enough to create a visible optical contrast. This makes it possible for graphene to be seen under optical microscopy just by looking for contrast with the background. The Si/SiO_2 wafer's high reflectivity is important to increase the contrast as it makes light pass twice through the graphene layer before being observed. Thicker flakes absorb more light and lead to a greater contrast. The color also changes with thicker flakes due to Fabry-Perot type interference. Figure 3.4 shows a flake where different thickness steps are visible, the last one being graphene as confirmed with Raman spectroscopy (see later). The optical contrast observed under the microscope being small (left), this process of sample analysis needs to be performed slowly and at high magnification. This is the most time-consuming step.

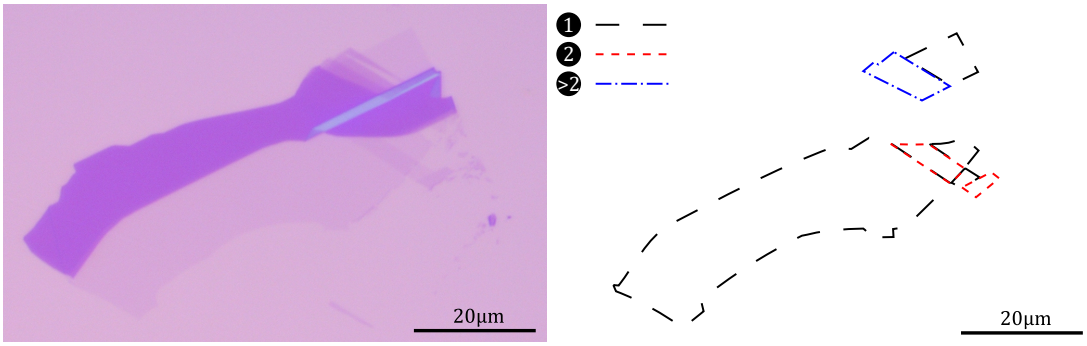


Figure 3.4: Optical microscope image of a graphene flake. Left is the unmodified image as observed under the microscope. Right is the same image with increased contrast and different thicknesses highlighted. The numbers in the black discs indicate the number of layers in each region.

3.2.2 h-BN

The exfoliation procedure of h-BN is similar to that of graphene, but still has some differences, represented schematically in figure 3.5. The main difference is the scarcity of the raw material. In order to limit the waste of raw h-BN a different strategy is adopted. The original line of h-BN grains is this time only limited to ± 1 cm (roughly the size of the wafers). Then, the tape is folded similarly as it is for graphene, but this time the operation is repeated only until the regions with bits of h-BN have a size of roughly 1 cm $\times$ 1 cm (fig 3.5.a). Then, two new bits of tape (this time ideally Scotch Magic Greener Tape) are stuck onto those regions (fig 3.5.b), before being peeled off. The Si/SiO_2 wafers are then stuck on those "Greener"-tape bands (fig 3.5.c). After pressing the tape against the wafer, the tape is very slowly peeled of the wafer. The original tape is never in contact with the wafers and is instead protected and kept until the next batch of exfoliation. This allows to waste as little h-BN as possible. Other differences in the procedure of exfoliation of graphene and h-BN are that, this time, the wafers don't need to be cleaned with O_2 plasma and there is no need for heating before peeling off the tape. This is because h-BN doesn't have to be single layer. Hence, far more usable flakes are created in each batch and there is no need for such thorough cleaning. Finally, the best h-BN flakes are identified and registered. The ideal flakes are perfectly flat (i.e. no glue left, no step in the number of layers, etc.) and of a size suited with the targeted flake of graphene (see later in the "stacking" section). They are also not too thick nor too thin (dark purple or blue flakes are ideal). This is because too thick flakes render further process steps more difficult and too thin flakes are too hard to pick up. Ideally the flatness of the flakes should be checked with an atomic force microscope (AFM). It is also possible to clean the h-BN flakes of most of the

remaining glue by heating them at $\sim 300°C$ in vacuum for ~ 2 h.

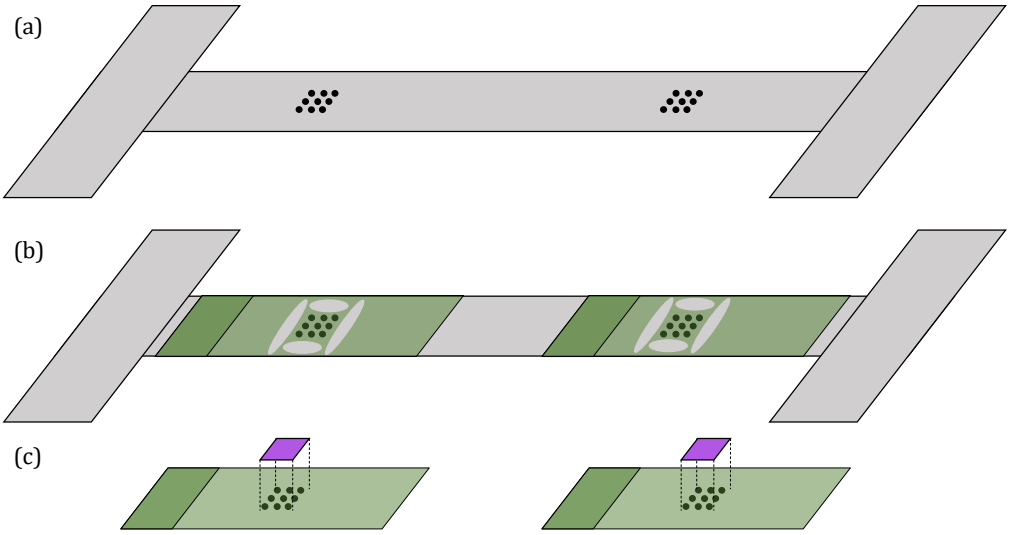


Figure 3.5: Scheme of the h-BN exfoliation procedure.

3.3 Raman spectroscopy

Up to this stage of the fabrication, graphene and h-BN flakes have been produced and potential candidates identified. Before moving on to the stacking of the different layers, it is important to make sure that it is indeed single layer graphene that will be used for the sample. Optical microscopy allows for a globally successful identification of graphene flakes, but a non-destructive method that would rule out any other possibility is required. The technique used is Raman spectroscopy, which will be discussed in this section. Raman spectroscopy presents the advantage of being able to clearly distinguish SLG from multilayer flakes. It is also able to "see through" the h-BN in a completed stack as will be discussed further.

3.3.1 Working principle

Raman spectroscopy is a non-destructive characterization technique of materials based on their vibrational modes (i.e. phonons) [56]. These vibrational modes being specific to every material, they allow the identification of the material. A Raman spectrometer works with a monochromatic laser (ranging from UV to near infra-red) shining through an optical lens onto the location to be analyzed. During interaction with matter, there are two ways light can be scattered by phonons: elastically or inelastically. Elastic scattering is commonly known as Rayleigh

scattering while inelastic scattering is known as Raman scattering. In Raman scattering, if the wavelength of the scattered photon has increased after scattering, it is called Stokes shift, otherwise it is called anti-Stokes shift (see figure 3.6). Of course, as energy is conserved, if a photon gains/loses energy, the exposed matter has shifted to a lower/higher vibronic state. The analysis of the scattered light is what a Raman spectrometer does. This yields a map of the energy transitions in vibrational modes of the material. The difference in energy between the incoming and scattered photon is called the Raman-shift. It is usually expressed in the difference between the wave numbers and hence expressed in cm^{-1}. Because of that, it can be calculated in the following way:

$$Raman\ shift = \frac{1}{\lambda_0[cm]} - \frac{1}{\lambda_1[cm]} \tag{3.1}$$

Where λ_0 and λ_1 represent the incoming and scattered wavelength respectively. The Raman shift is positive in the case of Stokes shifts because those are transitions from a lower to a higher energy level. These are more likely than the opposite and hence the ones measured in conventional Raman spectroscopy. The choice of the laser doesn't affect the measured Raman shift, but still affects the measurements. The choice of the laser must be made depending on sensitivity (Raman intensity $\propto \lambda^{-4}$), spacial resolution (diffraction limit $\propto \lambda$) and adapted to the material measured. In the case of carbon materials, blue or green lasers are especially adapted [57] and in the literature, three different lasers are commonly used: 514, 532 and 633 nm. The spectrometer used (LabRAM HR) has four available wavelengths (458, 488, 514 and 633 nm). For these reasons, the 514 nm laser will be mainly used in works of this thesis. Finally, the intensity of Raman peaks depends on a lot of parameters from measurements, including the device used. For this reason, the intensity is always measured in arbitrary units and only the relative intensity of the peaks and their position matter.

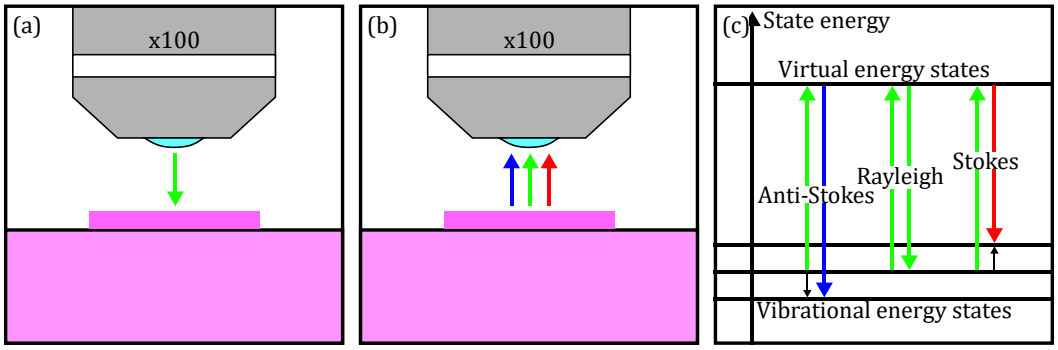


Figure 3.6: Schematic representation of Raman spectroscopy. (a) Incoming laser through an optical microscope on the flake. (b) Scattered photons from the flake back to the analyzer. (c) Schematic representation of the energy transitions. The little black arrows represent the Raman shift.

3.3.2 Graphene

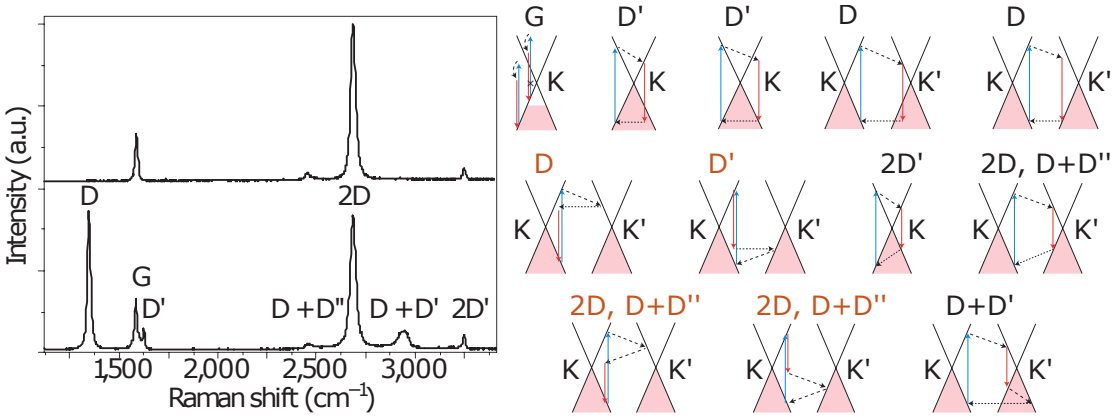


Figure 3.7: Left is typical spectrum of pristine graphene (up) and defected graphene (down). The different observable peaks are labeled. Right are the different transitions responsible for each peak. The solid lines represent the electronic band structure of graphene in the vicinity of the Dirac cones. The shaded region represent occupied states. The blue and red arrows represent the absorbed and emitted photon respectively. The momentum of the photons are neglected. The black dashed arrows represent the emitted phonons in the transitions. The black horizontal dotted arrows represent the effect of scattering on defects. Adapted from [58].

Figure 3.7 shows the different peaks observed in the typical range of Raman spectroscopy of graphene: $1200 - 3500$ cm^{-1}. The top left spectrum is the spectrum

of pristine graphene [1], while the bottom left spectrum shows all the peaks observable in the presence of defects. Mechanically exfoliated graphene being of the highest quality available (cfr. fig 3.2), the defect-related peaks are almost non-existent. Four peaks will be discussed in this section as they tell the most about the nature of the graphene samples. These peaks are the D-peak, G-peak, D+D" peak and 2D peak.

- **D-peak**: ~ 1350 cm^{-1}: Main peak originated from interactions with defects. The presence of this peak would indicate poor quality of the graphene flake.
- **G-peak**: ~ 1580 cm^{-1}: Originates from in-plane vibrations of sp^2 carbon atoms at the center of the Brillouin zone (Γ-point). This peak is doubly degenerate. [59] Originating from in-plane vibrations, this peak is common to all graphite-like structures.
- **G* or D+D"-peak**: $\sim$ 2450 cm^{-1}: Originates from double resonance processes along the KΓ line of the first Brillouin zone [60]. This peak will be used to confirm the thickness of flake, determined by the 2D-peak.
- **2D-peak**: $\sim$ 2680 cm^{-1}: Also labeled as the G' peak in the literature. This peak also originates from double resonance processes between the K and K' point of the first Brillouin zone [61]. This peak will be of major interest in differentiating SLG from thicker flakes and in evaluting the twist angle in tBLG.

[1] Pristine graphene means ideal, defect-less graphene.

Thickness resolution

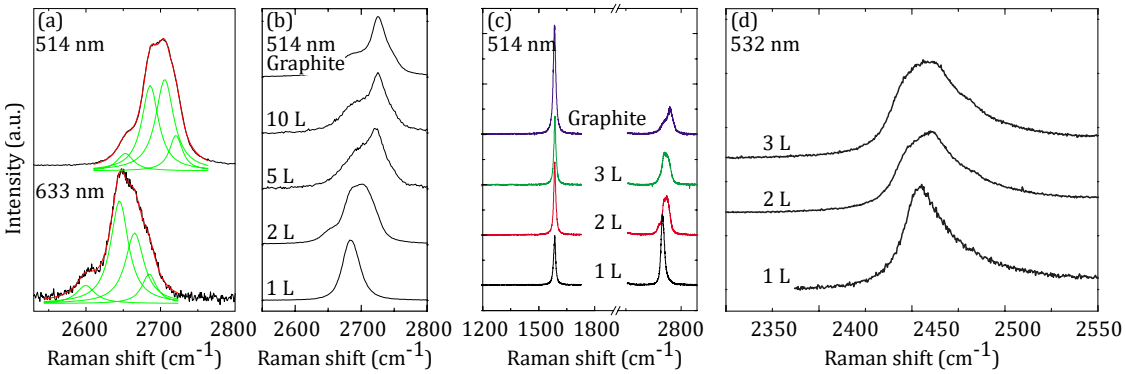


Figure 3.8: Influence of the number of layers on the shape of the 2D and D+D" peaks. (a) Shows the different Lorentzian contributions to the 2D peak in bilayer graphene. (b) shows the overall dependence of the 2D peak, w.r.t. the number of layers. Increasing number of layers create an asymmetry in the peak due to increasing number of modes contributing to the peak. (c) shows the relative intensity of the 2D peak w.r.t. the G peak. (d) shows the dependence of the D+D" peak, w.r.t. the number of layers. Single layer graphene produces a very sharp peak, the more layers, the rounder the peak. (a,b) adapted from [62]; (c) adapted from [63]; (d) adapted from [60].

The two main peaks that will be used for identifying the thickness of a flake are the D+D" peak and especially the 2D peak. Figure 3.8 shows their respective evolution for different thicknesses. In fact, the amplitude of the G peak also changes with the number of layer, reaching a maximum at 9 layer graphene [59], but the difference is too subtle to be grasped from the naked eye, especially given the powerful other identification means at our disposal. The D+D" quickly transitions from a sharp peak in single layer graphene, to a rounder peak for thicker flakes (fig 3.8.d). The 2D peak changes in two ways, depending on the thickness of the flake. First, its intensity relative to the G-peak drops going from SLG to thicker flakes (fig 3.8.c). For SLG the 2D peak is more intense than the G peak and less intense for thicker flakes. Secondly, the 2D peak transitions from a symmetric Lorentzian peak in SLG to an asymmetric peak for thicker flakes of two layers or more (fig 3.8.b). In BLG, the 2D peak can be modeled by four Lorentzian peaks (3.8.a).

Twist angle resolution

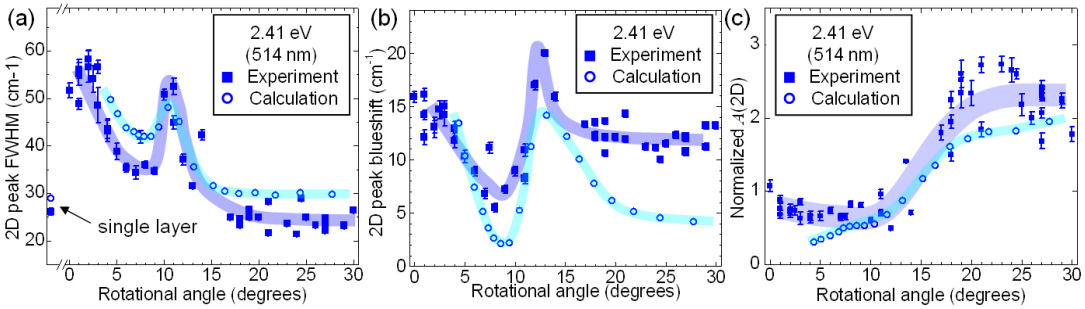


Figure 3.9: Twist angle dependence of the Raman spectrum. (a) FWHM of the 2D peak as a function of the twist angle. This was calculated from a single Lorentzian fit of the 2D peaks. (b) Blueshift of the center of the 2D peak w.r.t. the position of the 2D peak in SLG. (c) Integral intensity of the 2D peak normalized to the integral intensity of the 2D peak in SLG. All measurements are made using a 514 nm laser. Figure from [64].

Raman spectroscopy not only allows to quickly identify the thickness of a graphene flake, but it is also able to tell the presence of a twist angle through the top h-BN of a stack. The 2D peak is sensitive to small misalignment in all possible ways as shown in figure 3.9. The 2D peak's width and position decrease quickly with increasing angles for small angles. In the figure, the width of the peak is characterized by fitting a single Lorentzian peak around the 2D peak and measuring the fit's full width at half maximum (FWHM). The position of the peak is measured relative to the position of the 2D peak of SLG. Finally, the 2D peak's integrated area also varies with the twist angle, but the variations are small at small twist angles. These twist angle dependencies in the Raman spectrum are most pronounced when measured with a red laser (633 nm) [64]. However, given the available expertise, all spectra measurements in this master thesis are made with a 514 nm laser. It is interesting to note that these features (except for the position) approach the features of (2 sheets of) SLG graphene for large twist angles, indicating almost no interaction between the layers at large twist angles.

Carozo et al. (2011) [65] developed a completely different method for the resolution of the twist angle in the Raman spectrum. It is based on the emergence of a new peak (called the R' peak) whose position depends on the twist angle as shown in figure 3.10. However, the position of this new peak at the magic angle is ~ 1595 cm^{-1} and is therefore potentially hidden by the G peak. Nevertheless, this method might be very useful for the identification of larger twist angle. The region in which the R' peak might be hidden by the G peak has been set between 1570

and 1598 cm^{-1}. This choice is because the G peak has a FWHM of $\sim 6 - 16$ cm^{-1}. Because the R' peak could be small compared to the G peak, a safety margin has been (arbitrarily) set to 10 cm^{-1} on each side. Furthermore, the G peak's position may fluctuate between 1580 and 1588 cm^{-1} [59]. This yields the chosen "danger" region.

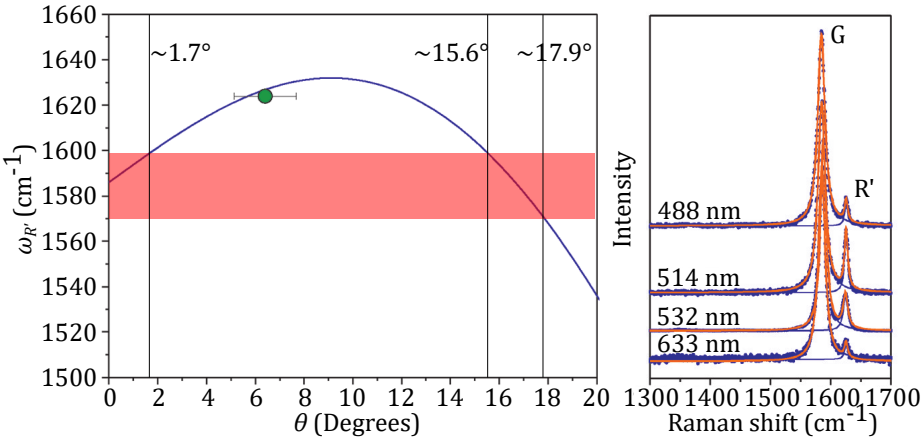


Figure 3.10: Left: theoretical position of the R' peak as function of the twist angle. The shaded region represents all the positions where the R' peak might be hidden by the G peak. Right: measurements of the R' peak on a $6 \pm 2°$ tBLG sample. The green dot and the error bar on the left panel show the position of the measured R' peak. Adapted from [65].

3.3.3 h-BN

h-BN also has a Raman signature in the 1200 to 2900 cm^{-1} range. Only one sharp peak is visible at $\sim$ 1360 cm^{-1}. This peak hence coincides with a potential D peak in graphene, possibly hiding it in the Raman spectrum of a stack. Therefore, it becomes unfortunately hard to know with Raman spectroscopy if a defect has been brought to the graphene during the stacking process. Since the h-BN is well visible under optical microscopy and its thickness doesn't really matter for this thesis, the Raman signature of h-BN won't be further discussed. An example of the h-BN peak in the Raman spectrum is shown in figure C.5 of appendix C.

3.4 Thermal annealing

It is known that, at high temperatures, tBLG tends to realign into Bernal stacked BLG. This phenomenon is driven by a strong dependence of the Van der Waals

energy with the twist angle. Furthermore, as briefly mentioned in section 2.3.3, friction between twisted graphene layers is very small, even leading to superlubricity in some cases [46]. These two properties (high Van der Waals potential gradient and low friction) are the origins of thermal annealing of the twist angle in tBLG. In fact, what seems to prevent the twist angle annealing at low temperature is the pinning effect due to chemical adsorbents between the layers. Annealing to Bernal stacked BLG of tBLG samples, twisted by an angle of $\sim 5°$, has been observed after 12 h at 200°C [66]. Similar studies on angle annealing between graphene and h-BN indicate a constant annealing rate ($d\theta/dt$) that heavily depends on temperature and flake size [67].

A precise temperature threshold not to cross in order to prevent thermal annealing of the samples is however hard to determine given the small number of quantitative studies of this phenomenon. It is nevertheless possible to look at the thresholds set by other groups who have achieved results with tBLG samples. During their fabrication process, Cao et al. (2018) [5] have heated their stack up to 160°C for a few minutes without consequences on their measurements. Other papers [32, 68] mention in their fabrication process the self set limit of 180°C. The same temperature limit of 180°C is hence imposed for the process in this master thesis.

3.5 Dry transfer

Transfer methods of graphene are required to move the graphene flake from one substrate to another. Two families of transfer exist: wet and dry transfer methods. Wet transfer methods involve the contact between the graphene layer and a liquid at some point during the process [53]. During the contact between the liquid and the graphene, some contamination is possible which might result in undesired doping [69]. Dry transfer techniques make use of the strong Van der Waals interactions between h-BN and graphene to detach the graphene from its substrate. The graphene and h-BN are usually brought in contact using a polymer. Dry transfer methods yield higher charge carrier mobilities and are well suited to encapsulate graphene flakes in h-BN. Therefore, a dry transfer technique is used in this master thesis.
Different variants of dry transfer techniques exist. Differences may reside in the chosen polymers, whether graphene or h-BN are directly exfoliated on a polymer film or whether the polymer is also used to pick them up, ... The samples presented in this master thesis were made using a technique similar to the ones used in ref [70] and [71], with a few minor adaptations for practical reasons. The technique

for the creation of a precisely controlled twist angle is adapted from [72].

3.5.1 Tools

In order to make the desired heterostructures, the different flakes of graphene and h-BN need to be stacked onto each other. A series of tools are needed for this action. The first tool needed is one to pick up the flakes from the wafers they are on. This tool is made using a glass microscope slide and hence called a "transfer slide". The second tool allows the different flakes to be precisely aligned onto each other in order to stack them. This will be a complex system called the "transfer table", composed of several precisely moving parts, from which the movements are controlled by micrometre screws. They will be detailed in this section.

Transfer slides

A schematic representation of the procedure to make a glass slide is shown in figure 3.11. The idea to pick up the flakes is to use a transparent tool, with a sticky part at the bottom that can be used under an optical microscope. Polypropylene carbonate (PPC) is a polymer with high adhesion on h-BN flakes [72]. Furthermore, it has the advantage of having a glass transition temperature slightly above room temperature of $\sim 40°C$ [73]. This makes it possible for PPC to cover the desired flake smoothly by flowing on it when brought around 40°C and then maximize its adhesion with the flake when cooled down. Finally, the fact that graphene adheres better to SiO_2 than to PPC [71] but worse than to h-BN will be extremely useful for the selective picking of a part of a graphene flake (see later).
The PPC used for the pick-up presents itself in the form of a thin film. In order to precisely carry this film onto the wafer and under an optical microscope, it is important that it is carried on a transparent and rigid structure. The rigidity is ensured by dropping the film on a glass microscope slide. Then, it is necessary to have a small contact area between the PPC and the wafer for at least three reasons. First because there might be other interesting flakes on the same wafer and we would not want to waste them by accidentally picking them up. Secondly, the pressure on the flake needs to be applied precisely for the contact between flake and PPC to be as smooth as possible. Thirdly, once the h-BN (with or without graphene) is on the PPC, it loses its color (as it originated from interference inside the SiO_2) and is much harder to see under the microscope. Therefore, having only a small region to look for the stack saves a lot of time. This smaller area is formed by creating a bump on the glass slide where the PPC will be put on. This bump is made from a small block of polydimethylsiloxane (PDMS) (a type of silicone) dropped on the glass slide (figure 3.11.1) and held in place with some very transparent tape (e.g. Scotch Crystal Tape)(figure 3.11.2). The PDMS needs to be

very uniform and flat. PDMS has several advantages as it is optically very clear and soft. This softness makes a good contact with the wafer possible.
Eventually, the PPC film needs to be put on the bump created by the PDMS on the glass slide and also needs to be very flat. In order to ensure that, the PPC is dissolved in a solvent such as anisole (e.g. 15% PPC, 85% anisole). Then, it is spin-coated on a roughly 1 cm × 1 cm Si/SiO_2 wafer (figure 3.11.3) at e.g. 2000 RPM. The wafer is heated up to about 110°C in order to evaporate the anisole, leaving a thin PPC film. A hole (smaller than the PPC film) is then punched in a piece of tape, which is then used to pick up the PPC film (figure 3.11.4). It is useful to scratch a little corner of the film while on the wafer in order to hold the wafer in place without holding back the film. The tape with the film is then put on the slide, with the PPC on the bump (figure 3.11.5). Finally, the slide is heated up to roughly 110°C[2] (far higher than PPC's glass transition temperature) so the PPC can flatten out, leaving a very smooth surface.

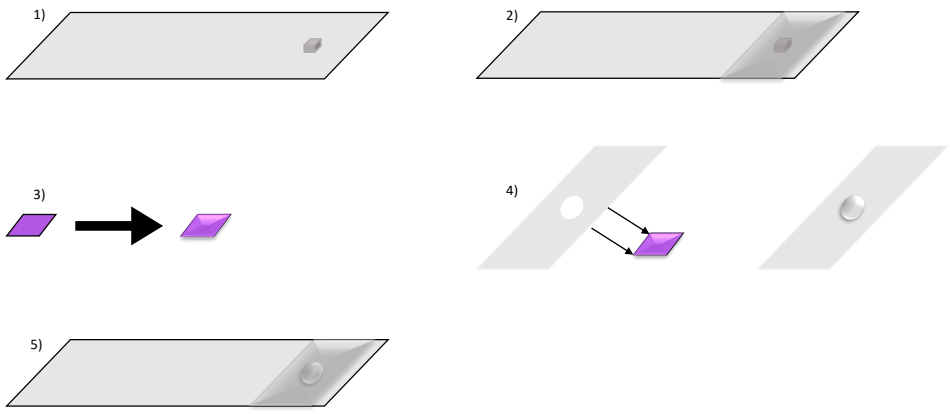


Figure 3.11: Scheme of a transfer slide.

Transfer table

As mentioned before, the transfer table is required only to align the flakes precisely before stacking them. However, given the way chosen to pick up the flakes, it is also necessary that the table includes a heating and cooling system. The transfer table is shown in figure 3.12. The table consists of two independent parts: one to move around the wafer and one to move the glass slide.

The first part (on the left of figure 3.12) needs to hold the wafer in place and be allowed to move around. It is important that the wafer doesn't move when

[2]This temperature is used for practical reasons as it allows to use the same heating equipment as the one used for the evaporation of the anisole.

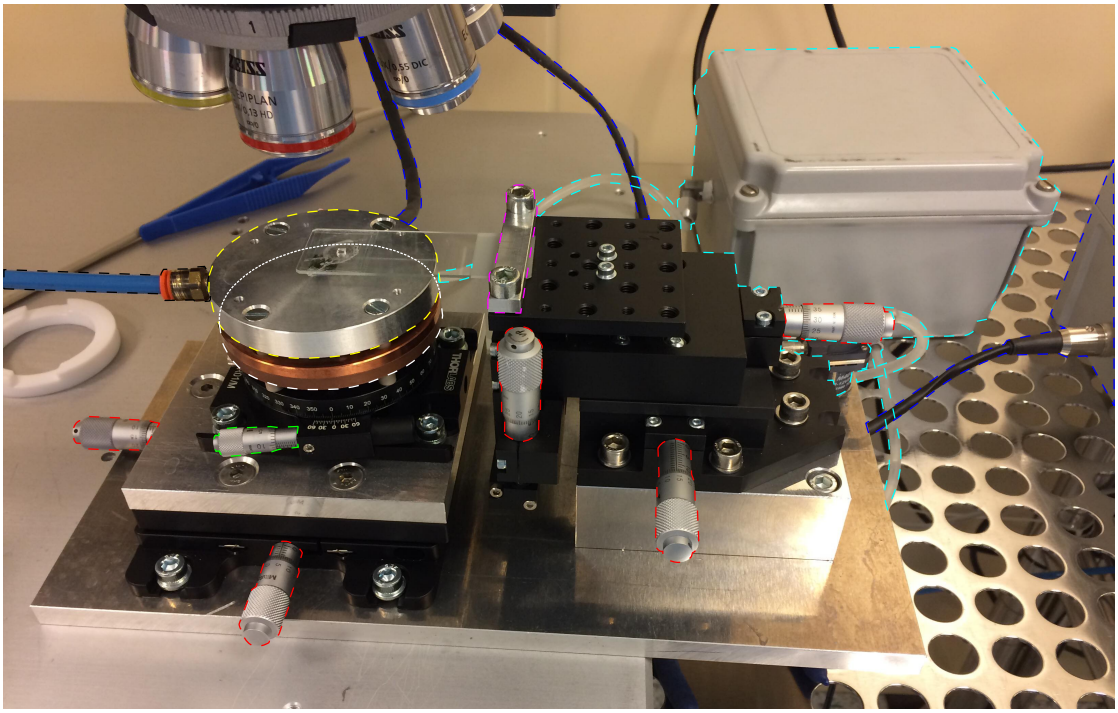


Figure 3.12: Picture of the transfer table with a few key elements highlighted. Yellow is the aluminum stage holding the wafer. White is the copper disc beneath the aluminum stage. In between the aluminum stage and the copper disc is the (hidden) Peltier cooler/heater. Magenta is the slide holding setup on the slide holding table. Red are the micrometre screws to move both the wafer holding table and the slide holding table in the x- and y- direction. The slide holding table can also be moved in the z-direction using the vertical screw. Green is the micrometre screw controlling the rotation of the wafer holding stage. A vernier-like scale is available for the control of the angle. Blue are the electrical connections to the PID controller for the temperature. Cyan are the pump, pipes and reservoir of the water cooling system. Black is the pipe from the vacuum pump.

a flake is picked up, especially for the control of the twist angle. Therefore, a vacuum pump pumps the air from a little hole in the center of the stage holding the wafer. The wafer can then be steadily held in place as it is sucked against the stage, hence increasing the friction. The stage holding the wafer can move in the x- and y-direction and is able to rotate. These motions are controlled with micrometre screws.
The second part of the table is a stage designed to move the transfer slide in the x-, y- and z-direction with three micrometre screws. The transfer slide is attached

on this stage, with the PPC pointing downwards, with a metallic bar pressing the slide on the stage with screws.
As mentioned, the transfer table is also equipped with a heating/cooling equipment. This equipment is installed on the wafer holding stage. A piece of copper is held as close as possible to room temperature thanks to a water cooling pipe twining within the piece of copper and connected to a water reservoir. The water circulates though the pipes thanks to a small pump. Copper has been chosen because of its high thermal conductivity and density, making it a great heat reservoir. On the piece of copper, there is a Peltier heater/cooler pasted with thermal grease to the copper. On top of that there is an aluminum stage, pasted on the Peltier heater/cooler also with thermal grease. The aluminum piece holds the wafer. Aluminum is the material chosen for its low density and relatively high thermal conductivity. The low density ensures that only a little amount of heat is required to reach a given temperature. The high thermal conductivity is needed to carry the heat to the wafer and to the PPC after that. The heating/cooling is performed with a Peltier device because of its small size, easiness to control electronically and lack of moving parts. However, such a device only imposes a temperature difference and no absolute temperature. This justifies the entire heat absorbing setup with the copper and water cooling system. Finally, a PID controller regulates the voltage on the Peltier device, taking into account the information from the temperature sensor included inside the aluminum.

3.5.2 Transfer

In order to obtain the desired stack one will first have to pick up an h-BN flake, then align it on the two graphene layers, correctly oriented and finally on the last h-BN flake. The entire stack is then dropped on a marked wafer for the lithography (see later). The first thing to do is to identify the best h-BN flake for the desired stack. As mentioned in the section about exfoliation, this means a perfectly flat flake of the right size. The ideal geometry of this first flake (which will eventually end up being the top layer of the stack) is roughly the shape and size of the graphene flakes. This is for two reasons. First, we don't want to take anything else than the needed graphene flakes which are not always properly isolated. Second, once the stack is made, the graphene flakes are no longer visible and it is much easier to perform a lithography when the position of the graphene is precisely known. This position is easier to identify on a small flake.

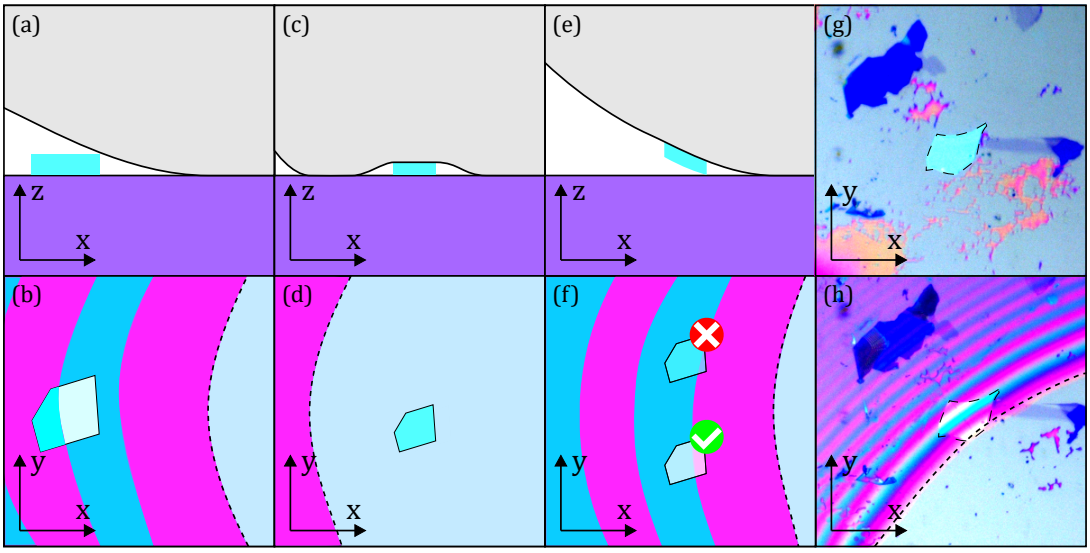


Figure 3.13: Picking up technique for h-BN flakes. (a) and (b) show the point at which the lowering must stop and heating must start. (c) and (d) show when the heating can stop and cooling start. (e) and (f) show the actual pick-up. (f) emphasizes the color change, seen in successful pick-ups. (g) and (h) show an example with real colors. In all panels, the short dashed line represent the contact front.

The pick-up method (illustrated in figure 3.13) has been briefly described when explaining the choice of PPC as adhesion enhancing material, but will be discussed in more details in this paragraph. The first thing to do is to identify a clean region on the PPC to pick up the flakes. It can indeed happen that some dust lands on the transfer slide and those could damage the h-BN flake and the final stack. The clean region is identified by coinciding the focal plane of the optical microscope with the PPC layer. The clean region must be aligned with the micromanipulator above the h-BN flake. Alignment can be checked by drawing the shape of the flake on the screen of the computer displaying the microscope image and subsequently changing the focus of the microscope on the plane of the PPC. The transfer slide is lowered vertically until the PPC is in contact with the wafer. The contact is visible by a change in color as seen in figure 3.13. The region of contact between the PPC and the wafer is bordered by a contact front (dashed line in fig 3.13). The transfer slide must ideally be lowered until the point where the contact front is just about to reach the flake (fig 3.13.a and 3.13.b). Then, lowering must stop and heating to $\sim 40°C$ can start. The contact front will expand during heating, eventually crossing the targeted flake. This is to make sure that the PPC flows all over the flake in a smooth way. The temperature must be held at 40°C for a few minutes (until the contact front no longer expands) in order to let the PPC

thermalize and make contact with the flake. Once the contact front has stopped expanding (fig 3.13.c and 3.13.d), the voltage on the Peltier heater may be flipped to set it in cooling mode. The cooling goes on until reaching a low temperature, far lower than the glass transition temperature of PPC (40°C), but above 0°C as going below 0°C would make water droplets condense on the wafer and the stack (cfr. fig C.1 in appendix C). This effect is not desired again because it could damage the flakes and stack. Therefore, the target temperature for cooling is set around 5°C. It can happen that, during cooling, the contact front shrinks. This is no problem so long as the contact front doesn't reach the flake as, from experience, this usually leads to a failure of the pick-up attempt. If that happens, the transfer slide can be slightly lowered to maintain the contact front distant from the targeted flake. When 5°C is reached, the voltage on the Peltier device is switched off, slowly letting the setup thermalize to the ambient temperature. Then, the transfer slide is very slowly lifted from the wafer until the entire contact front has crossed the flake, after which the transfer slide can be lifted faster. In order to maximize the rate of success, this has to be done before the setup has reached a temperature above $12 - 13$°C as has been observed from experience. If the flake has lost its color and become white, it has been picked up by the transfer slide and the transfer is a success (fig 3.13.e and 3.13.f). Otherwise, the procedure can be restarted. Before any pick-up attempt, the transfer slide can be heated up to about $90 - 110$°C in order to flatten out the PPC that could have been deformed by previous transfers. However, this cannot be done between the transfer of the two graphene flakes as the knowledge of the relative crystalline orientation would then be lost. The reason for that will be explained in the next section about the transfer angle.
Once part of the stack is formed and on the transfer slide, it has to be precisely aligned with the next layer to be transferred. This is done again by drawing the flake on the wafer and/or the stack on the PPC on the screen of the computer and aligning both by changing the focus to the other plane (wafer or PPC). When the transfer slide is lowered, it is important to check that the alignment has not changed. This is for two reasons. First, because slight movements of the hand during manipulation of the "lowering" screw may lead to a slight shift of the horizontal position of the transfer slide. Second, because the glass of the slide and the PDMS have different refractive indices than air. The observed position of the flake might differ slightly when lowering the transfer slide. When picking up graphene flakes, they become more and more blurry and harder to see when the slide goes down. It can then be helpful to use surrounding flakes on the wafer as markers to check that the alignment is still correct.

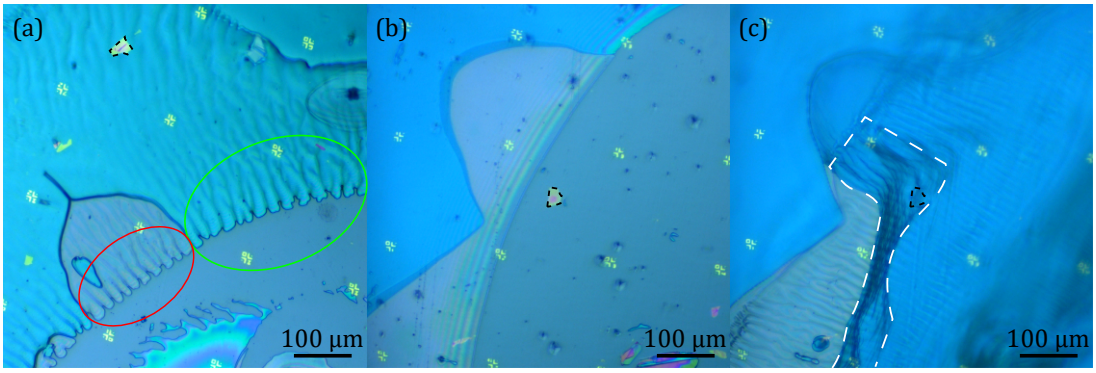


Figure 3.14: Drop-down of a flake. (a) Successful drop-down. The normal contact front (green) and a bubble in formation (red) are indicated. (b) Stack before the contact front passes. A large bubble is visible in the contact front. (c) Same stack as in (b), but after crossing of the contact front. Risks presented by a bubble are illustrated, the white dashed line highlights the wrinkled part of the PPC. In all figures, the black dashed line indicates the flake dropped.

This entire procedure is the same to pick up both the h-BN and graphene flakes. As mentioned, the top (first transferred) h-BN flake needs to be roughly the size of the graphene flakes. The bottom h-BN flake, however, can be any size as long as it contains a large enough region to lay the entire stack on.
When the stack is completed, it needs to be dropped on another, clean and marked, Si/SiO_2 wafer for the lithography (the reason for the marks will become clear in the lithography section). This is the most delicate step, many things can go wrong. The first thing to do is to align the stack (on the slide) roughly in the middle of the wafer. Then, the slide is lowered until it comes in contact with the wafer in exactly the same way as it was done for pick-up. The difference for drop-down is that the temperature is then raised to $\sim 80-90°C$ where the PPC really becomes a (viscous) fluid. Then, the slide can be very slowly lifted until the contact front crosses the stack. As can be seen in figure 3.14, the contact front looks very different at such temperatures. When the contact front has crossed the stack, the latter is dropped and the slide can be lifted up a little bit faster. If everything went well, the PPC has been dropped down as well and still covers the flake.
An alternative is to cool back the PPC after the contact front has passed the stack and before lifting the slide. This alternative is more complicated, but when successful presents two advantages. First, it almost doesn't leave any PPC behind on the slide (unlike the first method), making the cleaning of the stack easier. Second, if the PPC is not too damaged, the slide can be reused for another transfer after having heated it back to $90-110°C$ to flatten the PPC's surface.
Two things can go wrong during the drop-down. One is that during the first (slow)

lifting of the transfer slide a bubble appears in which the PPC wrinkles heavily. These wrinkles in the PPC could break the stack due to increased stresses (see fig 3.14.c). If a bubble starts to form the slide needs to be lowered again, cooled to roughly 40°C, lifted up slightly to put the contact front closer to the stack and then heated up again. The other thing that can go wrong is during the second (faster) lifting of the slide. If the stack is not well dropped on the wafer after the contact front has passed it, it could be picked up again by the PPC and get lost in wrinkles forming in the hot PPC. If this starts to happen, the slide must be lowered again and the entire procedure restarted.
When the stack has been successfully dropped on a marked wafer it has to be cleaned from all the remaining PPC and glue from the exfoliation. There are two ways of doing that: physically or chemically. The physical method is to heat up the stack in vacuum to high temperatures ~ 300°C for one or two hours. This will make the polymers decompose and subsequently evaporate (cfr section on stack flips). The chemical method consists in putting the wafer with the stack for ~ 10 minutes in a powerful organic solvent like chloroform [74]. The chemical method is faster, but consists in manipulating dangerous chemicals (which is always better to avoid). Furthermore, there is a small chance that, if a lot of PPC has been deposited on the wafer and the stack hasn't been dropped properly on the wafer, the stack vanishes in the chloroform with the PPC. The physical method is safer for the user and leads to less losses of stacks. However, at temperatures as high as ~ 300°C risks of thermal annealing of the twist angle are too high. This means that for the production of twisted bilayer graphene, the physical method cannot be used and all the stacks mentioned in this thesis were cleaned using chloroform.
The reader might have noticed that a small magnification ($\times 10$) has been used for all steps of transfer under the optical microscope. This is because, with the material used, the image becomes far too blurry to work with at higher magnifications. The source of this problem likely originates from the poor quality of the PDMS used.

3.5.3 Twist angle

The biggest issue with producing twisted bilayer graphene is to precisely control the twist angle. Indeed, it is hard to know in what orientation the lattice of a graphene flake is oriented. The solution to this problem comes with the fact that mechanically exfoliated graphene flakes is monocrystalline [51]. In order to select the rotation angle precisely, a large flake could just be split in two sub flakes with originally the same crystalline orientation. Then, the flakes should simply be superimposed, while twisting one relative to the other.
As mentioned before, graphene adheres less to PPC than to SiO_2, hence bare PPC never manages to pick up graphene flakes. However, the Van der Waals interactions between h-BN and graphene are much stronger than those between graphene and

SiO_2 [75]. The solution becomes to align the h-BN flake with only some part (± half) of the graphene flake (fig 3.15.d). The part of the graphene flake covered by the h-BN flake is then picked up, while the part covered by the PPC tend to stay in place on the SiO_2 wafer. This is possible because graphene tend to easily tear apart in such situations as observed experimentally and illustrated in figure 3.15.

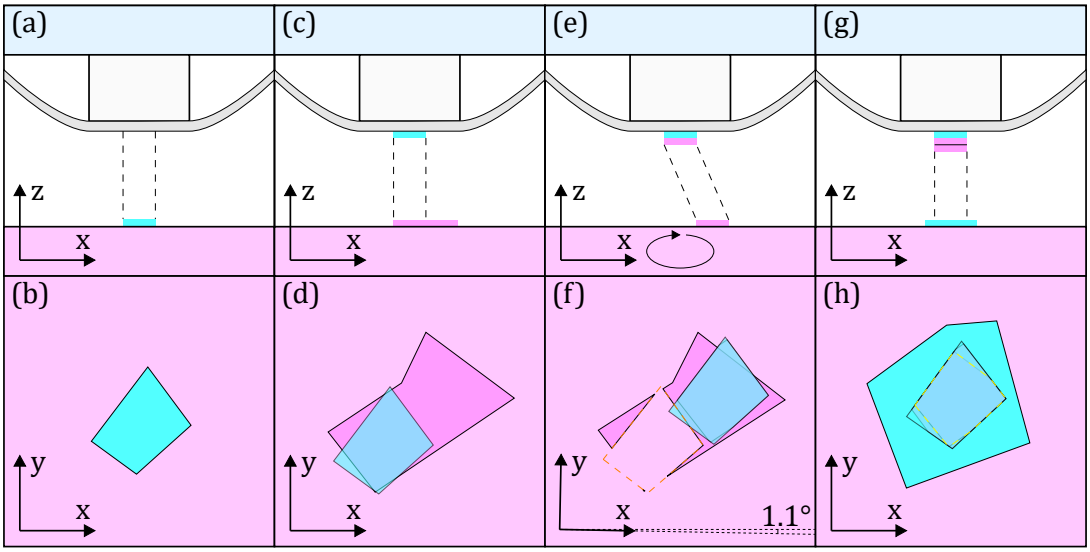


Figure 3.15: Stacking different flakes.

The twist angle is set by turning the rotation stage from the micromanipulator with the appropriate angle. On screen measurements with back ground elements may help determine and adjust the rotated angle (cfr. figure C.2 in appendix C). However, the exact angle between the layers in the sample may vary a little from the angle that was selected, due to three likely causes [32]:

- The top graphene may rotate onto the top h-BN as there is very little friction between those layers.
- During pick-up, the bottom graphene has the tendency to "jump" off the Si/SiO_2 wafer directly onto the stack, possibly inducing a slight angle.
- Graphene may strain during stacking, effectively changing the area of the Moiré unit cell for a given twist angle, hence changing the electronic properties.

3.5.4 Stack flips

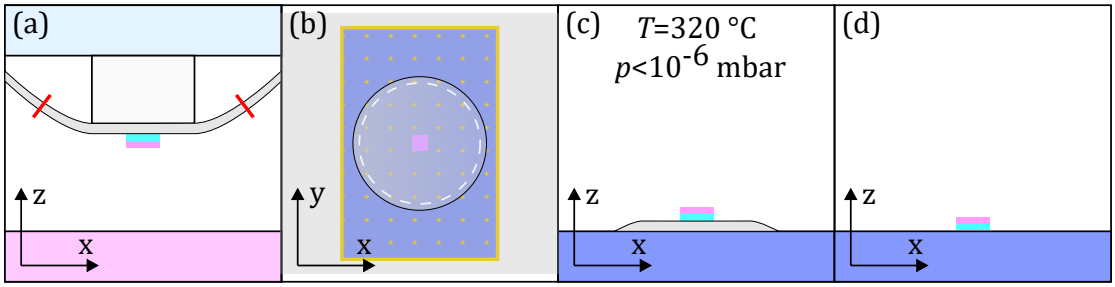


Figure 3.16: Stack flip procedure. (a) Targeted cuts of the PPC to be flipped and dropped on a marked wafer. (b) Light grey is the piece of crystal tape holding the PPC, stuck on a marked sample. The grey circle with black edge in the middle represents the PPC with, at its center, the stack with the graphene on top. The white dashed line is the targeted cut of the PPC. (c) Marked wafer (blue) with the PPC (grey) and the stack on top of it. This is put inside an oven under vacuum. (d) After heat treatment, the PPC is gone and the stack fell down on the wafer.

For any other device than twisted heterostructures, another method exists that makes the contacting much easier, the so-called "stack flip" method. Figure 3.16 shows a schematic development of the method. In order to maintain an easy access to the graphene, the targeted sample in this method is one with the graphene on top (fig 3.16.d). This is done by peeling off the transfer slide, the tape holding the PPC (tape from fig 3.11.d). The tape is then stuck on a clean, marked wafer with the PPC completely on the wafer (fig 3.16.d). The sticky part of the tape must be down in order to have the stack on top of the PPC. Next, the PPC is cut from the tape on the wafer (white dashed line in fig 3.16.b). Finally, the wafer with the PPC on it is put in an oven under vacuum ($p < 10^{-6}$ mbar) at 320°C for 1 to 2 h. At temperatures between $\sim$ 220 and $\sim$ 300°C the PPC decomposes into volatile side products [76] which are then eliminated by evaporation under vacuum. Because of these high temperatures at stake in this process, stack flips are not applicable to tBLGs on PPC. However, if a polymer were found to be suited for dry pick-up of h-BN[3] and with low decomposition temperature ($<$ 180°C), this could be an interesting alternative. Other polymers used in the literature for dry transfer of graphene on h-BN are polycarbonate (PC) and poly(methyl methacrylate) (PMMA). However, none of them show a decomposition temperature below 180°C (but respectively $\sim$ 500 and $\sim$ 600°C [77, 78]).

[3]and not graphene as the tearing of graphene to create the twist angle is possible only because of the selectivity of PPC pick-up.

3.6 Lithography

The stack being completed, it must subsequently be put into the right shape and contacted before any measurement can be performed. This is done using a lithography technique, more specifically an electron beam lithography. The reasons behind the choice of this technique are multiple. Firstly, given the size of the flakes and the desired design, a precision of a few hundreds of nanometres is required, this can really be achieved only by e-beam lithography or X-ray lithography. Secondly, every stack having its unique geometry, it is much faster not to use a process requiring the production of a mask. Eventually, the main drawback of e-beam lithography is usually its exposure speed, but with the small size of exposed areas, this is not a problem as the exposure only lasts up to a few minutes.

3.6.1 Working principle

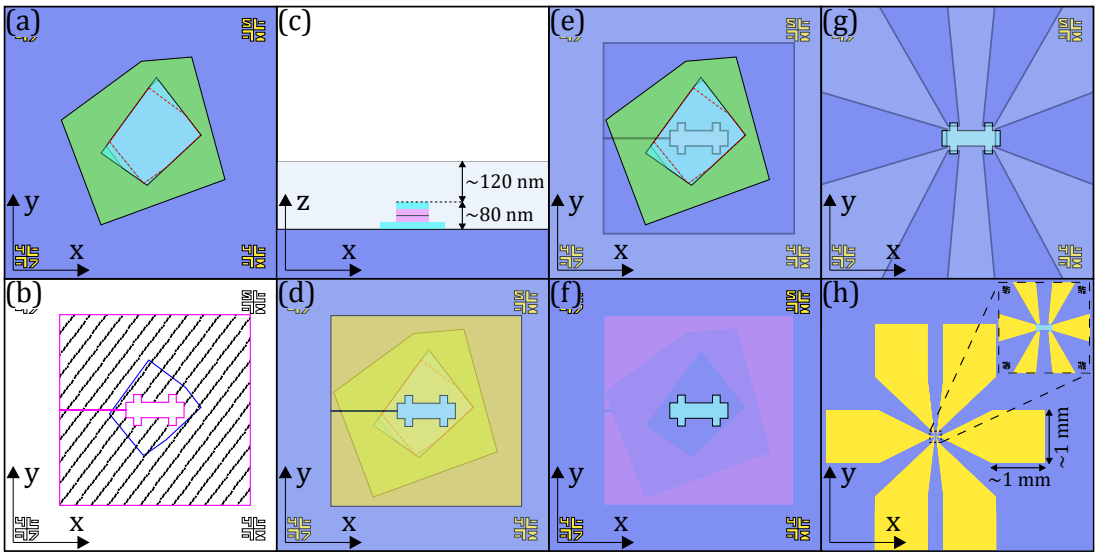


Figure 3.17: Schematic representation of the lithography procedure. (a) Imaging and registering the position of the stack with respect to marks using a SEM. The red dashed line shows the area above the tBLG. (b) Lithography lay-out drawing on the recorded position. (c) Spin coating with PMMA. (d) Exposure of the lay-out (yellow area is exposed). (e) Development and etching. (f) Lift-off of the PMMA resist, the coloured contours of the flakes are their "shadows" in the etched SiO_2. (g) and (h) illustrate the contacting process. (g) Lithography of the grooves. (h) Metalization and lift-off.

Figure 3.17 shows a schematic representation of the process of lithography. The main idea of this technique is to give to the stack the desired Hall bar shape by etching away the surrounding parts of the stack. This is possible by protecting the area of the desired Hall bar with a polymer mask, before etching the unprotected regions of the stack. To do that, the stack is covered by poly(methyl methacrylate) (PMMA), with a very narrow chain length distribution, centered around 950000. When exposed to an electron beam, the chains are broken into smaller bits, increasing their solubility in a solvent like methyl isobutyl ketone (MIBK). Once the flake is covered by PMMA, a region surrounding the desired area is exposed by the electron beam of a scanning electron microscope (SEM). The exposed region is then weakened by the electron beam, hence becomes soluble in MIBK. The exposed region is thus dissolved in MIBK and and one can then use an etching technique to remove the part of the flake or stack left uncovered by the PMMA. This entire process leaves only the protected area behind, with the desired shape. The last step is to dissolve the remaining PMMA.

3.6.2 Preparation

Two things need to be done before exposing the sample in the SEM. The first thing is to precisely locate the stack on the wafer. Secondly, the wafer needs to be covered by the PMMA resist of appropriate thickness.
The first step is performed by imaging the flake with the same SEM that will serve for the exposure. The reason for that is that the position of the stack can vary a little bit between the different imaging techniques. The position of the stack and its shape are, using the SEM image, precisely recorded with respect to some gold marks printed on the wafer beforehand. Each mark is 20 µm wide and the different marks are separated by 200 µm. With this recorded position, a negative of the desired Hall bar shape is drawn on a computer. In practice, this is done by drawing a polygon closing in on itself, leaving a hole with the shape of the Hall bar in its center.

The thickness of a stack is typically around 80 nm. The etching process also etches PMMA of, depending on the process, around 50 to 100 nm. For this reason, the initial thickness of the PMMA resist covering the stack should be at least 200 nm. Such a thickness can easily be obtained by a spin-coating method. In such a method, the combination viscosity ($\sim$ concentration)-spinning speed determines the thickness of the resist. Calibrations with PMMA dissolved in anisole yield a theoretical resist thickness of 219 nm for a 4 % vol. PMMA solution at 4000 RPM. This is of the desired order of magnitude and these parameters are hence the ones chosen for this process. After being spin-coated, the anisole must be evaporated in order to leave only a PMMA layer behind. This is important for two reasons. First, a 4 % solution of PMMA in anisole has a relatively low viscosity and the

PMMA flowing freely on the surface of the wafer after exposure would dramatically decrease the precision of the exposure. Secondly, the e-beam exposure is a process happening under vacuum. If anisole is still present in the layer when put inside the SEM, this would slow down the vacuum pumping step of the SEM chamber as anisole would continuously evaporate. The conventional method to evaporate the anisole is to leave the sample for 15 min inside an oven at 150°C. However, heating to temperatures as high as 150°C might lead to some uncertainties in the twist angle as the exact mechanisms of thermal annealing are still poorly quantified. An alternative method is to put the sample under vacuum for 24h and let the anisole evaporate that way. Nevertheless, in the case of this master thesis, most of the samples were put inside the oven as this process is much less time-consuming. When both of these steps are done, the sample is ready for exposure.

3.6.3 Exposure and development

After the PMMA spin-coating, the sample can be put inside the SEM and be ready for exposure. The stack cannot be imaged this time as imaging would expose all of the PMMA covering the stack, hence ruining the lithography. Therefore, the position of the stack can be determined by very precisely positioning the previously mentioned gold marks. Since the stack's position relative to the marks is well known, the exposure can be precisely performed without ever having to image the stack again. The required exposure dose for PMMA is $\sim 300\ \mu C/cm^2$ at 30 kV acceleration potential and depends almost linearly on this voltage.
Once the exposure is done, the sample can be developed, i.e. the exposed PMMA can be removed by dissolving it in MIBK. This is done by putting the sample in MIBK for 1 minute and 30 seconds, slowly shaking it inside the solution. This is enough to dissolve any exposed PMMA, but not yet enough to dissolve unexposed PMMA. After that, the sample is put, again for 1 minute and 30 seconds, in isopropanol to wash away all the remaining MIBK. The duration of this last step is not critical but the step must nevertheless absolutely be performed as leaving the sample in the MIBK for a little while longer might dissolved the unexposed PMMA, ruining the lithography. The sample can be dried with nitrogen and then observed using optical microscopy. If the exposure is a success, the process continues, otherwise all the PMMA can be washed away with acetone and the process can be restarted until it succeeds.

3.6.4 Etching

Given the available equipment, two etching methods commonly used in the literature are possible. The first possibility is a Reactive Ion Etching (RIE) process using a SF_6/Ar mix. The second possibility, which seems to be the most common in

the literature, is an Inductive Coupled Plasma - Reactive Ion Etching (ICP-RIE) process using a mixture of CHF_3/O_2. The main difficulty resides in the fact that the tBLG sample is completely encapsulated in h-BN due to the transfer process. Furthermore, there is no process known for selectively etching the h-BN and not the graphene. This involves the necessity to contact the stack through one-dimensional line contacts. However, because of graphene's lack of chemical bonding sites on its surface, the contact resistance of surface contact is much larger than for side contacts. Hence, line contacts outperform surface contacts for graphene as counter-intuitive as it may seem [70].

RIE SF_6/Ar process

Reactive ion etching is a technique that uses a plasma to etch a material. The wafer, containing the material to be etched is inserted in a vacuum chamber between two electrodes. A gas is injected at a certain flow rate. This gas becomes plasma and is accelerated between the electrodes by a radio-frequency (RF) electric field. The etching can happen by a physical or chemical mechanism or a combination of both. Indeed, the acceleration field leads to collisions between the charged particles of the plasma and the material, leading to a physical etching effect. Furthermore, ionized molecules also tend to be extremely reactive and can thus also have an etching effect by reacting with the material exposed. The composition of the plasma, pressure of operation, RF power supply as well as the time of exposure form together what is known as the recipe of the etching process. [79]
In the case of the SF_6/Ar RIE process for h-BN, the reference recipe has been found in the literature [80]. The gases injected and to be ionized are SF_6 and Ar in proportions $1:1$. The total flow of the mixture is 20 standard cubic centimetre per minute (sccm)[4]. The operation pressure and RF power are respectively 100 mTorr and 100 W. The time of etching mentioned is 20 s. It is worth noticing that the actual flow matters very little as the quantity of plasma in the chamber of each gas is mainly determined by the operation pressure and relative quantity of each gas. The only impact of a larger flow is the faster renewal of the plasma in the chamber, replacing reacted side-products with "fresh" plasma.
As shown in figure 3.18, this process is expected to etch at a more vertical angle [81]. This is because, with SF_6 the physical sputtering effect of RIE is dominant over the chemical sputtering effect.

ICP-RIE CHF_3/O_2 process

ICP-RIE is a variant of the RIE technique using a magnetic coil to condense the plasma at the center of the chamber. The denser plasma creates a more isotropic

[4]Volume flow in cm^3/min as it would be under standard conditions of pressure and temperature.

etching profile because the higher plasma density enhances the chemical sputtering process compared to the physical one.
The recipe for this process has been mentioned several times in the literature [70, 82]. The gas mixture is CHF_3/O_2 with respective flows of 40 sccm and 4 sccm. The RF power is 60 W. The expected etch rate of h-BN in this mixture is 30 nm/min. This method being slower than the previously mentioned process, a problem may appear as this plasma mixture also etches PMMA. It is important for the integrity of the stack that the protecting layer (PMMA) lasts longer than the etched h-BN. If not, the targeted Hall bar could be etched as well. Therefore, Wang et al. (2013) [70] suggest, on top of the PMMA layer, the addition of a hydrogen silsesquioxane (HSQ) layer of roughly 90 nm thick. HSQ resists are also used for electron beam lithography and do not change the process fundamentally. This process being much more isotropic, it is expected to etch the stack at a 45° angle. This is an advantage for the contact deposition, as inclined walls are more accessible for vertical metal deposition.

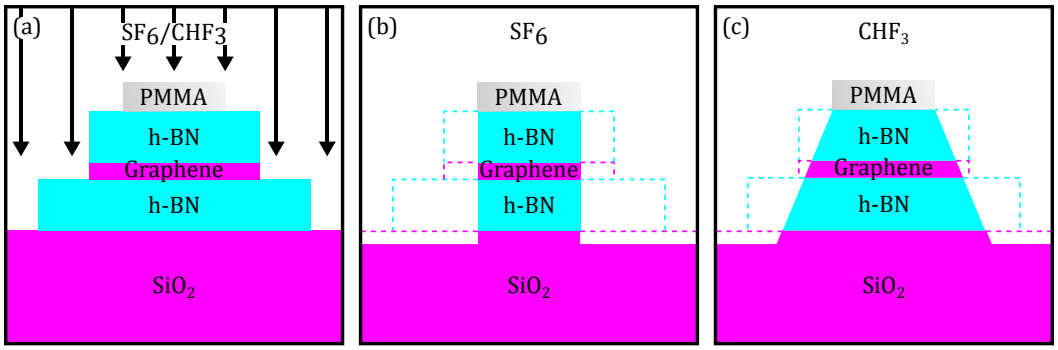


Figure 3.18: Different expected results for SF_6 etching vs CHF_3 etching. (a) Schematic representation of a RIE procedure. (b) Expected result with SF_6 etching. (c) Expected result with CHF_3 etching.

Tests

Every RIE equipment is different and therefore it is important to test the etching recipes before actually applying them on stacks. The SF_6/Ar in [80] and the CHF_3/O_2 in [70] recipes were respectively used on a RIE Oxford Plasmalab 80 and an Oxford ICP 80 systems. The system available in the WINFAB facility is an Oxford Plasmalab 100, different from the reference equipments, justifying the need for a test. Both recipes were tried on a large 3 inch wafer holding two smaller wafers: one coated with PMMA, the other holding exfoliated h-BN flakes (see figure 3.19). The thickness of the PMMA layer and SiO_2 layer were measured with an ellipsometer before and after the etching test. The ideal result is to observe

the disappearance of the h-BN flakes, while the SiO_2 and PMMA still have a "reasonable" thickness. By reasonable, it is meant a loss of thickness of less than $\sim$ 100 nm for PMMA and $\sim$ 50 nm for SiO_2. The reason is that a stack is typically 80 nm thick as the cyan h-BN flakes are typically 40 nm thick. Because the thickness of the PMMA layer for the lithography is roughly 200 nm, the PMMA supposedly tops the stack by a little more than 100 nm. Hence, 100 nm loss of the PMMA thickness is the maximum that can be tolerated before putting the integrity of the stack at risk. The SiO_2 should not be etched by more than $\sim$ 50 nm because this would mean a gap of $\sim$ 90 nm between the graphene and the top of the etched SiO_2 (40 nm from the thickness of the bottom h-BN and 50 nm etched from the SiO_2). This would mean that, in order to successfully contact the sample, a gold layer of $\sim$ 100 nm would have to be deposited. The lift-off in the contacting process (see later) would only work with a sufficient gap between the deposited metal and the PMMA layer (of $\sim$ 200 nm as well). Therefore, a loss of more than $\sim$ 50 nm in the SiO_2 layer would require a thicker metal layer deposition, hence putting at risk the lift-off process.

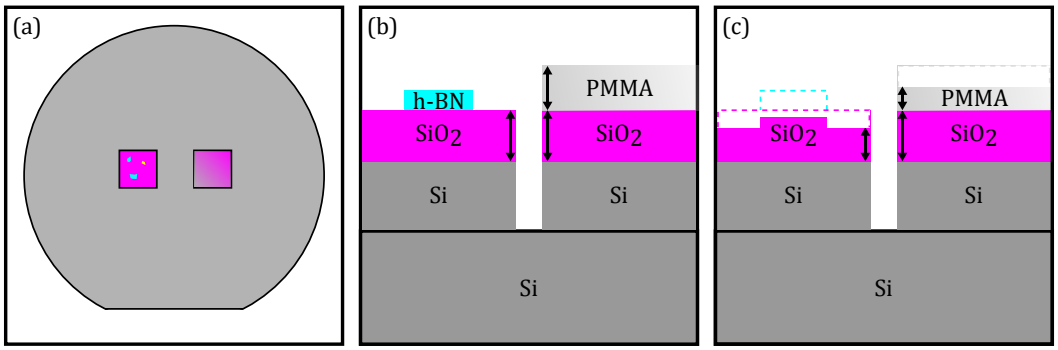


Figure 3.19: (a) 3" Si wafer with two smaller Si/SiO_2 wafers with respectively h-BN flakes and PMMA. (b) Ellipsometer measurements of the thicknesses of the SiO_2 and PMMA layers. (c) Checking that the h-BN is gone as well as measuring the change in thickness of the SiO_2 and PMMA.

3.7 Contacting

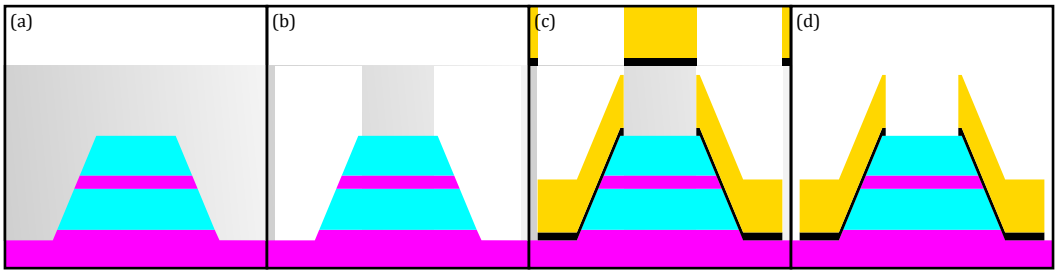


Figure 3.20: Scheme of the contacting procedure. (a) Coating of a PMMA resist on the wafer. (b) Exposure and development of the grooves. (c) Deposition of the gold with a thin underlayer of chromium for the adherence. (d) Dissolution of the PMMA and lift-off of the undesired gold layer.

The contacting procedure is very similar to the lithography process as shown in figure 3.17. The sample is again covered with a PMMA layer and put inside a SEM. Then, grooves are drawn from the contact points of the sample going outwards. This is done in 2-3 steps. A first exposure draws the thin grooves leaving contact points with the stack up to ~ 100 µm from the stack. This exposure is performed with low current as to increase precision. Then, a series of other exposures at higher currents enlarge the grooves until they reached a width of a few hundreds of µm. From there, large squares are exposed at the end of those grooves that will serve as contacting pads. The exposure current intensity is a trade-off between precision and exposure speed. In order to make sure that the different parts of each groove obtained by the different exposures are in contact with each other, a small overlap of a few microns is planned between the different exposures. After development, the grooves acquire their depth. The next step is to fill part of these grooves with gold on top of a thin layer of chromium (~ 5 nm). Chromium is used for adhesion with the substrate as it wets it well. The use of gold avoids oxidation problems on top of gold being a low resistance conductor. This is done in a process called metalization. In this process, a layer of 50 to 100 nm of gold is deposited by e-beam evaporation on the entire sample and hence in the grooves. After that, the PMMA is removed in acetone, taking with it the gold deposited outside the grooves.

Chapter 4

Fabrication results

In this section, results of the methods discussed in the previous chapter are discussed, along with an analysis of their quality.

4.1 Graphene flakes

The quality of the final device heavily depends on the choice of the graphene flake used for its fabrication. Graphene exfoliation and identification of the flakes is the most time-consuming step of the entire process. It is thus important to know what flakes can be expected in order to optimize this process. The minimal feasible size for the final, 6 contacts Hall bar can be set to approximately 3 µm × 5 µm. The misalignment during stacking and lithography can be up to ∼ 1 µm. Furthermore, in case of a rectangular flake, a maximum of 50% of the surface of the flake can effectively become the surface of the tBLG, as the flake is split in two. Therefore, the flake selected must at least have dimensions of 2 × 6 µm × 4 µm. This means a surface area of at least ∼ 50 μm^2 and a width of at least 4 µm. Size, however, is not the only important factor, the shape, surroundings and uniformity of the flake are too. Some shapes, such as triangles and curved shapes, do not allow a good overlap between the two halves of a flake. Triangles, for example, only allow for a maximum overlap of 33% of the area of the original flake. Isolated flakes are easier to pick up than flakes surrounded by thick graphite chunks, as these might be an obstacle to good contact between the h-BN and the graphene. Graphite must be avoided or removed to use the flake. In the first case, this is done by picking the graphene up a small margin away from the graphite, hence leaving some graphene unused. Removing the graphite is possible by picking it up like if it were graphene. This has been done (unwillingly) for the flake in figure 4.2, yielding the flake in figure 4.4.a. However, this might damage the graphene flake such as in the example. Finally, the flake's uniformity is important as well, as the quality of the graphene

has been the criterion for the choice of an exfoliation method.

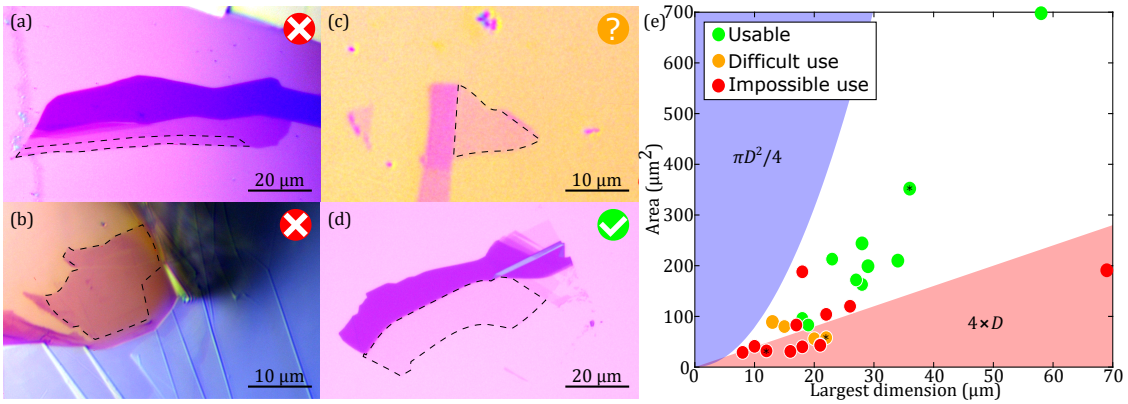


Figure 4.1: Different limiting factors for the choice of a graphene flake. (a) Too thin flake $\sim$ 3 µm width. This flake would be impossible to align correctly. (b) Too close to a thick graphite as well as non uniformity (artifacts visible on the flake). This flake would be impossible to pick up. (c) Area on the lower acceptable limit, but geometry not fitted for superposition. This flake could be used, but the tBLG area would be small. (d) Large and uniform flake, almost rectangular geometry, only drawback is the presence of the neighbouring graphite. This flake is close to ideal. (e) Compilation of flakes found on 41 1 cm $\times$ 1 cm wafers, sorted by size. The color code shows the individual quality of the flakes. The flakes marked with a "*" were exfoliated on wafers not cleaned with O_2 plasma beforehand. The blue shaded region is the mathematically impossible region for a flake to be. The red shaded region, corresponds to rectangles with a width smaller than 4 µm, which is a good indicator for acceptable width of a flake.

Figure 4.1.a to 4.1.c displays the different factors, outside from size, leading to a usable flake or not. Fig 4.1.e illustrates graphene flakes from the 41 first 1 cm $\times$ 1 cm wafers of exfoliated graphene made during this master thesis. Only graphene flakes with a largest dimension of at least $\sim$ 10 µm have been recorded. The quality of the flakes is illustrated as well. As for quantity, both graphites[1] used produced a similar density of flakes. However, the importance of O_2 plasma cleaning of the wafers is highlighted in the figure. Indeed, 12 of the 41 wafers were not cleaned in O_2 plasma before exfoliation and yielded only 3 of the 26 reported flakes.

The intuition, based on optical contrast, of the nature of the flakes needed to be checked through Raman spectroscopy. Figure 4.2 shows the Raman spectroscopy

[1]The graphites used are Hqgraphene's "natural graphite", > 99.98% pure and NGS Naturgraphit's "graphenium flakes"

of a flake, as well as the surrounding BLG for comparison. The obtained spectra were compared to the spectra from the literature (fig 3.8) in order to determine the thicknesses of the measured regions. Almost all (10 out of 11) flakes presumed to be graphene from optical contrast turned out to effectively present a Raman signature of graphene. It can therefore be concluded that optical contrast is, in many cases, sufficient to determine whether a flake is graphene or not.

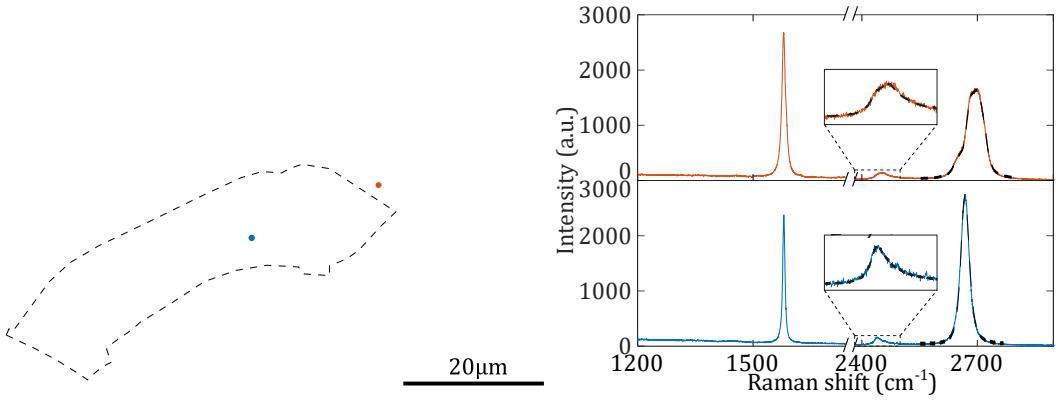


Figure 4.2: Raman spectrum of the graphene and bilayer graphene part of a flake. The picture left shows where the spectra were taken (the blue and orange dots correspond to the graphs of the same color). Right are the measured spectra. The D+D" and 2D peak are compared to the peaks from the literature from fig 3.8 (black dashed lines). Inset is a zoom-in of the D+D" peak.

4.2 h-BN flakes

h-BN flakes are a much less scarce resource than graphene flakes because their thickness can vary with a certain tolerance. Furthermore, h-BN exfoliation is a much less time-consuming process as their identification is fast due to their peculiar color. The h-BN flakes were exfoliated from h-BN crystals grown by the Japanese researchers K. Watanabe and T. Taniguchi in two different processes, labeled $M922$ and $M927$. h-BN from the $M922$ batch turned out to yield a far greater density of flakes than exfoliation from the $M927$ batch.
Nevertheless, it is important to be extremely careful with the chosen h-BN flakes as they are far more likely than graphene flakes to show surface defects. Two different types of defects, highlighted in figure 4.3 are to be avoided: glue residues (fig 4.3.a) and thickness steps (fig 4.3.b). Because of their thickness of several tens of nm, a one layer thickness step (~ 0.66 nm [76]) is barely visible to the naked eye. A dark field optical image highlights these surface defects (fig 4.3.c) and is hence a useful tool. Finally, because the h-BN is the tool used to tear the graphene in two, it is

important for the used flake to have at least one clean, straight edge (fig 4.3.d).

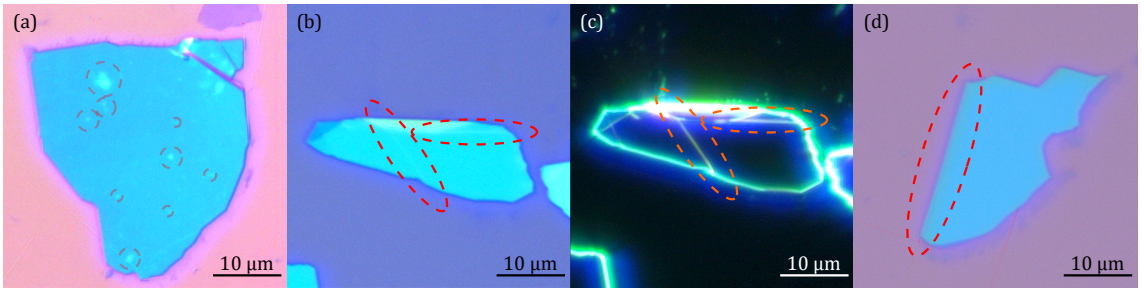


Figure 4.3: Different limiting factors for the choice of an h-BN flake. All flakes are of a targeted thickness (color), but not all are usable. (a) Presence of glue and other impurities on the flake. (b) Presence of a break on the flake, possibly indicating a thickness step. (c) Dark field view of the flake in (b), emphasizing the surface defects. (d) Clean flake with a clean, straight edge.

Because the thickness of the flake is not of much importance, Raman spectroscopy of h-BN flakes is often useless and may only confirm the "h-BN nature" of the flake.

4.3 Transfer

Figure 4.4 shows the different steps during the making of a stack[2]. As can be seen from fig 4.4.c and 4.4.d, only the part of the graphene covered by the h-BN has been picked up. This illustrates the power of this method to tear graphene apart. Figure 4.4.g shows the closed stack with some yellow stains visible on top of it. These could be either caused by bubbles/blisters of air caught between the layers [71] of the stack or by PPC residues on the top h-BN. The former hypothesis should probably be excluded as the stains are still present in the same area after etching (fig 4.4.h). However, the second hypothesis also seems unlikely, as, after 10 minutes in chloroform, the stains were still present, whereas virtually all other remaining PPC was gone. The origin of these stains remains an open question at this point. A last hypothesis could be PPC trapped inside the stack between the two graphene pick-ups. Indeed, the second graphene layer picked up is in contact with the PPC during the first graphene pick-up. But then again, on figure 4.4.a and 4.4.f, there doesn't seem to be any PPC on the unpicked graphene.

[2]The flake used is the same as the one shown in figure 4.2 after a failed pick up attempt

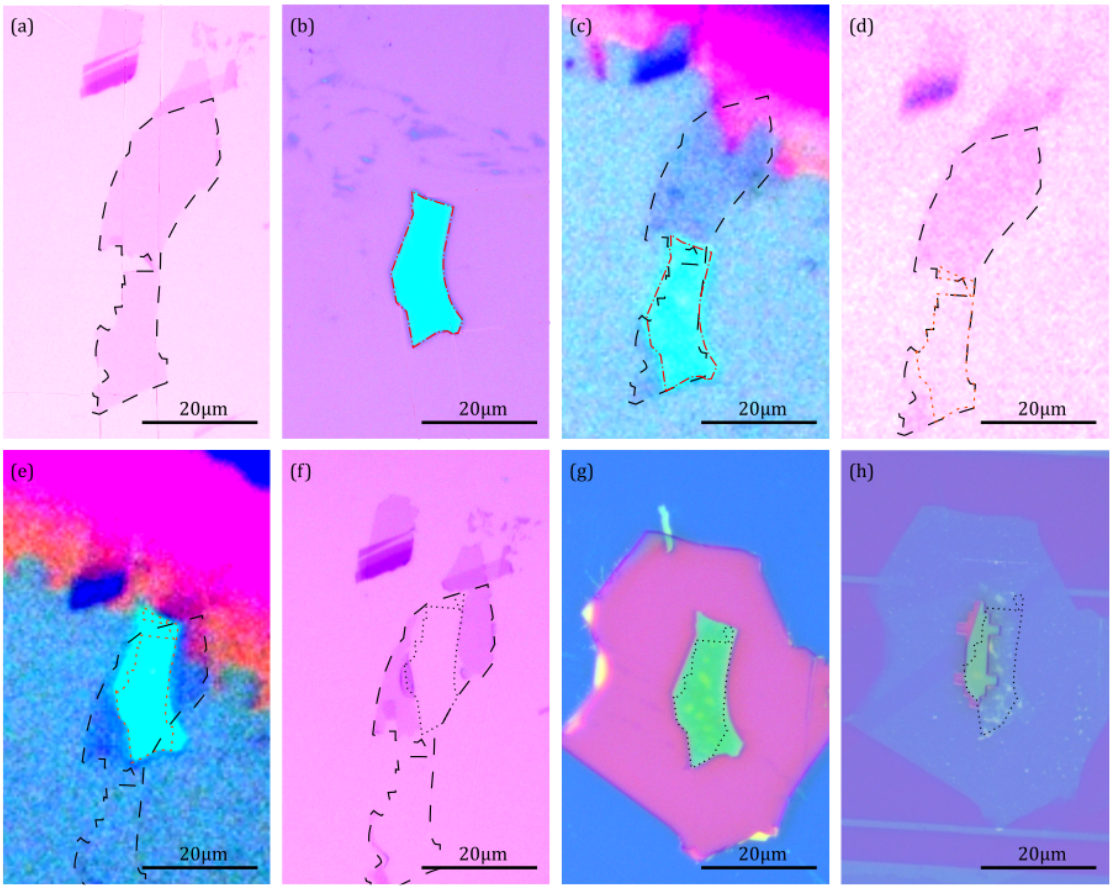


Figure 4.4: Evolution of the different steps in the fabrication process. (a) Graphene flake, surrounded by the black, long dashed line. (b) h-BN flake of appropriate size, surrounded by the red dashed-dotted line. (c) Superposition of the h-BN flake on the bottom part of the graphene flake, the contours of both flakes are the same as in images (a) and (b). (d) Remaining of the graphene flake after pick-up of the h-BN. The orange, short dashed line is obtained by taking the intersection of both flakes in image (c). The coincidence with the vanished graphene is noticeable. (e) Superposition of the stack on the top part of the graphene flake. Note that a rotation has been applied to the sample holder before putting the top graphene layer in contact with the bottom one on the wafer. (f) Remaining of the graphene flake after second pick-up. The black, dotted line is the intersection between the graphene flake and the supposed location of the first picked up graphene layer. (g) Stack closed by a bottom h-BN layer. (h) Stack after lithography. All images have increased contrast.

Other defects have been observed on all stacks made during this master thesis, all of which are shown in figure C.3 of appendix C. The most common of defects is

the breaking of the h-BN flake during all of the transfer process. In that case a break line appears on the flake, its consequences on the electronic properties of the device have not been established. A worse version of this is the complete tearing of the h-BN flakes. It can also happen that the graphene is not torn as precisely as it is in figure 4.4. Table 4.1 gives an idea of the frequency of these defects by summarizing the observed defects on all stacks. In addition to that, it also shows the stacks lost during the drop-down, emphasizing the delicateness of this step.

Stack N°	Surface stains	broken h-BN	h-BN torn	Unclear graphene cut	Stack lost
1	×				
2					×
3			×		
4	?	×			×
5		×	×		
6		×		×	
7	?				×
8		×		×	
9	×	×			
10	×				

Table 4.1: Defects observed on different stacks. Stack 1 is shown in figure 4.4, while stacks 2 to 10 are shown in figure C.3. The "?" symbols indicate the inability to check for the presence of stains because of a loss of the stack during the final transfer step.

4.4 Lithography and etching

The last part of the process (lithography and etching) presented some challenges. As can be seen from figure 4.4.h, the lithography hasn't precisely been centered on the flake. In practice, the lithography could simply have been restarted before the etching, but given that at least 4 contact points could be found, it has been decided not to be restarted. Other lithography results are shown in figure C.4 of appendix C. The main difficulty with the lithography process is the reporting of the exact position of the stack on the substrate. This is because h-BN (a thin insulating layer) on top SiO_2 (another insulating layer) shows very little contrast in SEM imagery. This is also shown in figure C.4 of appendix C.

Regarding the etching process, tests were performed as explained in section 3.6. Because of technical constraints, a few parameters were changed from the given

recipes. For the SF_6/Ar recipe, the pressure was set to 20 mTorr and the etching time to 23 s. 3 seconds were added for the initialization of the process. For the CHF_3/O_2 recipe, a few changes were brought as well for practical reasons. First, the HSQ layer was left behind, replacing it instead by a thicker PMMA layer. Second, the RF power was lowered to 10 W. The ICP power and operation pressure, not mentioned in the reference, were set to 2000 W and 20 mTorr respectively. The exposure time was set to 45 s. The results of the etching tests are summarized in table 4.2 and shown in figure 4.5.

	SF_6/Ar			CHF_3/O_2		
	h-BN	SiO_2	PMMA	h-BN	SiO_2	PMMA
Before	Present	278	192	Present	279	201
After	Gone	258	164	Blue flakes almost gone	236	97

Table 4.2: Thicknesses of the indicated layers before and after for both etching tests. All values are measured with an ellipsometer and expressed in nm.

The results for the SF_6/Ar process respect the constraints stated in section 3.6. On the contrary, the CHF_3/O_2 process yields results at the lower acceptable limit according to the constraints stated in section 3.6. Indeed, the SiO_2 as well as the PMMA are deeply etched (resp 43 and 104 nm), while the h-BN flakes are still visible (although etched as well). While the CHF_3/O_2 process is preferred in the literature for the inclined walls it delivers, its selectivity issues have prevented it from being used on any stack during this master thesis. This is a challenge that should probably be addressed in the future.

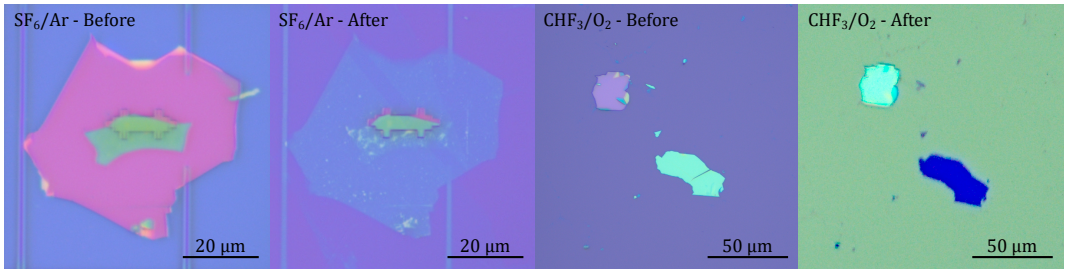


Figure 4.5: Results of the two etching recipes. Left: etching of a stack using SF_6/Ar. These are images of the etching of a stack instead of from the test due to image quality issues. Right: etching of h-BN flakes using CHF_3/O_2. The change in background color ($\sim SiO_2$ thickness) is far more pronounced right than left, while the etching of the h-BN is complete left and only partially complete right. This illustrates the selectivity issues with the CHF_3/O_2.

4.5 Characterization

The stacks obtained in the previous section have also been characterized. Two things were tested: the presence of a twist angle, if any at all, and the presence of graphene/tBLG at the desired contact points. Both of these were tested with a Raman spectroscopy. The results of the testing on the contact points, as well as at different locations on the Hall bar, are shown in figure 4.6. The rightmost peak in all of the spectra is the h-BN peak. The other peaks are the graphene peaks discussed in the section about Raman spectroscopy. Graphene is indeed present at all the expected contact points, which is promising for further contacting. However, all spectra do not look exactly the same, despite similar trends such as asymmetric G and 2D peaks.

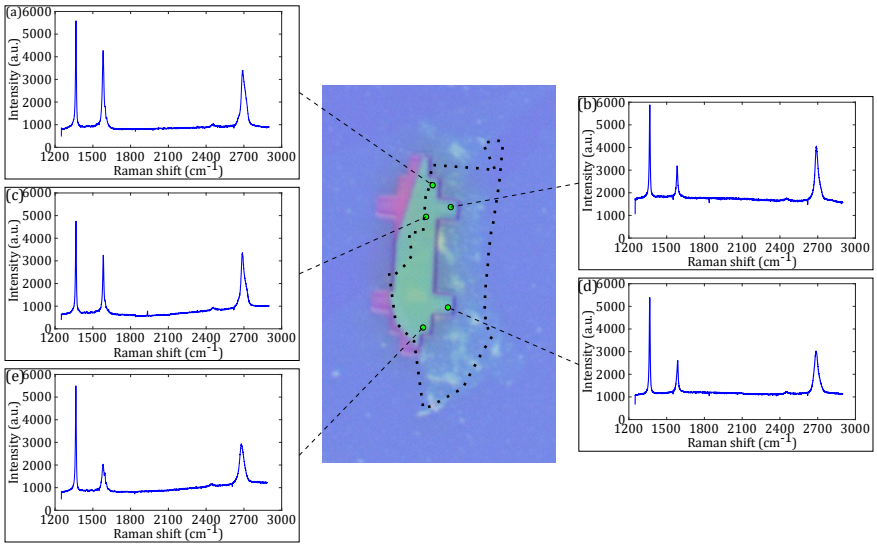


Figure 4.6: Raman spectra at the different contact points as well as one centered spectrum. The thick black dotted contour is the expected location of tBLG in the stack before etching. The green dots indicate the point where each spectrum was taken.

More quantitatively, three things were analyzed in these spectra: the presence of a new D peak, the presence of a new R' peak and the characteristics of the 2D peaks. The first feature (D peak) is examined in order to determine whether some defects have been created by the stacking or etching procedure. The other two features (R' and 2D peak) were examined to try determine the twist angle.
First of all, no extra peak could be found in the vicinity of 1350 cm^{-1} as shown in figure C.5 of appendix C. This means that no D peak is visible.
If a R' peak appeared, it is to be found in the vicinity of the G peak of the spectra.

The top row of figure 4.7 shows an analysis of the G peak in the spectra of SLG, BLG and tBLG. The peak from the tBLG seems to be composed of three peaks, one of which (at 1581.6 cm^{-1}) is the usual G peak while the two others are new. These two new peak are visible on three out of the five spectra shown in figure 4.6 (spectra (a), (c) and (e), cfr. appendix C, figure C.6). Each time, they are located at respectively 1599 and 1611 cm^{-1}. The first one (at 1599 cm^{-1}) could be associated with the R' peak shown in figure 3.10. According to the analysis presented in ref [65], this should correspond to a twist angle of $\sim 1.8°$. No explanation for the second of these new peaks has been found in the literature.

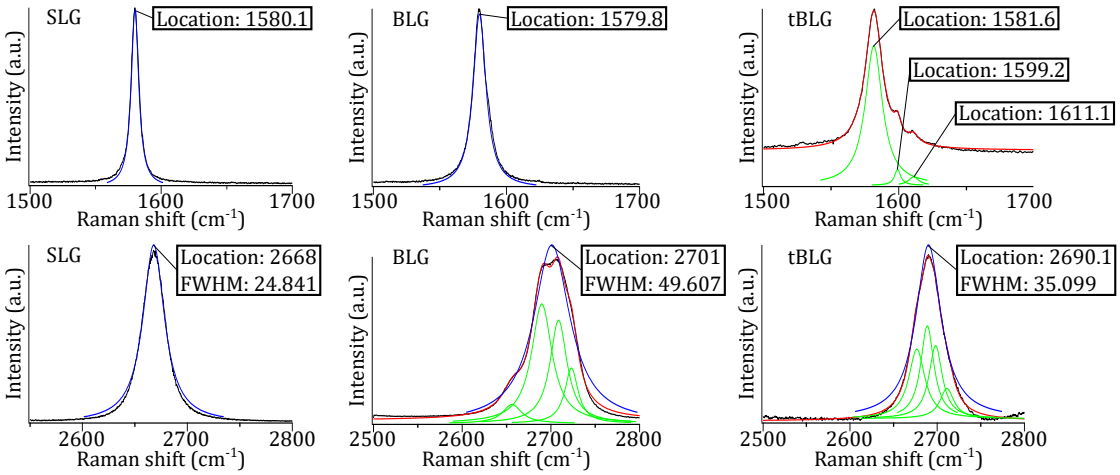


Figure 4.7: Top row: analysis and decomposition of the G peak in SLG, BLG and tBLG. The peak in the tBLG spectrum seems to be composed of three peaks at the given locations. The tBLG peak is the one from spectrum (a) in figure 4.6. Bottom row, analysis and decomposition of the 2D peak in SLG, BLG and tBLG. The tBLG peak has been specially acquired in the center of the stack shown in figure 4.6. In all of these figures, the black curve show the measured spectrum, the red curve shows the 3 or 4 Lorentzian fit, with the green curves composing it and the blue curve shows the fit using only one Lorentzian.

The bottom row of figure 4.7 shows the analysis of the 2D peak. Four components of the 2D peak could be found and analyzed. The width and location of the one Lorentzian fit of the tBLG 2D peak indicate the presence of a twist angle. This is because, at small angles, the width and position are very sensitive to the twist angle, according to fig 3.9. That angle, could not be determined according to the same reference, as the measured data do not correspond to any plausible angle. Surprisingly, the position of the 2D peak for graphene is shifted compared to values found in the literature (2676 cm^{-1} on Si/SiO_2 [59]). Estimating the blueshift of the

2D peak in tBLG relative to its position in SLG as found in the literature instead of the one measured would yield a twist angle of 1 to 2° according to the analysis presented in figure 3.9. A similar analysis would nevertheless not match with the measurement of the position of the 2D peak in Bernal stacked BLG.

4.6 Stack flips

As mentioned several times, the stack flip method is not suited for tBLG samples. Nevertheless, it may prove to be a useful method for other applications as it does not require the presence of a top h-BN flake. Therefore, a few trials of this method were performed during this master thesis. One may wonder if dropping a stack, albeit slowly, from a height of several hundreds of µm (the height of a crumpled PPC layer) could affect the stack's physical integrity. It turns out that the stacks in stack flip methods are dropped in a perfectly flat way as illustrated in figure 4.8.

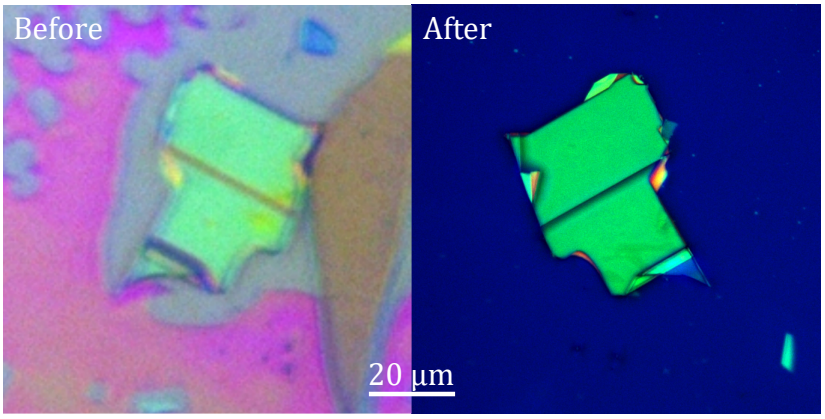


Figure 4.8: Stack before and after flipping. The stack on the left appears to be a mirror image of the stack on the right, indicating that the flipping of it has been a success.

Chapter 5

Conclusion and perspectives

This master thesis' purpose was to dive into the new promising field of twisted bilayer graphene. To begin with, an understanding of the properties of these structures was necessary. Because of its flat band structure, magic angle tBLG opens a surprisingly easy way to access strongly correlated phenomena. Furthermore, the shortcomings of simulation tools to model magic angle tBLG structures make it a continuously surprising material, e.g. the unexpected discovery of superconductivity in 2018. Its experimental study may turn out to be very precious in understanding strongly correlated systems.
The main aspect of this master thesis' was the development of a suitable fabrication technique for such devices. Mechanical exfoliation of graphene and h-BN has produced the desired results with the creation of very uniform flakes, suitable for further transfer. Furthermore, the transfer technique, adapted from [70] and [71] turned out to be efficient for the stacking of these 2D materials, given the appropriate tools. The only, unexpected, difficulty arose from the drop-down step, which has often lead to stack losses. The formation of the twisted graphene bilayer by tearing of single domain SLG flakes also turned out to be extremely precise as optical images have shown. Finally, the lithography and etching processes worked, but not without posing several challenges. The lithography's precision was limited by the precise identification of the flake's position. The etching processes with CHF_3 and SF_6 respectively lead to selectivity issues between h-BN and SiO_2 and to very vertical edges, hard to contact.
Characterization of the produced samples yielded contrasted results. On the one hand, Raman spectroscopy of the samples indicated the presence of, what seems to be, twisted bilayer graphene as desired. On the other hand, optical images of every sample showed all sorts of defects present, from yet unidentified stains to broken lines in the stack. The problem of these defects need to be addressed for an improvement of the method.
Unfortunately, due to several technical issues, the process couldn't be totally com-

pleted, making electronic transport characterization impossible at this stage. This would have been the final step of the present master thesis, but will instead be left for future candidates.

From a wider point of view, plenty of future developments are still possible in this domain. Twistronics in graphene is a promising field of research and not only limited to tBLG. Recent works on twisted double bilayer graphene [83, 68, 84] (two Bernal stacked BLG stacked onto each other, with a twist angle) have shown the presence of superconductivity up to 12 K at a slightly larger twist angle of 1.28°. Other theoretical works predict similar phenomena in twisted multilayer graphene that still need to be explored [85, 86]. All of these structures are accessible with the method developed in this master thesis.
Other developments are possible in the process. For now, the limiting factor of the process is the size of the available graphene flakes. Because the exfoliation process is extremely time-consuming and the entire structure needs to be made from the same flake, mass production of twisted graphene structures is still complicated. Furthermore, the accessible number layers is limited for the same dimensional reason. CVD produced graphene flakes are available with far greater dimensions and would solve this problem. Therefore, progress in the quality of CVD produced graphene flakes [54] as well as of their transfer process [87] may be a key element in the development of this field.
Next, development of in situ rotatable twisted heterostructure devices [88] may open the door to the exploration of many other twist angles. It would also solve the thermal annealing problem as the twist angle can be redefined at any moment. That would allow for the thermal cleaning of the samples, mentioned in the process description, possibly yielding even clearer results.
Finally, a better theoretical understanding of the observed phenomena, such as superconductivity, is crucial for further developments in this domain.

Chapter 6

Acknowledgements

This work would not have been possible without the help of several people that I would like to thank in this chapter. Of course, I would like to thank my supervisor *Pr. Benoît Hackens* for giving me the chance to work on this project. His availability, ideas and precious advice have allowed me to discover so many aspects of the world of experimental physics and brought me to the end of this thesis.
Other people have also contributed to this project and for this reason I would like to thank *Sébastien Faniel*, *Romain Tuyaerts* and all the WINFAB staff for their precious help with the use of the equipment. Similarly I would like to thank *Sylvain Blanco Alvarez* and *Pr. Alejandro Silhanek* from the University of Liège for offering us their time and access to their equipment when ours was failing. I would also like to thank *Boris-Brun Barrière* and *Nicolas Reckinger* for having shared inspiring articles with me.
Furthermore, I would like to thank *Nadzeya Kryvutsa* and *Wasil Malik* for the time spent with me, sharing their knowledge, skills and even precious graphene flakes during the fabrication process.
Next, I would like to thank my fellow master student *Abbas Mounzer*, working on a very similar topic, for having been an amazing teammate in this project. I knew I never struggled alone and without sharing our tips to each other, progress would have been far more complicated.
Eventually, I would like to say a huge thank you to *Nicolas Moreau* and *Sébastien Toussaint* for the hours or even days spent with me trying to find new solutions to the problems encountered and for guiding me throughout this entire project. They gave a lot of their time trying to make a success of this project and therefore deserve a big part of the credit for everything achieved.

Bibliography

[1] K. S. Novoselov, A. K. Geim, S. V. Morozov, D. Jiang, Y. Zhang, S. V. Dubonos, I. V. Grigorieva, and A. A. Firsov. Electric field effect in atomically thin carbon films. *Science*, 306(5696):666–669, 2004.

[2] J. M. B. Lopes dos Santos, N. M. R. Peres, and A. H. Castro Neto. Graphene bilayer with a twist: Electronic structure. *Phys. Rev. Lett.*, 99:256802, Dec 2007.

[3] Stephen Carr, Daniel Massatt, Shiang Fang, Paul Cazeaux, Mitchell Luskin, and Efthimios Kaxiras. Twistronics: Manipulating the electronic properties of two-dimensional layered structures through their twist angle. *Phys. Rev. B*, 95:075420, Feb 2017.

[4] Yuan Cao, Valla Fatemi, Ahmet Demir, Shiang Fang, Spencer L. Tomarken, Jason Y. Luo, Javier D. Sanchez-Yamagishi, Kenji Watanabe, Takashi Taniguchi, Efthimios Kaxiras, Ray C. Ashoori, and Pablo Jarillo-Herrero. Correlated insulator behaviour at half-filling in magic-angle graphene superlattices. *Nature*, 556:80 EP –, Mar 2018.

[5] Yuan Cao, Valla Fatemi, Shiang Fang, Kenji Watanabe, Takashi Taniguchi, Efthimios Kaxiras, and Pablo Jarillo-Herrero. Unconventional superconductivity in magic-angle graphene superlattices. *Nature*, 556:43 EP –, Mar 2018. Article.

[6] A. H. Castro Neto, F. Guinea, N. M. R. Peres, K. S. Novoselov, and A. K. Geim. The electronic properties of graphene. *Rev. Mod. Phys.*, 81:109–162, Jan 2009.

[7] J.-N. Fuchs and M. O. Goerbig. Introduction to the physical properties of graphene. Lecture notes, Université Paris-Sorbonne, 2008.

[8] Changgu Lee, Xiaoding Wei, Jeffrey W. Kysar, and James Hone. Measurement of the elastic properties and intrinsic strength of monolayer graphene. *Science*, 321(5887):385–388, 2008.

[9] Duhee Yoon, Young-Woo Son, and Hyeonsik Cheong. Negative thermal expansion coefficient of graphene measured by raman spectroscopy. *Nano Letters*, 11(8):3227–3231, Aug 2011.

[10] L A Falkovsky. Optical properties of graphene. *Journal of Physics: Conference Series*, 129:012004, oct 2008.

[11] Hengji Zhang, Geunsik Lee, and Kyeongjae Cho. Thermal transport in graphene and effects of vacancy defects. *Phys. Rev. B*, 84:115460, Sep 2011.

[12] Alexander A. Balandin, Suchismita Ghosh, Wenzhong Bao, Irene Calizo, Desalegne Teweldebrhan, Feng Miao, and Chun Ning Lau. Superior thermal conductivity of single-layer graphene. *Nano Letters*, 8(3):902–907, Mar 2008.

[13] K. S. Novoselov, A. K. Geim, S. V. Morozov, D. Jiang, M. I. Katsnelson, I. V. Grigorieva, S. V. Dubonos, and A. A. Firsov. Two-dimensional gas of massless dirac fermions in graphene. *Nature*, 438(7065):197–200, 2005.

[14] D. G. Purdie, N. M. Pugno, T. Taniguchi, K. Watanabe, A. C. Ferrari, and A. Lombardo. Cleaning interfaces in layered materials heterostructures. *Nature Communications*, 9(1):5387, 2018.

[15] David Tong. Lectures on the Quantum Hall Effect. *arXiv e-prints*, page arXiv:1606.06687, Jun 2016.

[16] Lei Liu, Y. P. Feng, and Z. X. Shen. Structural and electronic properties of h-bn. *Phys. Rev. B*, 68:104102, Sep 2003.

[17] Li Song, Lijie Ci, Hao Lu, Pavel B. Sorokin, Chuanhong Jin, Jie Ni, Alexander G. Kvashnin, Dmitry G. Kvashnin, Jun Lou, Boris I. Yakobson, and Pulickel M. Ajayan. Large scale growth and characterization of atomic hexagonal boron nitride layers. *Nano Letters*, 10(8):3209–3215, Aug 2010.

[18] Pilkyung Moon and Mikito Koshino. Energy spectrum and quantum hall effect in twisted bilayer graphene. *Phys. Rev. B*, 85:195458, May 2012.

[19] S. Shallcross, S. Sharma, E. Kandelaki, and O. A. Pankratov. Electronic structure of turbostratic graphene. *Phys. Rev. B*, 81:165105, Apr 2010.

[20] Shuyang Dai, Yang Xiang, and David J. Srolovitz. Twisted bilayer graphene: Moiré with a twist. *Nano Letters*, 16(9):5923–5927, 2016. PMID: 27533089.

[21] E. Suárez Morell, J. D. Correa, P. Vargas, M. Pacheco, and Z. Barticevic. Flat bands in slightly twisted bilayer graphene: Tight-binding calculations. *Phys. Rev. B*, 82:121407, Sep 2010.

[22] J. M. B. Lopes dos Santos, N. M. R. Peres, and A. H. Castro Neto. Continuum model of the twisted graphene bilayer. *Phys. Rev. B*, 86:155449, Oct 2012.

[23] Shiang Fang and Efthimios Kaxiras. Electronic structure theory of weakly interacting bilayers. *Phys. Rev. B*, 93:235153, Jun 2016.

[24] G. Trambly de Laissardière, D. Mayou, and L. Magaud. Numerical studies of confined states in rotated bilayers of graphene. *Phys. Rev. B*, 86:125413, Sep 2012.

[25] G. Trambly de Laissardière, D. Mayou, and L. Magaud. Localization of dirac electrons in rotated graphene bilayers. *Nano Letters*, 10(3):804–808, Mar 2010.

[26] Nguyen N. T. Nam and Mikito Koshino. Lattice relaxation and energy band modulation in twisted bilayer graphene. *Phys. Rev. B*, 96:075311, Aug 2017.

[27] Stephen Carr, Shiang Fang, Pablo Jarillo-Herrero, and Efthimios Kaxiras. Pressure dependence of the magic twist angle in graphene superlattices. *Phys. Rev. B*, 98:085144, Aug 2018.

[28] Rafi Bistritzer and Allan H. MacDonald. Moiré bands in twisted double-layer graphene. *Proceedings of the National Academy of Sciences*, 108(30):12233–12237, 2011.

[29] Yuan Cao, Debanjan Chowdhury, Daniel Rodan-Legrain, Oriol Rubies-Bigordà, Kenji Watanabe, Takashi Taniguchi, T. Senthil, and Pablo Jarillo-Herrero. Strange metal in magic-angle graphene with near Planckian dissipation. *arXiv e-prints*, page arXiv:1901.03710, Jan 2019.

[30] Aaron L. Sharpe, Eli J. Fox, Arthur W. Barnard, Joe Finney, Kenji Watanabe, Takashi Taniguchi, M. A. Kastner, and David Goldhaber-Gordon. Emergent ferromagnetism near three-quarters filling in twisted bilayer graphene. *arXiv e-prints*, page arXiv:1901.03520, Jan 2019.

[31] Javier D. Sanchez-Yamagishi, Jason Y. Luo, Andrea F. Young, Benjamin M. Hunt, Kenji Watanabe, Takashi Taniguchi, Raymond C. Ashoori, and Pablo Jarillo-Herrero. Helical edge states and fractional quantum hall effect in a graphene electron-hole bilayer. *Nature Nanotechnology*, 12:118 EP –, Oct 2016.

[32] Matthew Yankowitz, Shaowen Chen, Hryhoriy Polshyn, Yuxuan Zhang, K. Watanabe, T. Taniguchi, David Graf, Andrea F. Young, and Cory R. Dean. Tuning superconductivity in twisted bilayer graphene. *Science*, 363(6431):1059–1064, 2019.

[33] Emilio Codecido, Qiyue Wang, Ryan Koester, Shi Che, Haidong Tian, Rui Lv, Son Tran, Kenji Watanabe, Takashi Taniguchi, Fan Zhang, Marc Bockrath, and Chun Ning Lau. Correlated Insulating and Superconducting States in Twisted Bilayer Graphene Below the Magic Angle. *arXiv e-prints*, page arXiv:1902.05151, Feb 2019.

[34] Xiaobo Lu, Petr Stepanov, Wei Yang, Ming Xie, Mohammed Ali Aamir, Ipsita Das, Carles Urgell, Kenji Watanabe, Takashi Taniguchi, Guangyu Zhang, Adrian Bachtold, Allan H. MacDonald, and Dmitri K. Efetov. Superconductors, Orbital Magnets, and Correlated States in Magic Angle Bilayer Graphene. *arXiv e-prints*, page arXiv:1903.06513, Mar 2019.

[35] Bikash Padhi, Chandan Setty, and Philip W. Phillips. Doped twisted bilayer graphene near magic angles: Proximity to wigner crystallization, not mott insulation. *Nano Letters*, 18(10):6175–6180, Oct 2018.

[36] Y J Uemura. Condensation, excitation, pairing, and superfluid density in high-tc superconductors: the magnetic resonance mode as a roton analogue and a possible spin-mediated pairing. *Journal of Physics: Condensed Matter*, 16(40):S4515–S4540, sep 2004.

[37] G. R. Stewart. Unconventional superconductivity. *Advances in Physics*, 66(2):75–196, Apr 2017.

[38] H. Polshyn, M. Yankowitz, S. Chen, Y. Zhang, K. Watanabe, T. Taniguchi, C. R. Dean, and A. F. Young. Phonon scattering dominated electron transport in twisted bilayer graphene. *arXiv e-prints*, page arXiv:1902.00763, Feb 2019.

[39] Fengcheng Wu, A. H. MacDonald, and Ivar Martin. Theory of phonon-mediated superconductivity in twisted bilayer graphene. *Phys. Rev. Lett.*, 121:257001, Dec 2018.

[40] Biao Lian, Zhijun Wang, and B. Andrei Bernevig. Twisted Bilayer Graphene: A Phonon Driven Superconductor. *arXiv e-prints*, page arXiv:1807.04382, Jul 2018.

[41] Douglas R. Hofstadter. Energy levels and wave functions of bloch electrons in rational and irrational magnetic fields. *Phys. Rev. B*, 14:2239–2249, Sep 1976.

[42] R. Bistritzer and A. H. MacDonald. Moiré butterflies in twisted bilayer graphene. *Phys. Rev. B*, 84:035440, Jul 2011.

[43] Sung Joon Ahn, Pilkyung Moon, Tae-Hoon Kim, Hyun-Woo Kim, Ha-Chul Shin, Eun Hye Kim, Hyun Woo Cha, Se-Jong Kahng, Philip Kim, Mikito

Koshino, Young-Woo Son, Cheol-Woong Yang, and Joung Real Ahn. Dirac electrons in a dodecagonal graphene quasicrystal. *Science*, 361(6404):782–786, 2018.

[44] Laura C. Collins, Thomas G. Witte, Rochelle Silverman, David B. Green, and Kenjiro K. Gomes. Imaging quasiperiodic electronic states in a synthetic penrose tiling. *Nature Communications*, 8:15961 EP –, Jun 2017. Article.

[45] Yaacov E. Kraus, Zohar Ringel, and Oded Zilberberg. Four-dimensional quantum hall effect in a two-dimensional quasicrystal. *Phys. Rev. Lett.*, 111:226401, Nov 2013.

[46] Elad Koren and Urs Duerig. Superlubricity in quasicrystalline twisted bilayer graphene. *Phys. Rev. B*, 93:201404, May 2016.

[47] Abhay A. Sagade, Daniel Neumaier, Daniel Schall, Martin Otto, Amaia Pesquera, Alba Centeno, Amaia Zurutuza Elorza, and Heinrich Kurz. Highly air stable passivation of graphene based field effect devices. *Nanoscale*, 7:3558–3564, 2015.

[48] Alexander S. Mayorov, Roman V. Gorbachev, Sergey V. Morozov, Liam Britnell, Rashid Jalil, Leonid A. Ponomarenko, Peter Blake, Kostya S. Novoselov, Kenji Watanabe, Takashi Taniguchi, and A. K. Geim. Micrometer-scale ballistic transport in encapsulated graphene at room temperature. *Nano Letters*, 11(6):2396–2399, Jun 2011.

[49] C. R. Dean, A. F. Young, I. Meric, C. Lee, L. Wang, S. Sorgenfrei, K. Watanabe, T. Taniguchi, P. Kim, K. L. Shepard, and J. Hone. Boron nitride substrates for high-quality graphene electronics. *Nature Nanotechnology*, 5:722 EP –, Aug 2010.

[50] L. A. Ponomarenko, R. V. Gorbachev, G. L. Yu, D. C. Elias, R. Jalil, A. A. Patel, A. Mishchenko, A. S. Mayorov, C. R. Woods, J. R. Wallbank, M. Mucha-Kruczynski, B. A. Piot, M. Potemski, I. V. Grigorieva, K. S. Novoselov, F. Guinea, V. I. Fal'ko, and A. K. Geim. Cloning of dirac fermions in graphene superlattices. *Nature*, 497:594 EP –, May 2013.

[51] K. S. Novoselov, V. I. Fal'ko, L. Colombo, P. R. Gellert, M. G. Schwab, and K. Kim. A roadmap for graphene. *Nature*, 490:192 EP –, Oct 2012. Review Article.

[52] Caterina Soldano, Ather Mahmood, and Erik Dujardin. Production, properties and potential of graphene. *Carbon*, 48(8):2127 – 2150, 2010.

[53] Francesco Bonaccorso, Antonio Lombardo, Tawfique Hasan, Zhipei Sun, Luigi Colombo, and Andrea C. Ferrari. Production and processing of graphene and 2d crystals. *Materials Today*, 15(12):564 – 589, 2012.

[54] Luca Banszerus, Michael Schmitz, Stephan Engels, Jan Dauber, Martin Oellers, Federica Haupt, Kenji Watanabe, Takashi Taniguchi, Bernd Beschoten, and Christoph Stampfer. Ultrahigh-mobility graphene devices from chemical vapor deposition on reusable copper. *Science Advances*, 1(6), 2015.

[55] Yuan Huang, Eli Sutter, Norman N. Shi, Jiabao Zheng, Tianzhong Yang, Dirk Englund, Hong-Jun Gao, and Peter Sutter. Reliable exfoliation of large-area high-quality flakes of graphene and other two-dimensional materials. *ACS Nano*, 9(11):10612–10620, Nov 2015.

[56] Gurvinder Singh Bumbrah and Rakesh Mohan Sharma. Raman spectroscopy – basic principle, instrumentation and selected applications for the characterization of drugs of abuse. *Egyptian Journal of Forensic Sciences*, 6(3):209 – 215, 2016.

[57] Horiba Scientific. What laser wavelengths are used for raman spectroscopy? `http://www.horiba.com/us/en/scientific/products/raman-spectroscopy/raman-academy/raman-faqs/what-laser-wavelengths-are-used-for-raman-spectroscopy/`. Accessed: 2019-05-22.

[58] Andrea C. Ferrari and Denis M. Basko. Raman spectroscopy as a versatile tool for studying the properties of graphene. *Nature Nanotechnology*, 8:235 EP –, Apr 2013. Review Article.

[59] Zhenhua Ni, Yingying Wang, Ting Yu, and Zexiang Shen. Raman spectroscopy and imaging of graphene. *Nano Research*, 1(4):273–291, Oct 2008.

[60] Patrick May, Michele Lazzeri, Pedro Venezuela, Felix Herziger, Gordon Callsen, Juan S. Reparaz, Axel Hoffmann, Francesco Mauri, and Janina Maultzsch. Signature of the two-dimensional phonon dispersion in graphene probed by double-resonant raman scattering. *Phys. Rev. B*, 87:075402, Feb 2013.

[61] L. G. Cançado, A. Reina, J. Kong, and M. S. Dresselhaus. Geometrical approach for the study of G' band in the raman spectrum of monolayer graphene, bilayer graphene, and bulk graphite. *Phys. Rev. B*, 77:245408, Jun 2008.

[62] A. C. Ferrari, J. C. Meyer, V. Scardaci, C. Casiraghi, M. Lazzeri, F. Mauri, S. Piscanec, D. Jiang, K. S. Novoselov, S. Roth, and A. K. Geim. Raman

spectrum of graphene and graphene layers. *Phys. Rev. Lett.*, 97:187401, Oct 2006.

[63] E. H. Martins Ferreira, Marcus V. O. Moutinho, F. Stavale, M. M. Lucchese, Rodrigo B. Capaz, C. A. Achete, and A. Jorio. Evolution of the raman spectra from single-, few-, and many-layer graphene with increasing disorder. *Phys. Rev. B*, 82:125429, Sep 2010.

[64] Kwanpyo Kim, Sinisa Coh, Liang Z. Tan, William Regan, Jong Min Yuk, Eric Chatterjee, M. F. Crommie, Marvin L. Cohen, Steven G. Louie, and A. Zettl. Raman spectroscopy study of rotated double-layer graphene: Misorientation-angle dependence of electronic structure. *Phys. Rev. Lett.*, 108:246103, Jun 2012.

[65] Victor Carozo, Clara M. Almeida, Erlon H. M. Ferreira, Luiz Gustavo Cançado, Carlos Alberto Achete, and Ado Jorio. Raman signature of graphene superlattices. *Nano Letters*, 11(11):4527–4534, Nov 2011.

[66] Mengjian Zhu, Davit Ghazaryan, Seok-Kyun Son, Colin R Woods, Abhishek Misra, Lin He, Takashi Taniguchi, Kenji Watanabe, Kostya S Novoselov, Yang Cao, and Artem Mishchenko. Stacking transition in bilayer graphene caused by thermally activated rotation. *2D Materials*, 4(1):011013, dec 2016.

[67] Duoming Wang, Guorui Chen, Chaokai Li, Meng Cheng, Wei Yang, Shuang Wu, Guibai Xie, Jing Zhang, Jing Zhao, Xiaobo Lu, Peng Chen, Guole Wang, Jianling Meng, Jian Tang, Rong Yang, Congli He, Donghua Liu, Dongxia Shi, Kenji Watanabe, Takashi Taniguchi, Ji Feng, Yuanbo Zhang, and Guangyu Zhang. Thermally induced graphene rotation on hexagonal boron nitride. *Phys. Rev. Lett.*, 116:126101, Mar 2016.

[68] Xiaomeng Liu, Zeyu Hao, Eslam Khalaf, Jong Yeon Lee, Kenji Watanabe, Takashi Taniguchi, Ashvin Vishwanath, and Philip Kim. Spin-polarized Correlated Insulator and Superconductor in Twisted Double Bilayer Graphene. *arXiv e-prints*, page arXiv:1903.08130, Mar 2019.

[69] W. Gannett, W. Regan, K. Watanabe, T. Taniguchi, M. F. Crommie, and A. Zettl. Boron nitride substrates for high mobility chemical vapor deposited graphene. *Applied Physics Letters*, 98(24):242105, 2011.

[70] L. Wang, I. Meric, P. Y. Huang, Q. Gao, Y. Gao, H. Tran, T. Taniguchi, K. Watanabe, L. M. Campos, D. A. Muller, J. Guo, P. Kim, J. Hone, K. L. Shepard, and C. R. Dean. One-dimensional electrical contact to a two-dimensional material. *Science*, 342(6158):614–617, 2013.

[71] Filippo Pizzocchero, Lene Gammelgaard, Bjarke S. Jessen, José M. Caridad, Lei Wang, James Hone, Peter Bøggild, and Timothy J. Booth. The hot pick-up technique for batch assembly of van der waals heterostructures. *Nature Communications*, 7:11894 EP –, Jun 2016. Article.

[72] Kyounghwan Kim, Matthew Yankowitz, Babak Fallahazad, Sangwoo Kang, Hema C. P. Movva, Shengqiang Huang, Stefano Larentis, Chris M. Corbet, Takashi Taniguchi, Kenji Watanabe, Sanjay K. Banerjee, Brian J. LeRoy, and Emanuel Tutuc. van der waals heterostructures with high accuracy rotational alignment. *Nano Letters*, 16(3):1989–1995, 2016. PMID: 26859527.

[73] Gerrit. A. Luinstra and Endres Borchardt. *Material Properties of Poly(Propylene Carbonates)*, pages 29–48. Springer Berlin Heidelberg, Berlin, Heidelberg, 2012.

[74] H.B. Ribeiro, K. Sato, G.S.N. Eliel, E.A.T. de Souza, Chun-Chieh Lu, Po-Wen Chiu, R. Saito, and M.A. Pimenta. Origin of van hove singularities in twisted bilayer graphene. *Carbon*, 90:138 – 145, 2015.

[75] P. J. Zomer, M. H. D. Guimarães, J. C. Brant, N. Tombros, and B. J. van Wees. Fast pick up technique for high quality heterostructures of bilayer graphene and hexagonal boron nitride. *Applied Physics Letters*, 105(1):013101, 2014.

[76] X.H. Li, Y.Z. Meng, Q. Zhu, and S.C. Tjong. Thermal decomposition characteristics of poly(propylene carbonate) using tg/ir and py-gc/ms techniques. *Polymer Degradation and Stability*, 81(1):157 – 165, 2003.

[77] K. Erickson. Thermal decomposition mechanisms common to polyurethane, epoxy, poly(diallyl phthalate), polycarbonate and poly(phenylene sulfide). *Journal of Thermal Analysis and Calorimetry*, 89(2):427–440, 2007.

[78] M. Ferriol, A. Gentilhomme, M. Cochez, N. Oget, and J.L. Mieloszynski. Thermal degradation of poly(methyl methacrylate) (pmma): modelling of dtg and tg curves. *Polymer Degradation and Stability*, 79(2):271 – 281, 2003.

[79] H. Sharifi and G. Gardner. Plasma rie etching fundamentals and applications. Lecture slides, Purdue University, 2008.

[80] Marta Autore, Peining Li, Irene Dolado, Francisco J. Alfaro-Mozaz, Ruben Esteban, Ainhoa Atxabal, Fèlix Casanova, Luis E. Hueso, Pablo Alonso-González, Javier Aizpurua, Alexey Y. Nikitin, Saül Vélez, and Rainer Hillenbrand. Boron nitride nanoresonators for phonon-enhanced molecular vibrational spectroscopy at the strong coupling limit. *Light: Science &Amp; Applications*, 7:17172 EP –, Apr 2018. Article.

[81] Johannes E. Fröch, Yongsop Hwang, Sejeong Kim, Igor Aharonovich, and Milos Toth. Fabrication of photonic nanostructures from hexagonal boron nitride. *arXiv e-prints*, page arXiv:1809.07561, Sep 2018.

[82] T. Chari, I. Meric, C. Dean, and K. Shepard. Properties of self-aligned short-channel graphene field-effect transistors based on boron-nitride-dielectric encapsulation and edge contacts. *IEEE Transactions on Electron Devices*, 62(12):4322–4326, Dec 2015.

[83] Cheng Shen, Na Li, Shuopei Wang, Yanchong Zhao, Jian Tang, Jieying Liu, Jinpeng Tian, Yanbang Chu, Kenji Watanabe, and Takashi Taniguchi. Observation of superconductivity with Tc onset at 12K in electrically tunable twisted double bilayer graphene. *arXiv e-prints*, page arXiv:1903.06952, Mar 2019.

[84] Yuan Cao, Daniel Rodan-Legrain, Oriol Rubies-Bigordà, Jeong Min Park, Kenji Watanabe, Takashi Taniguchi, and Pablo Jarillo-Herrero. Electric Field Tunable Correlated States and Magnetic Phase Transitions in Twisted Bilayer-Bilayer Graphene. *arXiv e-prints*, page arXiv:1903.08596, Mar 2019.

[85] Cenke Xu and Leon Balents. Topological superconductivity in twisted multilayer graphene. *Phys. Rev. Lett.*, 121:087001, Aug 2018.

[86] E. Suárez Morell, M. Pacheco, L. Chico, and L. Brey. Electronic properties of twisted trilayer graphene. *Phys. Rev. B*, 87:125414, Mar 2013.

[87] D. De Fazio, D. G. Purdie, A. K. Ott, P. Braeuninger-Weimer, T. Khodkov, S. Goossens, T. Taniguchi, K. Watanabe, P. Livreri, and F. H. L. Koppens. High-mobility, wet-transferred graphene grown by chemical vapor deposition. *arXiv e-prints*, page arXiv:1904.01405, Apr 2019.

[88] Rebeca Ribeiro-Palau, Changjian Zhang, Kenji Watanabe, Takashi Taniguchi, James Hone, and Cory R. Dean. Twistable electronics with dynamically rotatable heterostructures. *Science*, 361(6403):690–693, 2018.

Appendix A

Commensuration condition

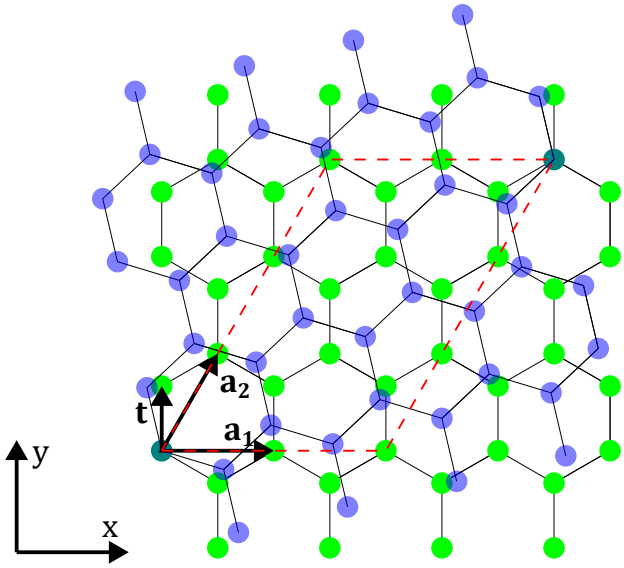


Figure A.1: Two honeycomb lattices twisted w.r.t. each other by a commensurate angle. The thick black arrows represent the defined vectors. The red dashed line indicate the closest coinciding atoms from the two lattices.

Let's define following vectors, illustrated in figure A.1:

$$\mathbf{a_1} = \begin{bmatrix} 1 \\ 0 \end{bmatrix} \quad \mathbf{a_2} = \begin{bmatrix} \frac{1}{2} \\ \frac{\sqrt{3}}{2} \end{bmatrix} \quad \mathbf{t} = \begin{bmatrix} 0 \\ \frac{1}{\sqrt{3}} \end{bmatrix} \tag{A.1}$$

Then, if (h, k) is a pair of integers, all atoms are located on points with coordinates:

$$\begin{bmatrix} h + \frac{1}{2}k \\ \frac{\sqrt{3}}{2}k \end{bmatrix} \quad or \quad \begin{bmatrix} h + \frac{1}{2}k \\ \frac{\sqrt{3}}{2}k + \frac{1}{\sqrt{3}} \end{bmatrix} \tag{A.2}$$

Rotation yields:

$$\begin{bmatrix} \cos\theta & -\sin\theta \\ \sin\theta & \cos\theta \end{bmatrix} \begin{bmatrix} h + \frac{1}{2}k \\ \frac{\sqrt{3}}{2}k \end{bmatrix} = \begin{bmatrix} \cos\theta(h + \frac{1}{2}k) - \sin\theta\frac{\sqrt{3}}{2}k \\ \sin\theta(h + \frac{1}{2}k) + \cos\theta\frac{\sqrt{3}}{2}k \end{bmatrix} \tag{A.3}$$

This is commensurate if, for some pairs of integers (h^*, k^*) and (l, m) following equality holds:

$$\begin{bmatrix} \cos\theta(h^* + \frac{1}{2}k^*) - \sin\theta\frac{\sqrt{3}}{2}k^* \\ \sin\theta(h^* + \frac{1}{2}k^*) + \cos\theta\frac{\sqrt{3}}{2}k^* \end{bmatrix} = \begin{bmatrix} l + \frac{1}{2}m \\ \frac{\sqrt{3}}{2}m \end{bmatrix} \quad or \quad \begin{bmatrix} l + \frac{1}{2}m \\ \frac{\sqrt{3}}{2}m + \frac{1}{\sqrt{3}} \end{bmatrix} \tag{A.4}$$

In other words, this yields the following equalities:

$$\cos\theta(2h^* + k^*) - \sqrt{3}\sin\theta k^* = integer \tag{A.5}$$

$$\sqrt{3}\sin\theta(2h^* + k^*) + 3\cos\theta k^* = integer \tag{A.6}$$

From this, it follows immediately that both $\cos\theta$ and $\sin\theta/\sqrt{3}$ must be rational numbers. From equations A.2 and A.3 it is then clear that all atoms of a layer rotated by a commensurate angle still have rational coordinates. If an atom had coordinates (h, k) before rotation, after rotation, its coordinates are given by:

$$k_{new} = \frac{2}{\sqrt{3}}(\sin\theta(h + \frac{1}{2}k) + \cos\theta\frac{\sqrt{3}}{2}k) = k(\cos\theta) + (2h + k)(\sin\theta/\sqrt{3}) \tag{A.7}$$

$$h_{new} = \cos\theta(h + \frac{1}{2}k) - \sin\theta\frac{\sqrt{3}}{2}k - \frac{1}{2}k_{new} = h(\cos\theta) - (h + 2k)(\sin\theta/\sqrt{3}) \tag{A.8}$$

All commensurate angles can alternatively be described as all angles θ with $\cos\theta = x/z$ and $\sin\theta/\sqrt{3} = y/z$, with (x, y, z) a solution of the Diophantine equation:

$$x^2 + 3y^2 = z^2 \tag{A.9}$$

Appendix B

Process sheet

Step	**Material**	**Parameters**
Graphene and h-BN flake production		
Wafer cleaning	• Acetone, an ultrasonic cleaner and isopropanol for rinsing • O_2 plasma chamber	• 3 min in ultrasonic cleaner • 60 s, 40 W
Graphene exfoliation	• Graphite grains • Scotch Magic Tape • 1 cm × 1 cm Si/SiO_2 wafers • Heating plate	• Quick peeling • 90°C
h-BN exfoliation	• h-BN grains • Scotch Magic Tape • Scotch Magic Greener Tape • 1 cm × 1 cm Si/SiO_2 wafers (• Vacuum furnace for cleaning)	• Slow peeling (• ∼ 300°C, 2 h)
Transfer tools		
Transfer slides	• Glass microscope slides • PDMS • Scotch Crystal Tape • PPC • 1 cm × 1 cm Si/SiO_2 wafers	

	• Spin coating machine for PPC • Heating plate	• 60 s, 2000 RPM, 1000 RPM/min • 110°C
Transfer table	• Micromanipulator, including rotatable stage • Heating/cooling module • Vacuum sample holder	
Transfer procedure		
Pick-up	• Transfer slide • Heater from the transfer table • Micromanipulator of the transfer table	• Contact front of the PPC almost at the flake • Heat up to 40°C to make contact Cool to 5°C to increase adhesion • Lift transfer slide slowly • Align stack with the next flake • Set twist angle between two graphene pick-ups
Drop-down	• Marked wafer • Transfer table	• Similar contact making as for pick-up • Heat to $\sim 80 - 90$°C • Lift transfer slide slowly (• Cool down to room temperature after contact front has passed the stack)
Lithography		
Sample preparation	• PMMA 4% vol. • Spin coating machine for PMMA • Oven	• 60 s, 4000 RPM, 1000 RPM/min • 15 min, 150°C
Exposure	• SEM	• 300 μC/cm^2, 30 kV
Development	• MIBK with isopropanol • Isopropanol for rinsing	• 1 : 3 • 1 min 30 s • 1 min 30 s

Etching		
SF_6/Ar recipe	• RIE process	• 1 : 1 • 20 sccm total flow • 20 s • 100 W RF • 100 mTorr
CHF_3/O_2 recipe	• ICP-RIE process	• 10 : 1 • 44 sccm total flow • 30 nm of h-BN/min • 60 W RF • 2000 W ICP* • 20 mTorr*
Contacting		
Sample preparation	• Similar procedure as for lithography	
Metalization	• E-beam evaporation PVD**	• $\sim$ 5 nm Cr • $50 - 100$ nm Au

* Indicates values not described in the process, but used for the tests.
** Indicates a process not performed during this master thesis.

Appendix C

Supplementary illustrations

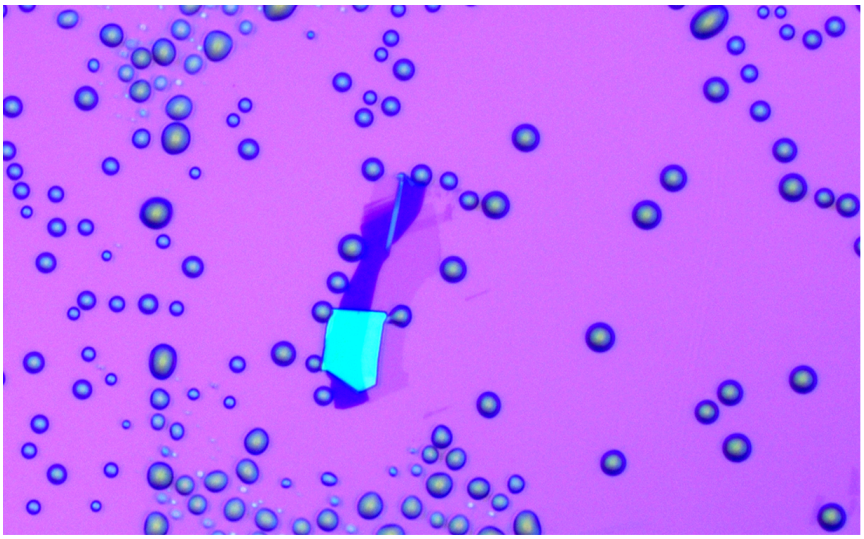


Figure C.1: Water droplets condensation below 0°C

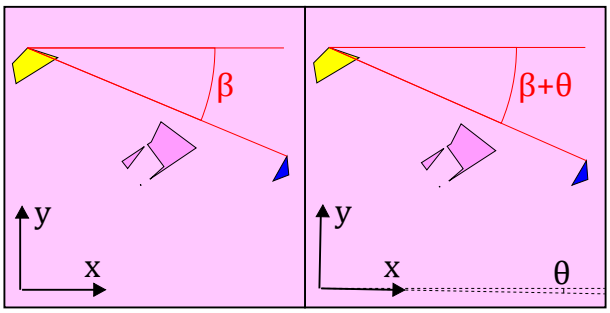


Figure C.2: Adjustment of the twist angle w.r.t. background elements.

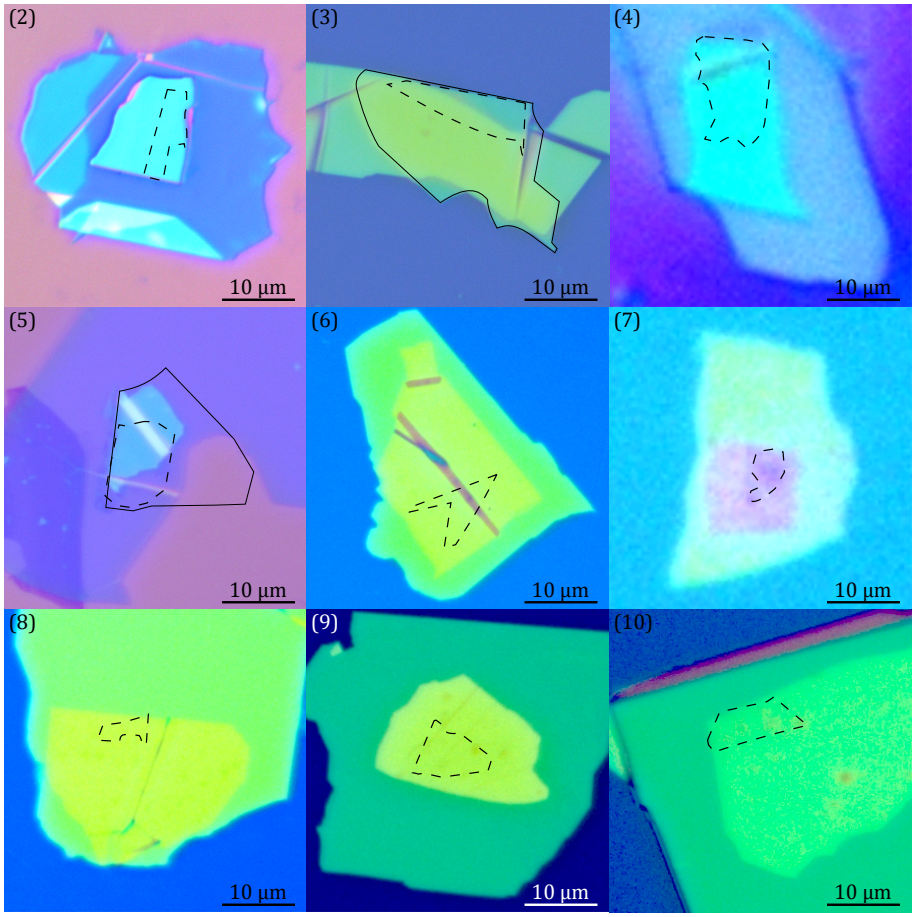


Figure C.3: All stacks discussed in section 4.3. The dashed line represent the suspected location of the tBLG. The solid lines (if present) represent the contours of the top h-BN flake before transfer.

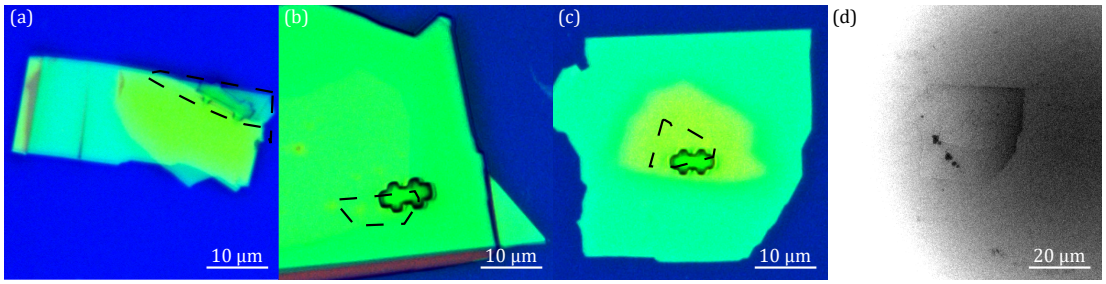


Figure C.4: (a-c) Results of lithography of Hall bars on different stacks. The dashed lines represent the presumed location of the tBLG. (d) Best contrast achieved during SEM imagery of the stack in (c).

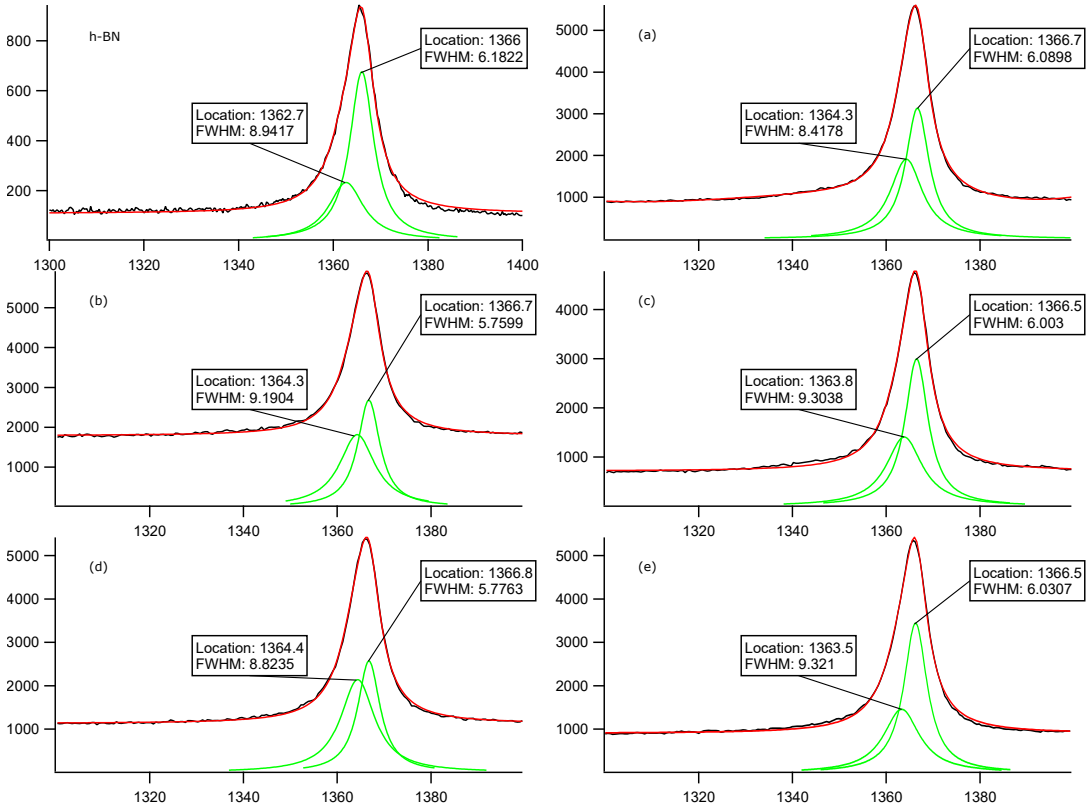


Figure C.5: Analysis of the h-BN peaks on an h-BN flake and at all contact points of figure 4.6. All peaks can be decomposed in two almost identical sub peaks with high accuracy. No D peak seems to have emerged from the stacking procedure. The horizontal axis represents Raman shift in cm^{-1} and the vertical axis represent Raman intensity in a.u.

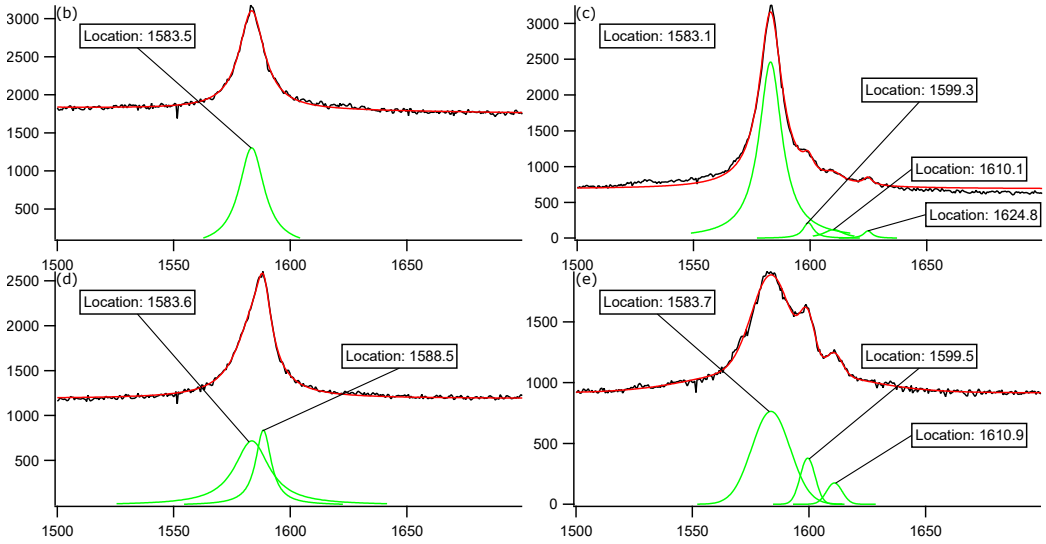


Figure C.6: Decomposition of the G peak of the spectra (b) to (e) from figure 4.6. The 1599 and 1611 cm^{-1} peaks appear 2 other times ((c) and (e)). Two other unidentified peaks at $\sim$ 1625 and $\sim$ 1589 cm^{-1} are visible respectively in (c) and (d). They are likely due to external factors as they only appear once. The horizontal axis represents Raman shift in cm^{-1} and the vertical axis represent Raman intensity in a.u.

UNIVERSITÉ CATHOLIQUE DE LOUVAIN
École polytechnique de Louvain
Rue Archimède, 1 bte L6.11.01, 1348 Louvain-la-Neuve, Belgique | **www.uclouvain.be/epl**